Master Thesis

MHz to TeV Expectations

from scotogenic WIMP Dark Matter

Laura Eisenberger

Würzburg, January 2024

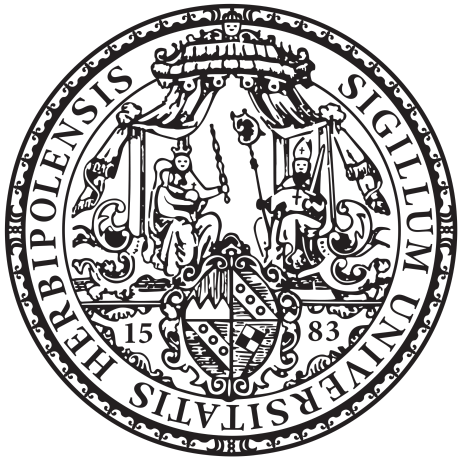

Julius-Maximilians-Universität Würzburg
Faculty of Physics and Astronomy

Supervisors:
Dr. Thomas Siegert, Prof. Dr. Karl Mannheim, Prof. Dr. Werner Porod

Abstract

There is strong evidence for the existence of dark matter (DM) from a large number of astrophysical and cosmological observations. While decades of intense direct and indirect searches could not reveal the nature of DM, a variety of theories trying to explain the DM phenomenon has been developed. Weakly Interacting Massive Particles (WIMPs) are one of the most promising DM candidates since they could naturally account for the observed cosmological abundance of DM which is known as the "WIMP miracle".

Scotogenic WIMPs arise in particle physics models where an additional symmetry ensures both the existence of a stable DM candidate and the generation of neutrinos masses through couplings to the dark sector (Ávila et al. 2020; Ma 2006). Alvarez et al. (2023) identified scotogenic DM candidates which can additionally explain the muon anomalous magnetic moment and, potentially, the baryon asymmetry of the Universe while fulfilling the current limits for charged lepton flavour violating processes. One such candidate is a fermionic WIMP with a mass around 1 TeV whose properties are used in this work to determine the primary and secondary emission from its annihilation products.

Particle DM could annihilate through weak couplings into detectable Standard Model particles. Most efforts on the indirect search for DM focus on the high-energy photons directly produced by DM annihilation. However, such prompt signals alone are too weak to be measurable in large astrophysical fore- and backgrounds. Following a multiwavelength approach, the secondary emission from charged annihilation products, including Inverse Compton (IC) scattering, bremsstrahlung and synchrotron radiation, should be also taken into account to increase the chances of detecting an unambiguous signal.

In this thesis, a parametrized model is developed to calculate the DM photon spectrum in 27 dwarf galaxies of the Milky Way, reaching from synchrotron emission in the MHz range to the IC peak at MeV energies and to the prompt signature in the GeV up to TeV regime. This unique "triple hump" structure will be easily distinguishable from any other source. From radiating cosmic particles within the Milky Way causing a large-scale diffuse emission and from catalogues containing Active Galactic Nuclei along the line-of-sight, the astrophysical fore- and background is estimated to obtain signal-to-background ratios in different energy bands for each galaxy. The ratios found for individual galaxies are up to the order of 10^{-3} between 1 keV and 100 GeV.

In the light of upcoming observatories like COSI-SMEX and CTA, the detection of faint DM signals is within reach if a coherent analysis of deep exposure observations of many galaxies across the MeV to GeV range is applied.

Zusammenfassung

Es gibt starke Hinweise auf die Existenz Dunkler Materie (DM) aus einer Vielzahl astrophysikalischer und kosmologischer Beobachtungen. Trotz jahrzehntelanger intensiver Suche konnte die Natur der DM bisher nicht enthüllt werden. Es gibt jedoch zahlreiche Theorien, die das Phänomen zu erklären versuchen. Schwach wechselwirkende massereiche Teilchen (WIMPs) gehören zu den vielversprechendsten Kandidaten, da sie auf natürliche Weise für die beobachtete kosmologische DM Dichte aufkämen, was als "WIMP-Wunder" bekannt ist. Skotogene WIMPs treten in Modellen der Teilchenphysik auf, bei denen eine zusätzliche Symmetrie sowohl die Existenz eines stabilen DM-Kandidaten als auch die Erzeugung von Neutrinomassen gewährleistet (Ávila et al. 2020; Ma 2006). Alvarez et al. (2023) identifizierten skotogene DM-Kandidaten, die zusätzlich das anomale magnetische Moment des Myons und möglicherweise die Baryonenasymmetrie des Universums erklären und gleichzeitig die aktuellen Limits für flavourverletzende Zerfälle geladener Leptonen erfüllen. Ein solcher Kandidat ist ein fermionisches WIMP mit einer Masse von etwa 1 TeV, dessen Eigenschaften in dieser Arbeit verwendet werden, um die primäre und sekundäre Emission seiner Annihilationsprodukte zu bestimmen.

DM aus Teilchen könnte durch schwache Kopplungen in nachweisbare Standardmodellteilchen annihilieren. Die meisten Bemühungen bei der indirekten Suche nach DM konzentrieren sich auf die hochenergetischen Photonen, die direkt durch die Annihilation erzeugt werden. Jedoch sind solche prompten Signale allein zu schwach, um diese in starker astrophysikalischer Vorder- und Hintergrundstrahlung messen zu können. Verfolgt man einen Multiwellenlängen-Ansatz, sollte auch die sekundäre Emission von geladenen Annihilationsprodukten, einschließlich inverser Compton (IC) Streuung, Bremsstrahlung und Synchrotronstrahlung, berücksichtigt werden, um ein eindeutiges Signal zu erhalten.

In dieser Arbeit wird ein parametrisiertes Modell zur Berechnung des DM-Photonenspektrums in 27 Zwerggalaxien der Milchstraße entwickelt, das von Synchrotronemission im MHz-Bereich, über den IC-Peak bei MeV-Energien, bis zur prompten Signatur im GeV- bis TeV-Bereich reicht. Diese einzigartige dreihöckrige Struktur kann leicht von jeder anderen Quelle unterschieden werden. Anhand der großskaligen diffusen Emission durch abstrahlende, kosmische Teilchen innerhalb der Milchstraße, sowie von Katalogen, die aktive Galaxienkerne entlang der Sichtlinie enthalten, wird der astrophysikalische Vorder- und Hintergrund abgeschätzt. Dadurch kann das Signal-zu-Hintergrund-Verhältnis in verschiedenen Energiebändern für jede Galaxie bestimmt werden. Die gefundenen Werte reichen bis zu 10^{-3} zwischen 1 keV und 100 GeV. Im Hinblick auf zukünftige Observatorien wie COSI-SMEX und CTA liegt die Detektion schwacher DM-Signale in Reichweite, wenn eine kohärente Analyse im Bereich von MeV bis GeV angewendet wird.

Contents

1 Introduction **1**

2 The Dark Matter Phenomenon **3**

2.1 Evidence for Dark Matter . . . 3

2.1.1 Gravitational Consequences . . . 3

2.1.2 Cosmological Arguments . . . 6

2.2 Dark Matter Candidates . . . 8

2.2.1 Nonbaryonic Dark Matter . . . 9

2.2.2 Baryonic Dark Matter and Other Possibilities . . . 9

2.3 Distribution of Dark Matter in the Universe . . . 10

2.3.1 Dark Halo Formation . . . 11

2.3.2 Halo Density Profiles . . . 11

2.3.3 Subhalo Clumping . . . 14

2.4 Detection Strategies . . . 16

2.4.1 Collider Detection . . . 17

2.4.2 Direct Detection . . . 19

2.4.3 Indirect Detection . . . 20

3 Scotogenic Particle Model **26**

3.1 Motivation . . . 26

3.2 Field Content and Model Parameters . . . 27

3.3 Exploration of the Parameter Space . . . 29

3.3.1 Neutrino Masses . . . 29

3.3.2 The Muon anomalous magnetic Moment and cLFV Decays . . . 30

3.3.3 Dark Matter Observables . . . 30

3.4 Dark Matter Candidates . . . 33

4 Indirect Multiwavelength Approach **34**

4.1 Primary/Prompt Emission . . . 34

4.2 Secondary Gamma-Ray Emission . . . 36

4.2.1 Inverse Compton scattering . . . 39

4.2.2 Synchrotron radiation . . . 41

4.2.3 Bremsstrahlung . . . 42

4.3 Neutrino Emission 42
4.4 Dark Matter Spectral Energy Distribution 44

5 Application to Dwarf Galaxies **49**
5.1 Sample of Dwarf Galaxies 49
5.2 Expectations in Dwarf Galaxies 49

6 Astrophysical Fore- and Background **55**
6.1 Diffuse Galactic Emission 55
6.2 Dark Matter Halo of the Milky Way 62
6.3 Combined Multiwavelength SEDs 64
6.4 Source Confusion 69
6.5 Signal-to-Background Ratio 71

7 Conclusion and Outlook **74**

Bibliography **84**

Acknowledgements **84**

Declaration **85**

1 Introduction

About 27 % of the Universe consists of dark matter (DM), whereas the visible matter, such as protons, neutrons and electrons, accounts for only 5 % of the total energy density of the Universe (Aghanim et al. 2020). The remaining 68 % are assigned to dark energy which is responsible for the accelerated expansion of the Universe (Ade et al. 2016). DM, as this phenomenon is currently understood, requires the properties of being neutral, stable or at least long-lived and cold, so that the cosmological abundance is met and the conditions for structure formation are fulfilled (see e.g. Jungman et al. 1996). DM only interacts gravitationally and possibly weakly with ordinary matter but does not emit or absorb any electromagnetic radiation, which makes its detection extremely difficult.

There has been great effort from many experiments and observatories over the last decades to find a putative signal from DM (see e.g. Cebrián 2023; Gaskins 2016). Even though no clear detection has been made so far, many models have been ruled out or restricted in their parameter space of mass vs. cross section (see e.g. Geringer-Sameth & Koushiappas 2011) or decay time, for example. The indirect search for DM aims for the detection of visible matter generated by the annihilation or decay of DM particles. The

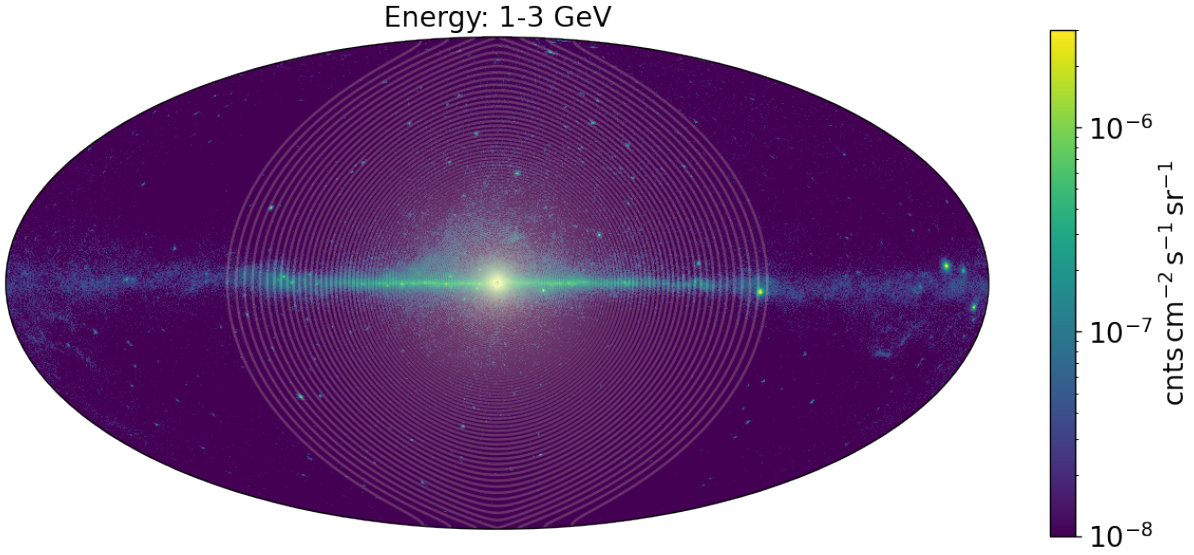

Figure 1.1: Sky map as observed by Fermi/LAT at 1–3 GeV. A possible DM signature from the halo of the MW is superimposed for illustrative reasons, whereby its brightness is not to scale. The strongest DM signal is expected from the GC where also the largest background emission prevails.

flux of produced particles depends on the nature, i.e. particle properties and type, of the DM candidate as well as on the DM density along the observer's line-of-sight. Weakly Interacting Massive Particles (WIMPs) are popular candidates for DM and arise, for example, in scotogenic particle models, such as the one investigated by Alvarez et al. (2023).

The strongest signal is expected from the Galactic Center (GC) which is the closest region with a high density of DM. Fig. 1.1 shows the sky map as observed by Fermi/LAT at 1–3 GeV, on which a possible DM signature from the halo of the Milky Way (MW) is superimposed for illustrative reasons. Especially in the central region, there is also strong emission of other origins, such as stars, dust, gas and cosmic ray (CR) induced processes (see e.g. Goldwurm 2011), masking any hints from DM. In addition, the profile of the DM distribution in the MW is highly uncertain towards the inner regions and only the local value around the Solar circle of about $0.3\,\mathrm{GeV\,cm^{-3}}$ is used as an anchor point for astronomical studies (Bovy & Tremaine 2012). For this reason, promising targets for the indirect search are the DM dominated satellite galaxies of the MW due to their proximity and low intrinsic background emission as they reside at high latitudes above the Galactic plane. It is still a challenge to disentangle the weak DM signals from the diffuse MW foreground. Therefore, the whole multiwavelength spectrum including primary and secondary effects of DM annihilation should be considered. Secondary photons are emitted by charged annihilation products via inverse Compton (IC) scattering, bremsstrahlung and synchrotron processes.

This thesis is structured as follows: Chapter 2 provides a general overview of the DM phenomenon, its distribution in galactic halos and different detection strategies. In Ch. 3, the scotogenic WIMP model and resulting DM candidates are described in detail. In Ch. 4, the parametrized model for the calculation of the DM multiwavelength photon spectrum including primary and secondary emission is introduced. A list of expected fluxes resulting from the spectral model in specific energy bands from 1 keV to 100 GeV according to the current instruments JEM-X/ISGRI, Swift/BAT, SPI, COMPTEL and Fermi/LAT is computed for 27 dwarf spheroidal galaxies of the MW in Ch. 5. The astrophysical fore- and background emission from CR induced diffuse Galactic radiation, DM annihilation in the MW halo itself and confusion with sources along the line-of-sight in these bands is estimated in Ch. 6. Finally, implications of the obtained signal-to-background ratios as well as possible extensions of the developed model are discussed in terms of detectability with future instruments in Ch. 7.

2 The Dark Matter Phenomenon

For a century, there has been strong evidence for the existence of DM from a large number of observations and theoretical considerations. From measurements of the Cosmic Microwave Background (CMB) anisotropies (Aghanim et al. 2020), it is known that DM accounts for 84% of the total cosmological matter density. Despite intensive research, the composition of DM still remains one of the greatest mysteries in physics. Trying to solve this puzzle requires close cooperation between astrophysics and particle physics as well as different search strategies. In this chapter, an overview of the evidence for DM, possible candidates and detection strategies is given.

2.1 Evidence for Dark Matter

The compelling evidence for the existence of DM is mainly based on gravitational and cosmological aspects. Some of the observational and theoretical arguments are discussed below.

2.1.1 Gravitational Consequences

Already in 1922, Kapteyn (1922) proposed to determine the amount of DM in the MW from the rotational velocities of stars. Oort (1932) investigated the velocity distribution in the direction perpendicular to the Galactic plane and determined a discrepancy of about 60% between the total density of matter near the Sun and the observed mass density of visible stars. He inferred that the invisible matter had to be more concentrated to the Galactic plane forming a dark disk. At about the same time, Zwicky (1933) postulated the presence of DM on larger scales. From the virial theorem, he derived that the mass density in the Coma Cluster had to be 400 times larger than the density resulting from luminous matter in order to account for the observed Doppler velocities of galaxies. Since then, many observations confirm the existence of a gravitationally acting invisible component on different scales.

The rotation curves of spiral galaxies are one of the most convincing evidence for dark halos in galaxies. Through optical spectroscopy, Rubin et al. (1978) confirmed that spiral galaxies show flat rotation curves. This means that the circular velocity of stars or gas remains constant with increasing distance r from the center of a galaxy (see Fig. 2.1 as an

example). According to Kepler's law, the rotational velocity is expected to decrease with $r^{-0.5}$. Beyond the galactic bulge which contains most of the visible matter, this decay is not observed. Instead, the rotational velocity remains constant which implies that the enclosed mass must grow linearly with radius, indicating the existence of a large, extended halo of invisible matter. A common interpretation is that this halo is composed of the unknown constituent named DM.

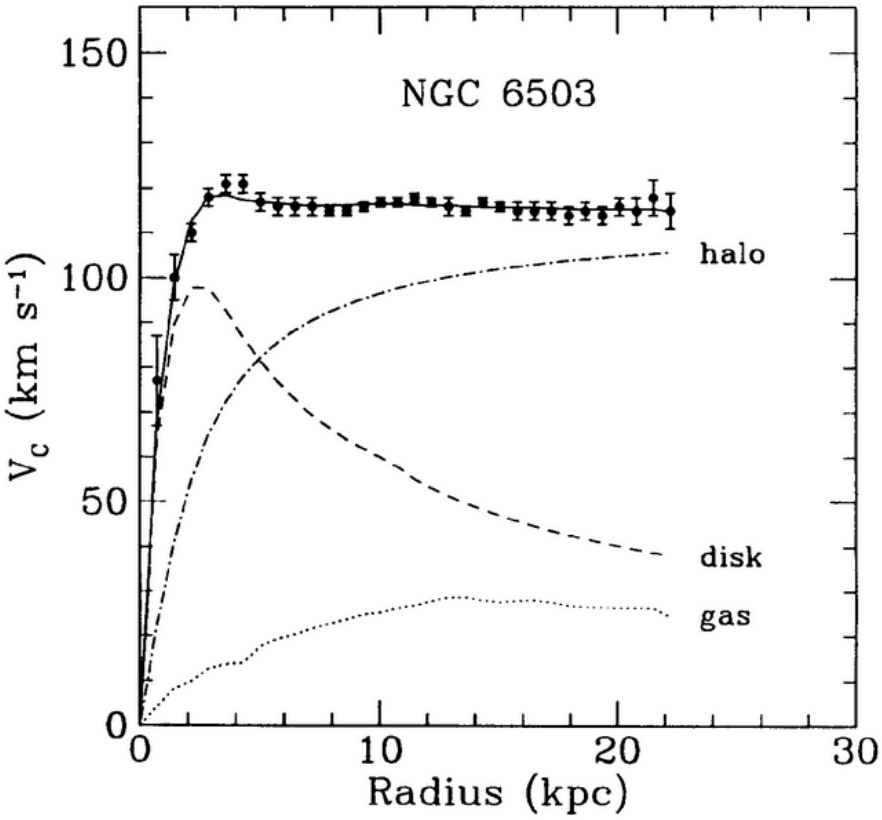

Figure 2.1: Rotation curve for the spiral galaxy NGC 6503 from Begeman et al. (1991). The rotational velocity was measured as a function of distance from the center of the galaxy. Since the disk and gas contribution cannot account for the observed rotation curve alone, a third component from an extended dark halo is needed.

Alternatively, the flatness of rotation curves is explained by deviations from Newtonian gravity. Milgrom (1994) suggested a Modified Newtonian Dynamics (MOND) as an alternative to the DM hypothesis at galactic scales. Thereby, the equation of motion is modified for a certain scale of acceleration a_0 corresponding to Newton's law in the limit $a_0 \to 0$. However, Clowe et al. (2006) refuted alternative gravity hypotheses by weak-lensing observations of the Bullet Cluster, a unique system where the DM component is expected to be spatially separated from the observed visible matter due to the collision of two galaxy clusters. Fig. 2.2 shows the X-ray emitting plasma, being the most massive baryonic component, and the corresponding gravitational lensing map of the merger. It can be seen that the clusters are dominated by DM since the gravitational potential is off-

set from the visible plasma distribution. Instead, it reflects two collisionless non-luminous components. While the Bullet Cluster is used as a standard example for the evidence of DM, there are doubts as to whether such systems are compatible with the standard cosmological model (Kraljic & Sarkar 2015).

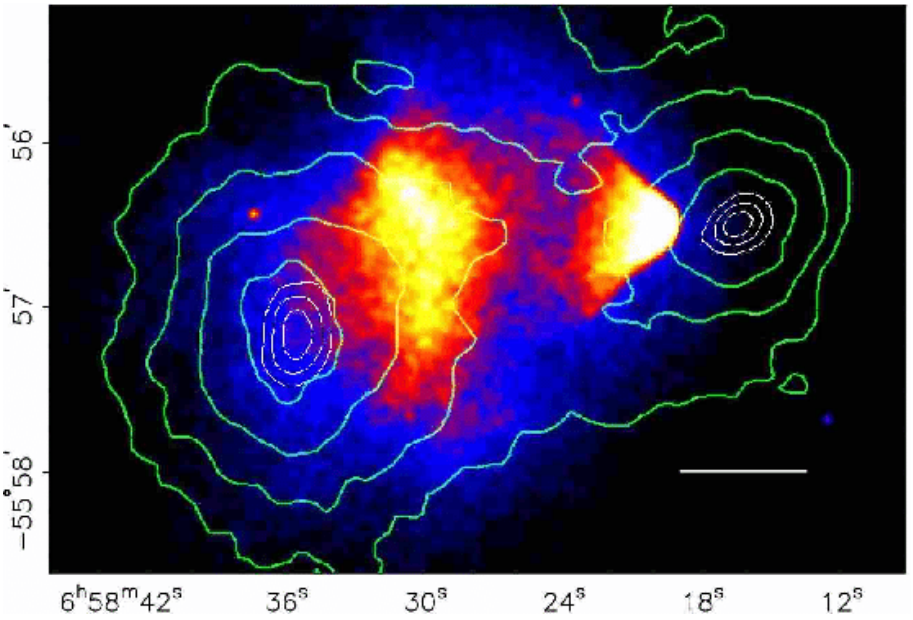

Figure 2.2: Chandra image of the galaxy cluster merger 1E 0657-558 from Clowe et al. (2006) showing the X-ray emitting plasma which decoupled from the galaxies. From the gravitational lensing map (green contours), it can be seen that the potential does not trace the dominant baryonic component but rather a collisionless DM distribution.

Compared to rotation curves, gravitational lensing can provide evidence of the existence of DM on much larger scales. According to the laws of General Relativity, the light from distant galaxies is distorted by the large amount of matter in galaxy clusters along the line of sight. Fig. 2.3 shows the strongly lensed images of galaxies behind the cluster Abell 370 as seen by the Hubble Space Telescope. In the weak lensing regime where the effect is less significant, the distortion of light cannot be detected in a single source but from statistical measurements of several background galaxies. From such observations the distribution of matter, both visible and dark, can be deduced (see, e.g. Jee et al. 2007).

Another evidence for DM in galaxy clusters comes from X-ray observations showing the structure of hot gas (see, e.g. Henry & Briel 1993). The presence of substructures indicates a hierarchical formation process through mergers of smaller to larger units which is given in a cosmological model including cold DM (see Sec. 2.1.2). The role of DM with respect to structure formation in the Universe is discussed in detail in Sec. 2.3.

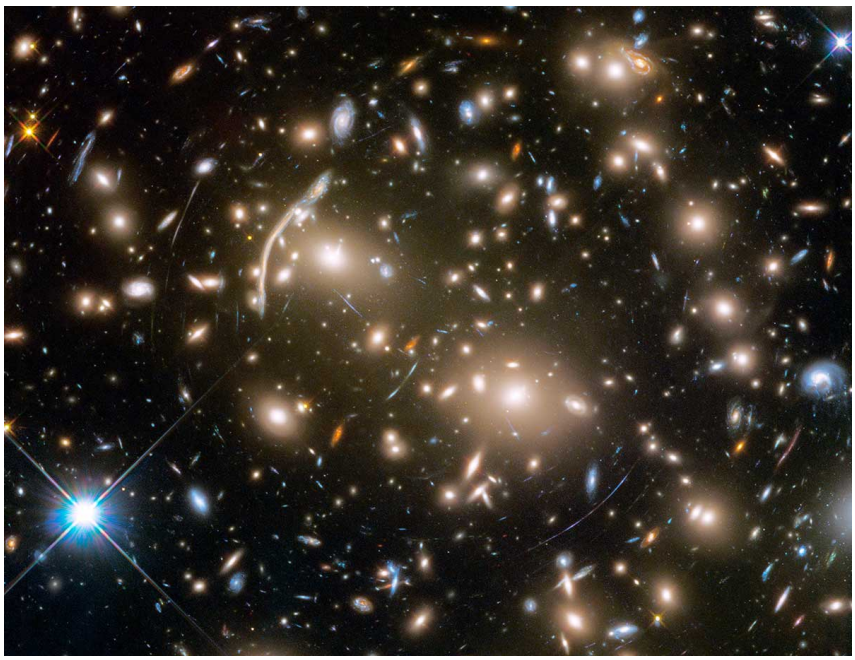

Figure 2.3: Strong lensing of distant galaxies by the gravitational field of the cluster Abell 370 as seen by the Hubble Space Telescope. Gravitational lensing probes the distribution of matter both visible and dark in galaxy clusters. Image from NASA, ESA, and J. Lotz and the HFF Team (STScI).

2.1.2 Cosmological Arguments

Since the ΛCDM model (CDM: cold dark matter) with Λ being the cosmological constant is able to explain the observed CMB anisotropies (see Fig. 2.4a), it is currently the best cosmological model describing the evolution of the Universe. Fig. 2.4b shows the corresponding power spectrum of the temperature fluctuations as measured by the Planck satellite as a function of angular scale (Aghanim, N. et al. 2020). The variations are caused by acoustic oscillations of the photon-baryon plasma of the hot, early Universe and are therefore an imprint of density fluctuations leading to structure formation (see Hu 2001, for detailed explanations). The position and amplitude of the first peak of the spectrum is consistent with a spatially flat universe. From the peaks at smaller scales, the baryon density Ω_b and DM density Ω_c can be derived. The cosmological density is defined as $\Omega = \rho/\rho_\mathrm{c}$, where the critical density is:

$$\rho_\mathrm{c} = \frac{3H^2}{8\pi G} = 1.88h^2 \times 10^{-29}\,\mathrm{g\,cm^{-3}}\,. \tag{2.1}$$

The uncertainty of the Hubble constant is reflected by $h = H_0/(100\mathrm{km\,s^{-1}\,Mpc^{-1}})$. The current values of H_0 range from about $67.4\,\mathrm{km\,s^{-1}\,Mpc^{-1}}$, as inferred from the Planck CMB measurements and the ΛCDM model (Aghanim et al. 2020), to $74.2\,\mathrm{km\,s^{-1}\,Mpc^{-1}}$, as determined from Hubble Space Telescope observations of a sample of Cepheids (Riess et al. 2019). The latter are variable stars with a regular period which are used as "standard

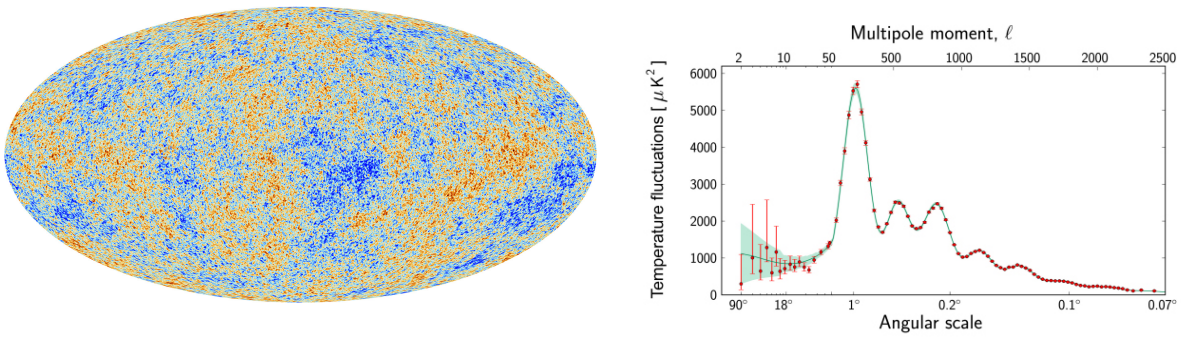

(a) Full sky map of temperature anisotropies of the CMB.

(b) Power spectrum of the temperature fluctuations and ΛCDM fit.

Figure 2.4: Temperature anisotropies of the CMB as observed by Planck. From the corresponding power spectrum, the baryonic and DM densities can be determined. Images from ESA and the Planck Collaboration[1].

candles" for the calibration of distance measurements.

Aghanim et al. (2020) determined the abundances of ordinary and dark matter to be $\Omega_b h^2 = 0.0224 \pm 0.0001$ and $\Omega_c h^2 = 0.120 \pm 0.001$, respectively. For a spatially flat cosmology (Friedmann 1922), the total energy density of the Universe is $\Omega = 1$. In the present day, the radiation energy density is almost zero because the Universe has cooled while expanding. Since the total matter energy density is much smaller than 1, the missing density of $\Omega_\Lambda h^2 \approx 0.31$ is assigned to dark energy.

An argument for the paradigm that DM is nonbaryonic comes from limits of primordial nucleosynthesis restricting the density of ordinary matter. Assuming the baryonic content to be only 4% of the total Universe, the Big Bang predicts abundances of helium, deuterium and lithium which are consistent with measurements (Smith et al. 1993; Walker et al. 1991). This means that the large part of the total matter density originates from DM. Considering the cosmological baryonic abundance, there is also a significant amount of dark baryons referring to luminous matter which has not been detected yet (Cen & Ostriker 1999).

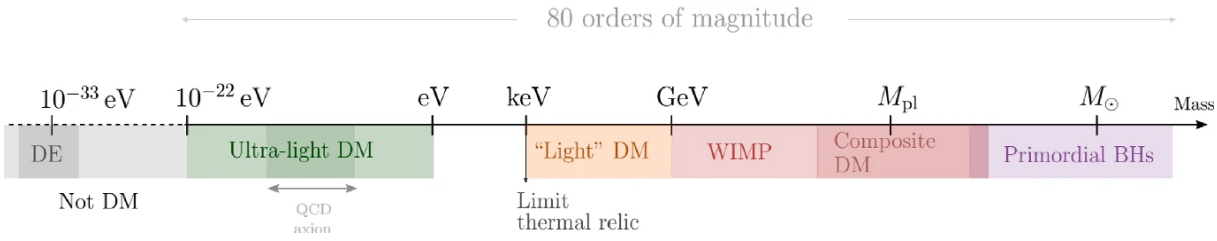

Figure 2.5: Mass range of classes of possible DM candidates. Figure from Ferreira (2021).

[1] https://wwwmpa.mpa-garching.mpg.de/mpa/institute/news_archives/news1303_aaa/news1303_aaa-en-print.html

2.2 Dark Matter Candidates

The number of possible DM candidates is large since it is only known about the gravitational properties of DM. On a microscopic scale, however, it is still completely unknown what DM consists of. Consequently, the mass range of DM classes spans 80 orders of magnitude reaching from ultra-light DM to Primordial Black Holes (PBHs, see Fig. 2.5). There is a variety of different theories and solutions trying to explain DM (see Fig. 2.6). In the following, some examples, among them baryonic and nonbaryonic, particle and nonparticle candidates, are given (see e.g. Jungman et al. 1996).

Figure 2.6: Overview of different DM theories. On the one hand, there are particle DM candidates spanning a wide range of masses, such as light bosons, neutrinos and weakly interacting DM arising in distinct frameworks. On the other hand, alternative solutions are modified gravitation theories and macroscopic DM. None of the candidates has been found except for MACHOs, which cannot account for the total amount of DM, and neutrinos, which are classified as hot DM and thus are inconsistent with the formation of structure in the early Universe. Figure from Bertone & Tait (2018).

2.2.1 Nonbaryonic Dark Matter

From Big-Bang nucleosynthesis, it is evident that even though there are hints of baryonic DM, the bulk of DM seems to be of nonbaryonic origin. Although ordinary neutrinos are neutral and only interact weakly with matter, they have been ruled out as DM candidates already in White et al. (1983) and Tremaine & Gunn (1979), for example. Neutrinos are classified as hot DM, a class of DM moving at relativistic speeds at the beginning of structure formation. However, hot DM cannot clump on small scales and thus fails to produce the observed fluctuations in the CMB and the present structure of galaxies in clusters. For this reason, DM has to be either cold or at least warm, that means moving at nonrelativistic or moderate speeds in the early Universe. In contrast to "active" neutrinos, sterile neutrinos would be right-handed and devoid of the weak interaction but could mix with the known neutrino flavors. They have been proposed by Abazajian et al. (2001) as viable cold, warm and hot DM candidate.

Theoretical particle physics offers a variety of possible particle DM beyond the Standard Model (SM). The most popular cold DM candidates are WIMPs as well as axions. The axion is a light, pseudo-scalar particle which stems from a proposed solution to the strong-CP problem. Its viable mass range has been found by Turner (1990) to be between 10^{-6} and $10^{-3}\,\mathrm{eV}$. Axions can possibly be detected when they convert to photons in a strong magnetic field. Latest searches for axion-like particles (ALPs) in Betelgeuse by Xiao et al. (2021) put constraints on the ALP-photon coupling for ALP masses between 10^{-15} and $10^{-9}\,\mathrm{eV}$.

WIMPs could be thermal relics of the early Universe with masses in the GeV to TeV range which means that their cosmological abundance naturally is of the same order than that for DM (see Sec. 3.3.3 for the calculation of the relic abundance). This so-called "WIMP miracle" makes them promising DM candidates which could possibly be detected via their annihilation and/or decay products. On the particle physics side, WIMPs are mostly proposed by supersymmetric extensions of the SM implementing an additional symmetry between bosons and fermions. The most famous supersymmetric WIMP candidate is the lightest neutralino in the Minimal Supersymmetric Standard Model (MSSM) in which every SM particle has a superpartner (Csáki 1996). Stable DM particles also arise in so-called scotogenic models which implement an additional $\mathbb{Z}_2$ symmetry under which all SM particles are even while new particles are odd. The scotogenic model and the properties of the resulting WIMP DM are used in this work and will be further explained in Sec. 3.

2.2.2 Baryonic Dark Matter and Other Possibilities

A fraction of the observed amount of DM might be of baryonic origin. This includes for example Massive Compact Halo Objects (MACHOs), a category summarising dark objects like faint stars, brown dwarfs, white dwarfs, neutron stars and black holes which

are detectable by gravitational microlensing (see e.g. Alcock et al. 2000).
PBHs could have formed in the early Universe. Depending on the time of formation, their masses could range from the Planck mass to thousands of solar masses. PBHs are actually considered as nonbaryonic since they formed before the Big Bang nucleosynthesis and could therefore contribute to the cosmological DM density (Carr & Kühnel 2022). The fraction of the PBH abundance with respect to the total DM energy density is constrained, for example, by microlensing observations or evaporation signatures (see Fig. 2.7). The latter refers to the mass loss of BHs due to Hawking radiation (see e.g. Villanueva-Domingo et al. 2021)
Apart from that, there are several non-Newtonian gravity theories like MOND (Milgrom 1994). However, modified gravity models face problems when it comes to the explanation of DM in galaxy clusters.

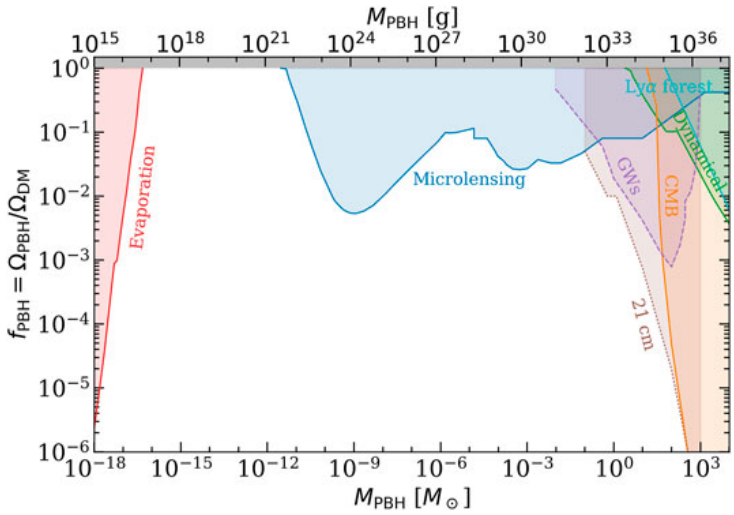

Figure 2.7: Exclusion limits on the PBH fraction with respect to DM as a function of the PBH mass. Considered are, for example, the impact of PBH evaporation on the extragalactic gamma-ray and CMB background, constraints from microlensing observations, PBH accretion signatures on the CMB or merger events from gravitational waves. Figure from Villanueva-Domingo et al. (2021).

2.3 Distribution of Dark Matter in the Universe

DM halos of galaxies are gravitationally bound regions with radii defined in a way that the halo encloses a certain DM overdensity (Wechsler & Tinker 2018), for example, 200 times the critical density of the Universe (see Eq. 2.1). They are believed to be the potential wells into which ordinary matter has collapsed to form galaxies. Rotation curves of galaxies (see Fig. 2.1) show that the dark halo has to extend far beyond the visible matter of a galaxy, exceeding radii of both bulges and disks. In order to determine the annihilation rate within a certain region, it is important to constrain the DM density distribution of

galaxies which is expected to exhibit multiple peaks from subhalos bound to the host halo with a smooth profile.

2.3.1 Dark Halo Formation

DM plays a crucial role in the structure formation of the Universe (Ferreras 2019). From measurements of the CMB anisotropies (Aghanim et al. 2020), it is known that small density fluctuations led to the formation of structures which grew through gravitational attraction over time. According to the ΛCDM cosmological model, cold DM is needed to explain the primordial density perturbations since baryonic matter was too hot to form gravitationally bound clumps in the early Universe. The evolution from a initially linearly growing density fluctuation to a stable DM halo can be described by spherical collapse. A structure is virialized when it reaches a state of equilibrium between its average kinetic and potential energy. In other words, a sphere collapses to a gravitationally bound DM halo when gravity overcomes the Hubble expansion at some critical density. The halo mass function, that is the number density of DM halos per mass interval, can be derived from a statistical description of halo formation (Press & Schechter 1974). Subsequently, galaxies could form through the collapse of gas into the centers of DM halos which is a complex process including cooling, star formation and baryonic feedback effects. The latter refers to processes involving baryonic matter, such as supernova explosions or outflows of Active Galactic Nuclei (AGN), which affect the star formation activity and therefore the evolution of galaxies (Ferreras 2019). The nonlinear growth phase and hierarchical structure formation from small halos merging and accreting to more massive ones complicates an analytical description. Properties and effects of subhalos surviving in larger host halos are discussed in Sec. 2.3.3.

On larger scales, DM provides the gravitational "skeleton" on which galaxies form resulting in a cosmic web consisting of filaments, voids and clusters. The large scale structure of the Universe has been mapped by several redshift surveys, such as the 2 degree Field Galaxy Redshift survey (2dFGRS, Norberg et al. 2001) or the Sloan Digital Sky Survey (SDSS, York et al. 2000). Fig. 2.8 shows the similarities between such observed galaxy distributions and the large scale structure maps from the Millennium simulation, a large N-body simulation with more than 10^{10} particles (Springel et al. 2005).

2.3.2 Halo Density Profiles

The choice of shape for the DM distribution highly affects the magnitude of the expected annihilation signal. DM density profiles can be roughly divided into two groups: cusped models are characterized by a steep density increase towards the halo center while cored profiles exhibit a constant density up to a certain radius (see Fig. 2.9).

Examples of cusped density distributions favored by N-body simulations are the widely

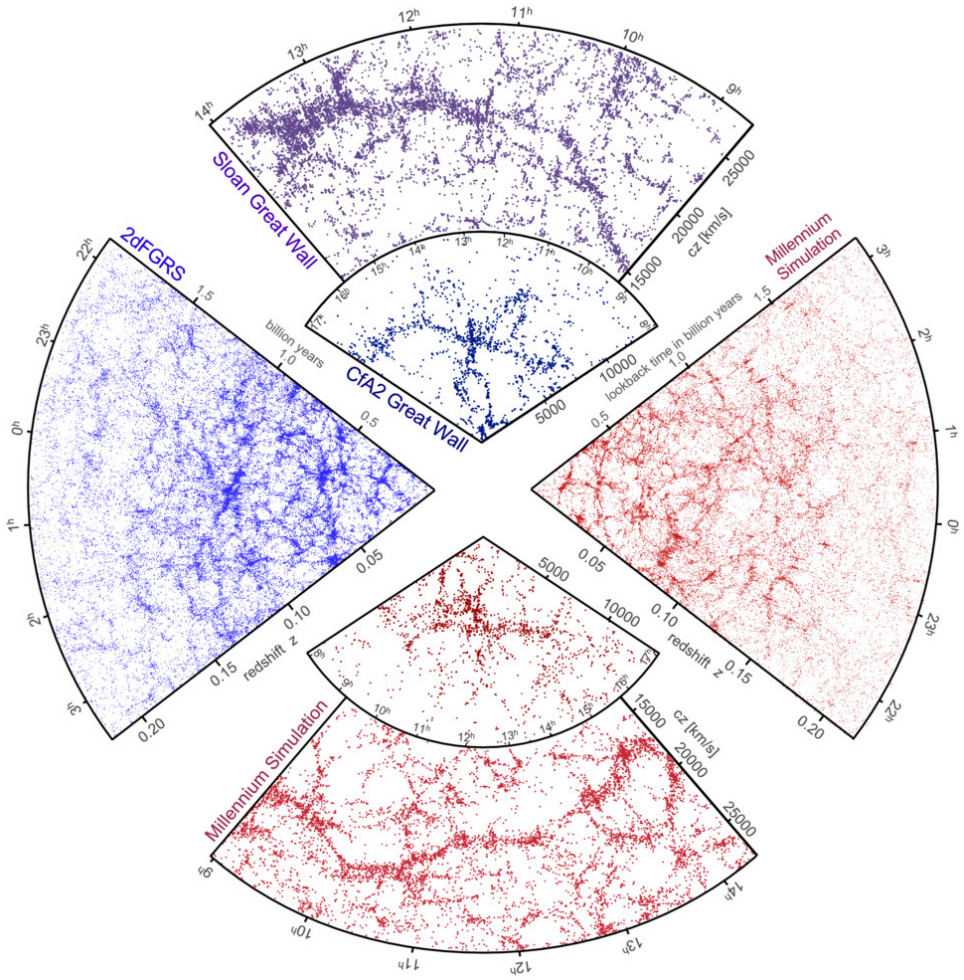

Figure 2.8: Large scale structure maps from the Millennium simulation (red) compared to observed distributions (blue) from the 2dFGRS, Sloan and CfA2 surveys showing structures of similar size and distribution. The radial coordinate can be expressed in either redshift or lookback time. The angle corresponds to the direction into which all galaxies (the data points shown) are projected. Figure from Springel (2006).

used Navarro-Frenk-White (NFW) profile (Navarro et al. 1997), where $\gamma = 1$, and the highly cusped Moore profile (Moore et al. 1998), where $\gamma = 1.5$:

$$\rho_{\rm cusp}(r) = \frac{\rho_{\rm s}}{(r/r_{\rm s})^{\gamma}(1 + r/r_{s})^{3-\gamma}}\,, \tag{2.2}$$

where $\rho_{\rm s}$ is the density at a scale radius $r_{\rm s}$ characteristic for each halo. Such cusped density models would strongly enhance the effectiveness for searches of annihilation signals in the inner halo regions. However, there is observational evidence from microlensing (Binney & Evans 2001) and from the rotational speed of the Galactic bar (Debattista & Sellwood 1998) that the halo of bright galaxies such as the MW is not cusped but rather cored resulting in a less bright DM signal from the GC. Examples of cored DM density distributions are the modified isothermal sphere (Begeman et al. 1991), with $\alpha = 0$, and

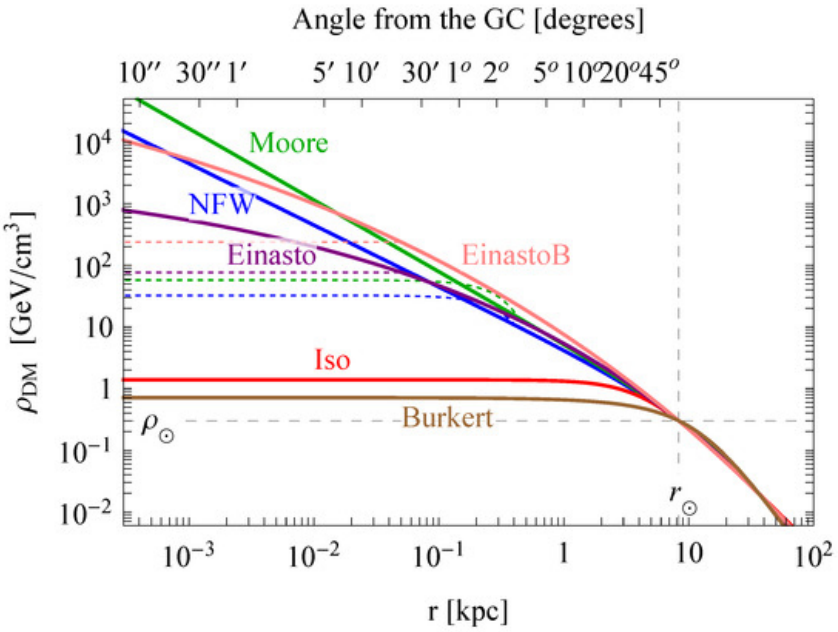

Figure 2.9: Different DM density profiles of the Galactic halo. While the NFW and Moore model are characterized as cusped profiles and would therefore enhance the annihilation signal in the GC, the isothermal and Burkert distributions are cored profiles describing a less dense inner region. All profiles are scaled in a way that they reproduce the estimated DM density at the position of the Sun of about $0.3\,\mathrm{GeV\,cm^{-3}}$. Figure from Pérez de los Heros (2020).

the Burkert profile (Burkert 1995), with $\alpha = 1$:

$$\rho_{\mathrm{core}}(r) = \frac{\rho_{\mathrm{s}}}{(1 + r/r_{\mathrm{s}})^{\alpha}(1 + (r/r_s)^2)}\,. \tag{2.3}$$

The origin of the flattening of halo profiles is not yet understood but might be due to baryonic feedback during galaxy formation as suggested by Binney et al. (2001).
The profile shape of an individual galaxy halo is determined by the two free parameters ρ_{s} and r_{s} which can be obtained from observational data such as the line-of-sight velocity dispersion of stars in a galaxy at different radii giving insights into the gravitational potential and thus into the mass distribution (Evans et al. 2004). However, for many galaxies there are limitations on observational data so that the parameters have to be estimated based on similar systems, which increases the uncertainties on derived quantities, such as DM annihilation fluxes.
Even though the shape of DM halos is usually approximated as spherical, there are indications that axisymmetric or even triaxial shapes are more realistic (see e.g. Posti, Lorenzo & Helmi, Amina 2019; Schneider et al. 2012).
Summarizing the conclusions in terms of observational strategies, the DM signal is expected to be stronger towards the center of a galaxy. The problem is that the DM density is much more uncertain in the inner regions compared to higher latitudes. Another advantage of off-center observations is that astrophysical foregrounds from which the DM

signal has to be distinguished are much lower. Observing targets with larger distances again weakens the flux but makes the signal also less sensitive to the choice of DM profile for larger integration angles (see Ch. 5).

2.3.3 Subhalo Clumping

DM halos of galaxies can be expected to show substructure and to only on average appear smooth. They may contain subhalos of different sizes due to hierarchical structure formation. Smaller halos would have a higher density as they collapsed earlier when the Universe was denser. As a consequence, the annihilation signals could be significantly boosted by overdense regions along the line-of-sight. Ando et al. (2019) provides a useful review of the properties of halo substructures and their boosting effects. The size of the smallest subhalo depends on the underlying DM model and is of the order of the Earth mass in the case of supersymmetric neutralino DM. Other DM particle models suggest different cutoffs, so that a measurement of the linear matter function of structure formation to the smallest scales may in fact inform about the DM particle responsible.
The boost factor is defined as the ratio of the luminosity stemming from annihilation in the subhalos to that originating from the smooth host halo component without substructure. The derivation of the annihilation boost factor is nontrivial and subject to large uncertainties. Assuming that the total DM density $\rho(\vec{r})$ depending on the location $\vec{r}$ consists of a smooth component $\rho_{\rm sm}(\vec{r})$ and a subhalo component $\rho_{\rm sh}(\vec{r})$, the annihilation signal is proportional to:

$$\langle\rho^2(\vec{r})\rangle = \langle\rho^2_{\rm sm}(\vec{r})\rangle + \langle\rho^2_{\rm sh}(\vec{r})\rangle + 2\langle\rho_{\rm sm}(\vec{r})\rho_{\rm sh}(\vec{r})\rangle\,, \tag{2.4}$$

which results in a total luminosity related to the host luminosity in the absence of subhalos $L_{\rm host,0}$:

$$L_{\rm total} = (1 - f^2_{\rm sh} + B_{\rm sh})L_{\rm host,0}\,, \tag{2.5}$$

where $f_{\rm sh}$ is the mass fraction in subhalos obtained from integrating the subhalo mass function $dN_{\rm sh}/dm$ and $B_{\rm sh}$ is the subhalo boost factor:

$$B_{\rm sh} = \frac{1}{L_{\rm host,0}}\int dm \frac{dN_{\rm sh}}{dm} L_{\rm sh}(m)\,. \tag{2.6}$$

In order to include "sub-subhalos", the subhalo luminosity has to be multiplied by $1 - f^2_{\rm ssh} + B_{\rm ssh}$. Considering "sub^n-subhalos", the boost factor could be calculated iteratively.
What makes this approach complicated, is that it cannot be naively the same density profile for subhalos and their hosts assumed. Effects like tidal stripping, which means that the host halo has stripped away mass from its subhalos, and encounters with other

subhalos can modify the density distribution (see e.g. Bartels & Ando 2015). The smallest halos are expected to have steeper central density profiles compared to more massive halos which flattened when they merged with other halos. The concentration-mass relation, that is the average concentration parameter as a function of halo mass, is expected to be higher for subhalos due to formation in dense environments and tidal stripping and might also depend on the distance from the host halo center.

Estimates on the boost factor are provided by cosmological N-body simulations and by analytical models. The first approach favors cuspy density profiles and indicates that the subhalo mass function and concentration-mass relation follow power laws. Numerical simulations, including only gravitational interactions, lead to the problem of predicting too many subhalos compared to the number of observed dwarf galaxies, which is commonly known as the "missing satellite problem". While this issue could be resolved by taking baryonic effects through hydrodynamic interactions into account, the major problem of N-body simulations is the limited resolution of the order of 10^4–$10^5\,M_\odot$ for halos with $10^{12}\,M_\odot$. For comparison, in the case of neutralino DM, a resolution of $10^{-6}\,M_\odot$ would be required to see the smallest subhalos. Therefore, the determination of the boost factor requires an extrapolation far beyond the numerical resolution leading to large uncertainties. Cosmological simulations generally yield large boost factors on the order of 100 for MW-size halos.

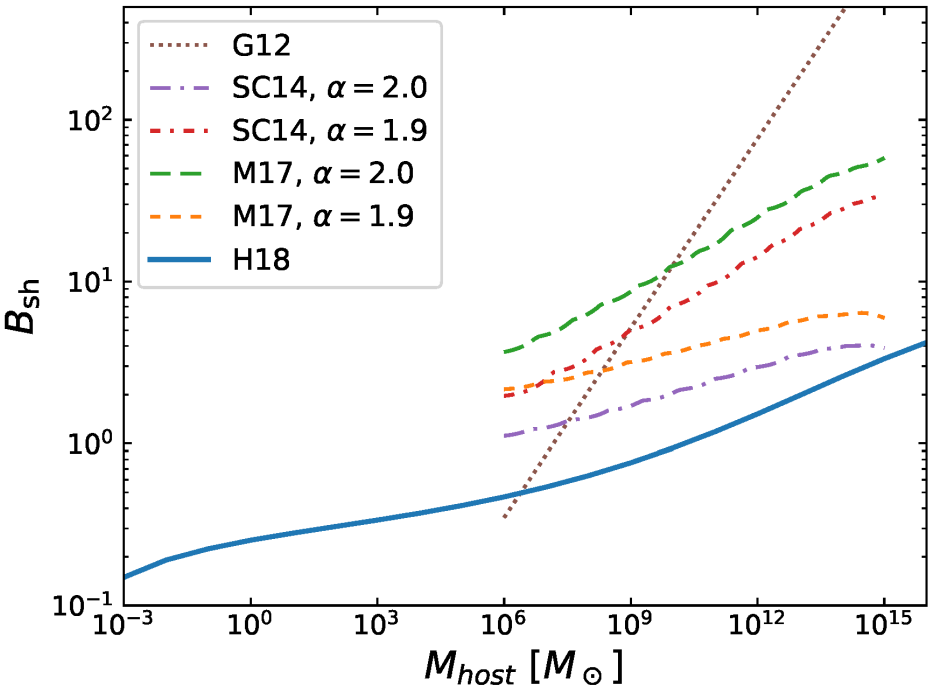

Figure 2.10: Subhalo boost factor as a function of the host halo mass obtained from different N-body simulations and one analytical model (blue). α is the assumed power law index of the subhalo mass function. Figure from Ando et al. (2019).

Another approach is to determine the boost factor via analytical models such as the extended Press-Schechter formalism describing the fraction of collapsing halos including collapsed regions within larger halos in a statistical way (Bond et al. 1991). Hiroshima et al. (2018) estimate the effect of sub^n-subhalos iteratively by assuming self similar subhalo properties characterized by mass, redshift, accretion history and mass loss. On the one hand, analytical models are calibrated with N-body simulations at resolved regimes and reproduce similar results. On the other hand, analytical approaches yield rather modest boost factors compared to simulations, of the order of 1 for MW-size halos.
Fig. 2.10 shows the subhalo boost factor as a function of the host halo mass for an analytical model compared to several simulated results. In dwarf galaxies, substructure boosts are expected to be less relevant because smaller halos contain less subhalos. They typically have masses between 10^3 and $10^7 M_\odot$ (McConnachie 2012) which results in boost factors smaller than 1 in the analytical case. According to N-body simulations annihilation in dwarf galaxies is possibly boosted by a factor between 1 and 5. However, subhalos might have a significant impact on the DM foreground originating from annihilation in the MW.

2.4 Detection Strategies

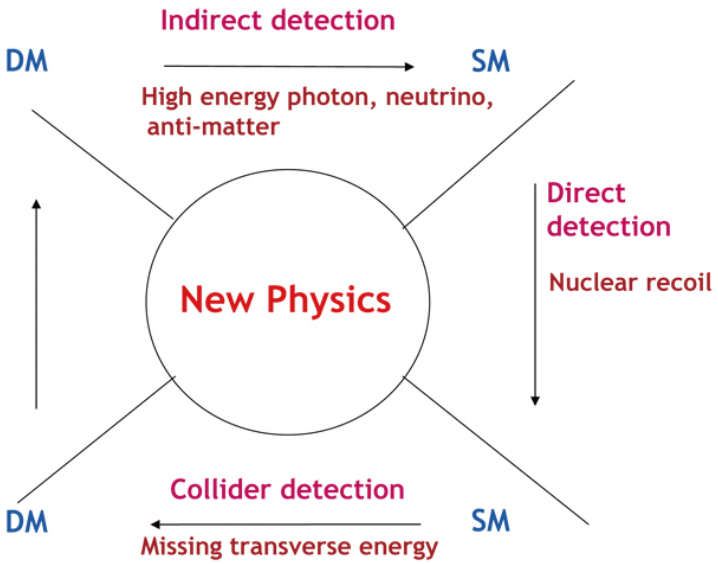

Figure 2.11: Strategies for the detection of particle DM. Figure from the 2023 Bulletin of the Chinese Academy of Sciences.

The interaction between particle DM and ordinary matter has to be weak but offers three types of detection strategies corresponding to the different channels in Fig. 2.11. Direct detection means measuring the nuclear recoil from a DM particle scattering off a SM particle. In a particle collider, DM is produced by the collision of SM particles which could be detected, for example, from missing transverse energy of the known products.

The opposite process is the production of SM particles from DM annihilation and offers the possibility of an indirect DM detection for example via photons.
So far, either channel is limited by the sensitivity of the corresponding instruments, so that at least parts of the parameter space have been ruled out for specific models. It is important to note that the model dependence of exclusion limits is an intrinsic difficulty. Due to the variety and complexity of distinct DM models, there is a large parameter space to be probed. Every detection channel has its advantages and disadvantages in terms of experimental conditions which makes the different search strategies highly complementary.

2.4.1 Collider Detection

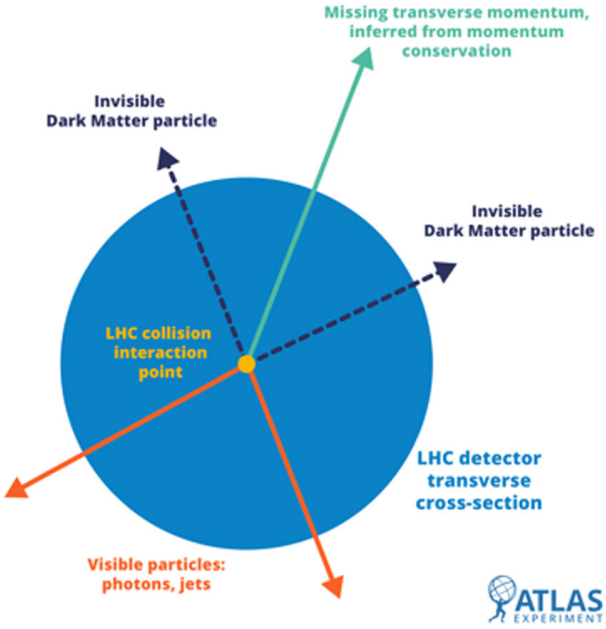

Figure 2.12: Illustration of the missing transverse energy (MET). The LHC beams are orientated perpendicular to the plane. Figure from ATLAS[2].

One approach to detect WIMP DM is finding characteristic signals at particle accelerators. An overview of DM searches at the Large Hadron Collider (LHC) is given, for example, by Giagu (2019) and is briefly summarized below. On the one hand, colliders are more sensitive to low mass DM (see Fig. 2.13) and have relatively small experimental uncertainties compared to direct and indirect searches which rely on the knowledge of the DM distribution with its major systematic uncertainties. On the other hand, there are constraints on the detection of very massive DM and/or its mediator due to the limited amount of energy per proton collision. A mediator particle, such as the gauge bosons of the SM, carries a certain interaction between other particles. The theoretical framework commonly used in this context are effective field theories (EFTs) which describe the interaction between SM and DM particles at a certain energy scale in a general, model

[2] https://atlassoftwaredocs.web.cern.ch/AnalysisSWTutorial/obj_met_intro/

independent way (see e.g. Bell et al. 2015).

Besides the search for light DM, the methods of collider detection can be categorized in the search for final states with and without DM. In the first case, the DM mass is small compared to the mediator mass which means that the produced WIMP pair is boosted in one direction. This would lead to a so-called mono-X signature with X being a detected SM particle from which the missing transverse energy (MET) could be determined (see Fig. 2.12). For instance, MET assigned to DM could be found in mono-jets or mono-photon/Z/W signatures, which are QCD jets or vector bosons radiated off a quark in initial state, respectively. Apart from that, MET could be detected in heavy quark final states, such as $b\bar{b}$, $t\bar{t}$, b and t, or in Higgs decays.

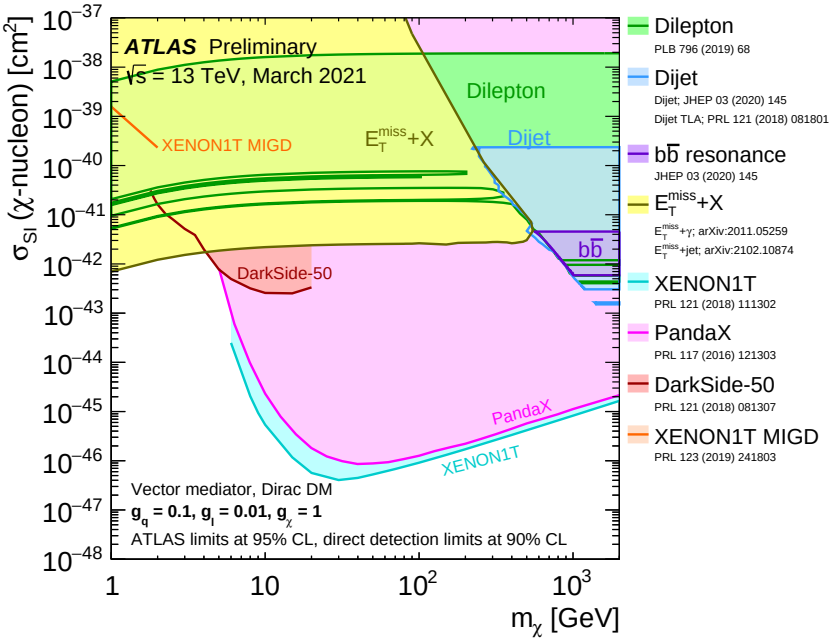

Figure 2.13: Exclusion limits on the spin-independent WIMP-nucleon scattering cross section for mono-X, dilepton, dijet and $b\bar{b}$ resonance searches by the ATLAS experiment compared to direct-detection experiments. The results are valid in the context of a simplified model with leptophilic vector couplings. Figure from ATLAS[3].

If a DM particle is heavier than its mediator, final states without DM can still give important constraints since the mediator particle may also decay into SM instead of DM pairs. In this case, dijet (two QCD jets) or dilepton resonances could be measured in the respective mass spectrum indicating the presence of DM.

In order to make accelerator constraints comparable to other detection strategies, the obtained limits can be converted to a cross section vs. WIMP mass parameter space. However, the cross sections depend on the mediator mass and the couplings assumption which makes the comparison only valid for a specific model. In Fig. 2.13, the limits

[3] https://atlas.web.cern.ch/Atlas/GROUPS/PHYSICS/PUBNOTES/ATL-PHYS-PUB-2021-006/

obtained from different channels are shown in the context of a simplified model with leptophilic vector couplings.

2.4.2 Direct Detection

Since the Earth is located in the DM halo of the Galaxy, it is constantly hit by WIMPs if DM consists of such. Most DM particles pass through the Earth without interaction. Nevertheless, there is a small chance that some nuclei experience a recoil from a WIMP collision. The attempt of measuring a WIMP-nucleus interaction is referred to as direct detection experiments. Jungman et al. (1996) provides a useful overview of direct and other DM search strategies.

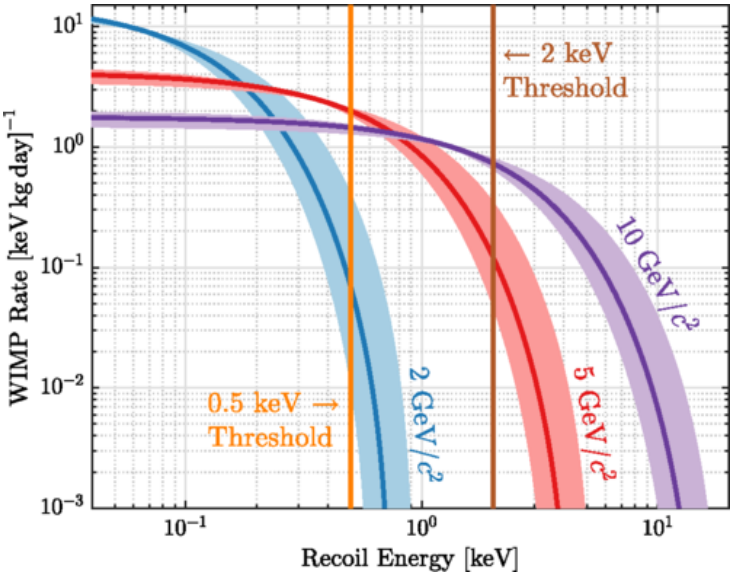

Figure 2.14: Differential rates for WIMP recoils on a germanium target as functions of recoil energy. Different WIMP masses are considered while the WIMP-nucleon spin-independent cross section is set to $10^{-41}\,\mathrm{cm}^2$. Astrophysical uncertainties are reflected by the band around each curve. Figure from Agnese et al. (2018).

The observed rate depends on the density and velocity distribution of WIMPs near Earth, on the number of target nuclei as well as on the cross section for elastic scattering of a WIMP from ordinary matter. In the nonrelativistic limit, the latter is the sum of spin and scalar interaction components. The cross section is determined by the couplings of the WIMP with quarks and gluons, the matrix elements of the latter in a nucleon state and the nuclear wave functions. On the one hand, the WIMP possibly couples to the spin of the nucleus, which is referred to as axial-vector or spin-spin interaction. On the other hand, it can couple to the mass of the nucleus in the case of scalar interaction. Both contributions are added together to obtain the total cross section, but usually they are considered separately as distinct experimental set-ups, using either nonzero spin or spin-zero target nuclei, are required. In both cases, the event rates and energy deposited by the WIMP are extremely small (see Fig. 2.14), which is why large detectors with low

backgrounds and long counting times are needed. Despite underground facilities with special shielding, there is an unavoidable background for example from cosmic rays, induced gamma rays and radioactive isotopes in the used materials. This requires sophisticated techniques for the discrimination between such background and possible DM signals.
There are different technologies to measure nuclear recoil. Suitable detector materials are for example scintillator crystals such as NaI used at DAMA (Bernabei et al. 2021), cryogenic crystals such as germanium used at EDELWEISS (Arnaud et al. 2020), superheated fluids used at PICO (Amole et al. 2019) or liquid noble-gases such as argon used at DEAP-3600 (Lai 2023) or xenon used at XENON (Aprile et al. 2017).
Another difficulty besides experimental challenges is the model dependence of the scattering cross sections. In order to calculate exclusion limits in the cross section vs. WIMP mass parameter space, assumptions about the particle physics model have to be made.
However, there is also a lower limit from neutrinos on detectable WIMP events. The so-called neutrino floor is the sensitivity limit at which DM interactions would become undistinguishable from the neutrino background level (see e.g. O'Hare 2021). Fig. 2.15 shows current exclusion limits compared to the upper bound of the neutrino floor.

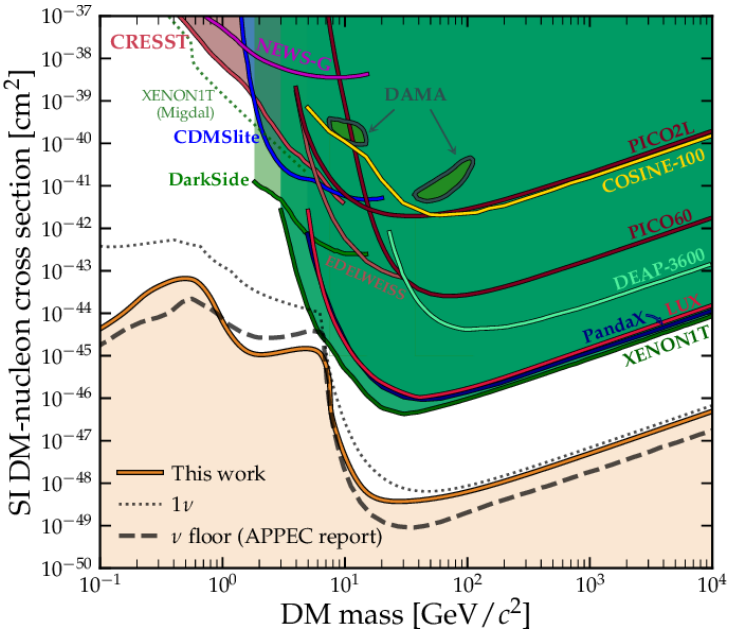

Figure 2.15: Exclusion limits on the spin-independent WIMP-nucleon cross section from different direct detection experiments. Indicated below are different definitions of the neutrino floor for a xenon target. Figure from O'Hare (2021).

2.4.3 Indirect Detection

Although DM and SM particles could only interact weakly, the large abundance of DM in the Universe would lead to a production of a small but possibly measurable amount of ordinary matter in DM dense regions for example through WIMP annihilation and decay.

However, the difficulty of such indirect detection is usually that the expected fluxes are too small to be distinguishable from large astrophysical backgrounds. Nevertheless, there is a variety of detection channels putting limits on DM models. The lectures, provided by Slatyer (2022) at the 2021 Les Houches Summer School on DM, give a comprehensive overview of indirect DM searches which comprise the detection of SM particles produced by DM and their secondary effects. In the following, the primary assumptions and lines of thought for the indirect detection of DM are outlined.

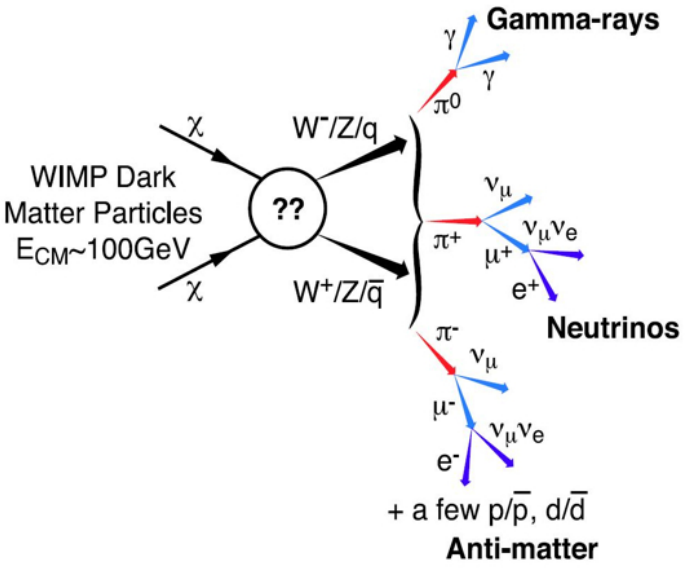

Figure 2.16: WIMP DM annihilates into pairs of SM particles which hadronize and finally decay into stable SM particles, namely photons, electrons/positrons and neutrinos. Figure from NASA[4].

The prompt flux of a SM particle species generated by DM annihilation (decay) depends on astrophysical parameters as well as on the underlying particle physics model (see Ch. 4 for details of the calculations): The J- and D-factors consider that the annihilation and decay rates scale as $\rho(\vec{r})^2$ and $\rho(\vec{r})$, respectively, with $\rho(\vec{r})$ being the three-dimensional DM density distribution. In the center of the DM halo, $\rho(\vec{r})$ is large but subject to large uncertainties as further discussed in Ch. 2.3. Furthermore, the annihilation (decay) rate depends on the cross section (lifetime) of the DM candidate and scales inversely with its mass. The expected flux is a function of the energy of the respective messenger corresponding to the annihilation (decay) spectrum. The latter is highly model-dependent but consists of contributions from possible two-body SM final states, such as ZZ, W^+W^-, $b\bar{b}$, e^+e^-, ..., occurring usually much more frequently than multi-body final states. Note that DM can only annihilate or decay into SM particles whose mass is below or equal to the mass of the DM candidate. The branching ratios of all accessible final states are model-dependent but it is common to calculate experimental constraints on

[4] https://fermi.gsfc.nasa.gov/science/eteu/dm/

individual channels for a generic WIMP. The smaller the WIMP mass, the more will the branching ratios of different channels depend on each other.
However, not all final states are stable and thus subsequently decay into detectable channels such as photons and lightest leptons. The produced SM pairs can be broadly divided into hadronic, leptonic and mere neutrino states as well as into photon line emission based on their final spectra.
τ lepton, gauge boson and quark pairs are referred to as hadronic states as they mainly produce neutral and charged pions and possibly (anti)nuclei. A broad photon continuum is generated by neutral pion decays while charged pions decay into prompt electrons, positrons and neutrinos (see Fig. 2.16). In contrast, from the leptonic channels e^+e^- and $\mu^+\mu^-$, photons can only be produced directly, for example, as part of three-body final states, such as $e^+e^-\gamma$, which are usually suppressed. The muon channel decays into prompt electrons, positrons and neutrinos.

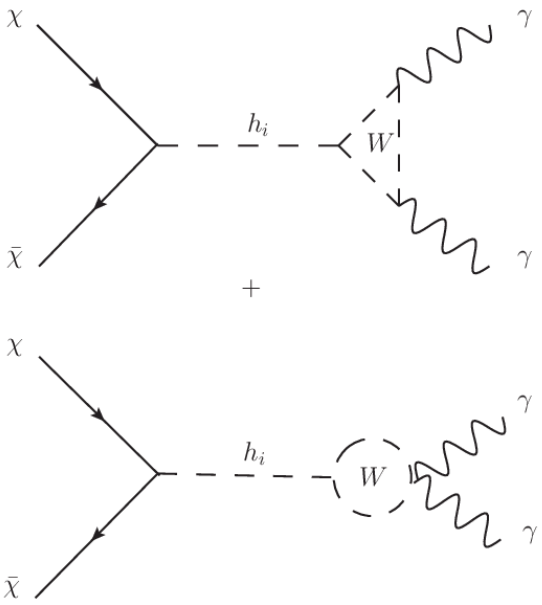

Figure 2.17: Feynman diagrams for WIMP annihilation into a photon pair via W boson loops in the context of a specific DM model where a singlet scalar communicates between DM and SM particles through a coupling to the Higgs. Figure from Franarin et al. (2014).

In principle, DM could also annihilate directly into photons resulting in characteristic line emission. However, this process is suppressed at one-loop level as DM has no electromagnetic charge and therefore cannot couple directly to photons. Fig. 2.17 shows how photons could be produced via loop diagrams in a specific DM model. On the one hand, gamma-ray lines in the GeV range are devoid of large astrophysical backgrounds and would be strong evidence for DM. On the other hand, high statistics and energy resolution are needed to detect any line features. So far, there are limits on gamma-ray lines from GC observations in the GeV range, for example by Fermi (Ackermann et al.

2015a; Foster et al. 2023), and in the MeV range by INTEGRAL for annihilation (Siegert et al. 2024) and decay (Calore et al. 2023). The exclusion limits on the cross section of the two-photon annihilation channel are shown in Fig. 2.18.

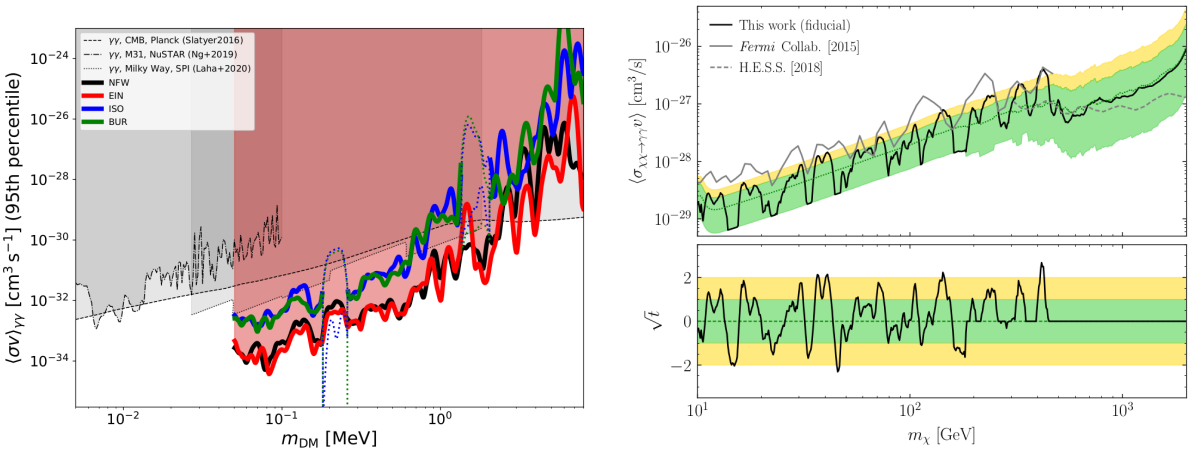

Figure 2.18: Left: Upper limits on the DM annihilation cross section into two photons as a function of particle mass obtained from INTEGRAL observations (Siegert et al. 2024) for different density profiles of the MW halo. **Right:** Same as left but obtained from Fermi observations (Foster et al. 2023) for an NFW profile. In the bottom, the associated sign-weighted significance for detection of an annihilation line is shown. One- and two-sigma containment intervals are depicted in green and yellow, respectively, with the median expected 95th percentile limit in dotted green.

Apart from that, DM could also directly annihilate or decay into neutrinos which are however hard to detect with respect to the large atmospheric neutrino background. Nevertheless, there are constraints from high-energy neutrino telescopes such as ANTARES and IceCube searching for neutrino emission from DM annihilation through different channels in the GC (Albert et al. 2020). Other promising targets to search for neutrino signatures from DM are the Sun or the Earth where a significant amount of DM is expected to accumulate in their centers. Neutrinos would be promising messenger particles which could escape from the overdense central region leading to an unambiguous signal (Baratella et al. 2014). Leane & Linden (2023) applied the same principle to Jupiter and searched for gamma-rays originating from captured sub-GeV DM.

The advantage of neutrino and photon emission produced by DM is that they carry directional information since they are not deflected by magnetic fields. Gamma rays are well suited to put limits on WIMP annihilation. So far, there are upper limits on the cross sections for WIMP masses between 2 GeV and 10 TeV from observations of the Milky Way's dwarf galaxies by Fermi (Ackermann et al. 2015b). Apart from that, Fermi set similar constraints from data of the MW halo (Chang et al. 2018), of galaxy groups (Lisanti et al. 2018) and of the extragalactic background radiation (Ajello et al. 2015). Higher WIMP masses can be probed by ground-based gamma-ray telescopes. There are studies on dwarf

galaxies, e.g. by MAGIC (Acciari et al. 2022), or on the region around the GC, e.g. by HESS (Abdallah et al. 2016).

Prompt emission includes both photons and charged particles which could be detected as CR excesses. However, there would be no information about their directional origin and initial spectrum because electrons and other charged particles diffuse through magnetic fields and lose energy on their way due to their interactions with the interstellar radiation fields and gas. Due to lower backgrounds, antiparticles are interesting detection channels. Adriani et al. (2009) reported an anomalous rise in positron flux from 1.5 to 100 GeV which could be traced to DM annihilation as one possible hypothesis besides astrophysical objects such as pulsars. There have also been claims of an observed antiproton excess in AMS-02 data (Cui et al. 2017). However, the particle measurements near Earth suffer from large uncertainties in the transport of cosmic rays. It can be shown, for example, that the positron excess by AMS-02 and PAMELA may be due to a mismodelling of the propagation (Mauro et al. 2014). Likewise, primary and secondary production and acceleration of antiparticles is only vaguely understood (see e.g. Jean et al. 2009; Siegert 2023).

Most studies focus on DM fluxes expected from the simplest thermal relic scenario (see Sec. 3.3.3). However, there are exotic models and additional effects which can severely modify the annihilation rate. For instance, DM could be asymmetric, i.e. that DM and anti-DM had different abundances determining the point of annihilation freeze-out. There could also have been several DM species in the early Universe leading to coannihilation. It is usually assumed that the velocity averaged cross section $\langle \sigma v \rangle$ is energy independent which is the case for s-wave annihilation where the total orbital angular momentum L of the inital state is zero. It is possible that the s-wave contribution is suppressed and p-wave ($L = 1$) annihilation dominates which scales with the squared velocity of the DM particle (see Boudaud et al. 2019):

$$\langle \sigma v \rangle = \langle \sigma v \rangle_{s\text{-wave}} + \langle \sigma v \rangle_{p\text{-wave}} + ... = \sigma_0 c + \sigma_1 c \left\langle \frac{v_\mathrm{r}^2}{c^2} \right\rangle + \mathcal{O}\left(\frac{v_\mathrm{r}^4}{c^4}\right) \tag{2.7}$$

where σ_0 and σ_1 are model-dependent cross-section terms and $v_\mathrm{r} \ll c$ is the relative WIMP speed. In contrast, there also exist low-velocity enhancements of the annihilation rate through resonance effects due to long-range attractive self-interaction between DM particles (see e.g. Hisano et al. 2005).

Besides searches for WIMP-scale DM, there have also been efforts setting constraints on other DM candidates from MeV observations. For instance, PBHs can be probed in the mass range $10^{16} - 10^{18}$ g by comparing their expected evaporation spectra due to Hawking radiation to X- and gamma-ray observations (see e.g. Berteaud et al. 2022; Iguaz et al. 2021; Siegert et al. 2022b). Light decaying DM, such as axion-like particles, with masses between ∼60 keV and ∼16 MeV has been constrained by Calore et al. (2023) through

INTEGRAL/SPI data.

Model uncertainties, weak signals and large backgrounds pose challenges for the indirect detection of DM, which is restricted to individual photon bands and instruments if only prompt signals are considered. However, charged particles produced by DM annihilation generate strong secondary photon fluxes by IC scattering, bremsstrahlung and synchrotron emission, which are considered in only a few studies. Cirelli et al. (2021, 2023); Cirelli & Panci (2009); Djuvsland et al. (2023) include contributions from IC scattering on Galactic radiation fields and the CMB. Saxena et al. (2011) model a double hump signature from prompt and IC gamma rays for the galaxy M87. Constraints on WIMP DM from secondary synchrotron emission have been set by radio observations (Chan et al. 2019; Regis et al. 2021). Siegert et al. (2022b) include in their analysis of the dwarf galaxy Reticulum II also tertiary emission from positron annihilation.

In this work, a multiwavelength approach is taken for the indirect search of scotogenic WIMP DM in dwarf galaxies considering prompt and secondary emission from IC scattering, bremsstrahlung and synchrotron radiation. The underlying particle physics model is introduced in Ch. 3 while astrophysical assumptions on the DM distribution were discussed in Sec. 2.3.

3 Scotogenic Particle Model

3.1 Motivation

Two main reasons for physics Beyond the Standard Model (BSM) are the needs for massive neutrinos and a neutral stable cold DM candidate. Neutrinos are known to have a non-zero mass due to measured neutrino oscillations between different flavors originating from a changing superposition of mass eigenstates over time (Fukuda et al. 1998). Reasons for the existence of cold DM are given in Sec. 2.1. Similar to supersymmetry, scotogenic models implement an additional $\mathbb{Z}_2$ symmetry under which all SM particles are even while new particles are odd. This symmetry automatically leads to a stable DM candidate and the generation of neutrino masses through couplings to the dark sector (see e.g. Ávila et al. 2020; Ma 2006). One can say that the neutrino masses are *born from darkness* when translating the word *scotogenic* of Greek origin.
The scotogenic model used in this study is classified as *T1-2-A* (Restrepo et al. 2013) with an additional fermionic singlet according to the topology of the one-loop diagram giving rise to neutrino masses (see Fig. 3.2). This model was studied by Alvarez et al. (2023) and is promising since it can additionally explain the muon anomalous magnetic moment and, potentially, the baryon asymmetry of the Universe while fulfilling the current limits for charged lepton flavour violating (cLFV) processes. The magnetic moment of an elementary fermionic particle with charge q, mass m and spin $\vec{S}$ is defined as

$$\vec{\mu} = g\frac{q}{2m}\vec{S}\,. \tag{3.1}$$

The Dirac equation yields exactly $g = 2$ which corresponds to the tree-level Feynman diagram of a particle emitting a photon. The classical result has to be corrected by loop contributions from quantum electrodynamics (QED), electroweak (EW) diagrams, quantum chromodynamics (QCD) and possibly BSM diagrams. The deviation of the g-factor from the classical value of 2 is referred to as the anomalous magnetic moment:

$$a_\alpha = \frac{1}{2}(g-2)_\alpha\,, \tag{3.2}$$

where $\alpha = e, \mu, \tau$. Due to its high mass ($m_\mu \approx 200\, m_e$) and comparably long lifetime ($\tau_\mu \approx 10^7\, \tau_\tau$), the muon is better suited than the electron or tau for the experimental determination of its anomaly. The latest results of the Muon $g-2$ Experiment yield

a new experimental value of $a_\mu^{\text{exp}} = 0.35\,\text{ppm}$ deviating from the theoretical prediction $a_\mu^{\text{SM}} = 0.37\,\text{ppm}$ by 4.2σ (Abi et al. 2021). The uncertainty of the theoretical value of a_μ might be larger than previously assumed due to the challenging calculation of QCD corrections (Borsanyi et al. 2021). Nevertheless, a significant deviation between the experimental and theoretical value of a_μ is a clear sign for new physics (see e.g. Fig. 3.3).
The scotogenic model studied by Alvarez et al. (2023) can provide the experimental value of a_μ while being consistent with current cLFV observables. Processes violating the conservation of flavor have only been observed for quarks and neutrinos but never for charged leptons although they would be allowed theoretically (Ardu & Pezzullo 2022). Examples for cLFV decays are $\mu \to e + X$ and $\tau \to e/\mu + X$ where X could be a photon or an electron-positron pair instead of a neutrino. Additional contributions to the branching ratios of cLFV processes arise in BSM physics but should be kept small in a viable model. The experimental upper limits of the cLFV branching ratios can be found in Workman et al. (2022) and the most important ones have been considered in Alvarez et al. (2023).
On the cosmological side, the need for new physics is not only expressed by the DM problem but also by the unexplained baryon asymmetry in the Universe. It is not clear why more matter than antimatter is *seen* from the production during the Big Bang. Considering that matter and antimatter particles are created in pairs and annihilate to photons, the baryon-to-photon ratio is a measure of the amount of matter survived in the Universe. One possible mechanism explaining this asymmetry is known as leptogenisis, where first a lepton asymmetry is generated, which is then converted into a baryon asymmetry through processes conserving the sum of baryon and lepton number $B + L$. Alvarez et al. (2023) showed that dark leptons in the discussed scotogenic model can drive the leptogenisis and produce the measured value $\eta_\text{B} = 6.1 \times 10^{-10}$ of the baryon-to-photon ratio (Workman et al. 2022).
In summary, what makes the extended scotogenic *T1-2-A* model interesting is that its parameter space offers the possibility to explain DM, neutrino masses, the muon $(g-2)$ and the baryon asymmetry simultaneously, while being consistent with cLFV upper limits. In the following, the particle content and parameters of this model as well as the determination of viable DM candidates are discussed.

3.2 Field Content and Model Parameters

In the scotogenic model discussed by Alvarez et al. (2023) the SM is extended by a scalar doublet η with respect to $SU(2)$, a scalar singlet S, two Weyl fermion doublets Ψ_1 and Ψ_2 and two Majorana fermion singlets F_1 and F_2 (see Tab. 3.1). All new particles are odd under a $\mathbb{Z}_2$ symmetry and singlets with respect to $SU(3)$.

The scalar potential of the Lagrangian including the new fields is given by:

	Ψ_1	Ψ_2	F_1	F_2	η	S
$SU(2)_L$	2	2	1	1	2	1
$U(1)_Y$	-1	1	0	0	1	0

Table 3.1: Field content of the scotogenic model in addition to the SM fields. The fermionic sector is extended by two doublets with respect to $SU(2)$ and two singlets. In the scalar sector one doublet and one singlet is added. The second row denotes the hypercharge with respect to gauge symmetry $U(1)$.

$$\begin{aligned} V_{\text{scalar}} = {} & M_{\text{H}}^2|H|^2 + \lambda_{\text{H}}|H|^4 + \frac{1}{2}M_S^2 S^2 + \frac{1}{2}\lambda_{4S}S^4 + M_\eta^2|\eta|^2 + \lambda_{4\eta}|\eta|^4 + \frac{1}{2}\lambda_S S^2|H|^2 + \\ & \frac{1}{2}\lambda_{S\eta}S^2|\eta|^2 + \lambda_\eta|\eta|^2|H|^2 + \lambda'_\eta|H\eta^\dagger|^2 + \frac{1}{2}\lambda''_\eta\Big[(H\eta^\dagger)^2 + \text{h.c.}\Big] + \alpha\Big[SH\eta^\dagger + \text{h.c.}\Big]\,, \end{aligned} \tag{3.3}$$

where H is the SM Higgs doublet. The Lagrangian containing the new fermions consists of a kinetic term, a mass expression and a Yukawa sector describing the interaction between scalar and fermionic fields:

$$\begin{aligned} \mathcal{L}_{\text{fermion}} = {} & i(\bar{\Psi}_j\sigma^\mu D_\mu\Psi_j + \frac{1}{2}\bar{F}_j\sigma^\mu\partial_\mu F_j) - \frac{1}{2}M_{F_{ij}}F_iF_j - M_\Psi\Psi_1\Psi_2 \\ & - y_{1i}\Psi_1 H F_i - y_{2i}\Psi_2\tilde{H}F_i - g_\Psi^k\Psi_2 L_k S - g_{F_j}^k\eta L_k F_j - g_R^k e_k^c\tilde{\eta}\Psi_1 + \text{h.c.}\,, \end{aligned} \tag{3.4}$$

where $i,j = \{1,2\}$ and L_k and e_k^c are the left-handed SM lepton doublets and the right-handed charged SM lepton singlets with flavors $k = \{e,\mu,\tau\}$. The Majorana masses and couplings between the fields are marked in blue as they are the modifiable parameters of the model which are subject to certain constraints as discussed in the Sec. 3.3. In order to illustrate some of the new interactions, Fig. 3.1 shows Feynman diagrams which contribute to the charge conjugation parity (CP) asymmetry generated in the decays of the new fermion singlets F_i. The decays displayed in Fig. 3.1 lead to a production of left-handed SM leptons L_k possibly resulting in a lepton asymmetry which could be converted to a baryon asymmetry in the Universe.

The physical particles stemming from the new fields only arise after elektroweak symmetry breaking (EWSB). The new particles are the neutral scalars, Φ_1^0 and Φ_2^0, the neutral pseudoscalar (CP-odd) Φ_3^0 and the charged scalars $\eta^\pm$. In the fermionic sector, there is the charged fermion χ^- and four neutral Majorana fermions χ_i^0. The mass spectra of the particles obtained by diagonalizing the resulting mass matrices are given in Alvarez et al. (2023). Relevant for the search of a DM candidate is the lightest neutral particle of the scalar, pseudoscalar and fermionic sector, respectively.

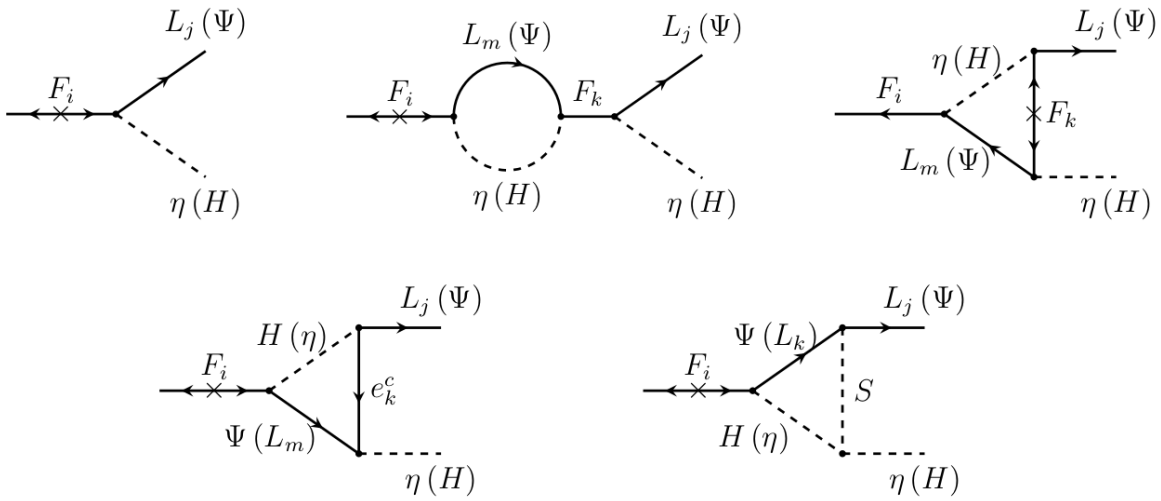

Figure 3.1: Contributions to the CP asymmetry generated in the decays of the new fermion singlets F_i in the gauge basis. The corresponding couplings can be found in Eqs. 3.3 and 3.4. Figure from Alvarez et al. (2023).

3.3 Exploration of the Parameter Space

The initially free parameters of the model are the couplings and masses in Eqs. 3.3 and 3.4, marked in blue, and the lightest neutrino mass. The couplings of the new fields to the SM leptons are constrained by neutrino oscillation data and cLFV upper limits and are fitted by Alvarez et al. (2023) in a way that they reproduce the experimental value of a_μ. Further constrained by the Higgs mass $m_{\mathrm{H}} = (125.3 \pm 1.0)\,\mathrm{GeV}$ (Workman et al. 2022) and DM relic density $\Omega_{\mathrm{CDM}}h^2 = 0.120 \pm 0.012$ (Aghanim et al. 2020), a model parameter scan of Alvarez et al. (2023) showed that fermionic DM with a mass around 1.1 TeV is preferred among viable DM candidates. In the following, the implementation of the constraints from neutrino data, $(g-2)_\mu$, cLFV and DM observables is further specified. A detailed study of the parameter space of the scotogenic model can be found in Alvarez et al. (2023).

3.3.1 Neutrino Masses

At tree-level, neutrino masses can be generated by a model known as Seesaw mechanism (Mohapatra et al. 2005). For instance, a set of heavy right-handed neutrinos, that are singlet fermions in the Seesaw type 1 case, are added to the SM giving rise to a Majorana mass term.

In the scotogenic model, introduced in Sec. 3.2, neutrino mass generation is suppressed at tree-level but becomes possible through the one-loop diagram depicted in Fig. 3.2. After EWSB, each loop involves one of the neutral scalars and one of the neutral fermions. The relevant couplings for the neutrino mass generation are the nine Yukawa couplings g_Ψ^k and

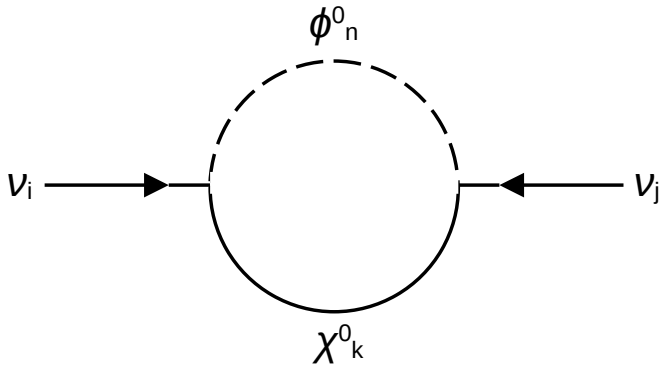

Figure 3.2: Generation of neutrino masses at one-loop level after EWSB. The loop contains one of the neutral scalars Φ^0_n, $n = \{1, 2, 3\}$, and one of the neutral fermions χ^0_k, $k = \{1, 2, 3, 4\}$.

$g^k_{F_j}$ between the new fields and the left-handed SM leptons and can be expressed in terms of neutrino oscillation data with three remaining degrees of freedom.

3.3.2 The Muon anomalous magnetic Moment and cLFV Decays

The new fields also contribute to the calculation of the muon anomalous magnetic moment a_μ. The leading contributions involve the coupling g^μ_R of the new fields to the right-handed muon and are shown in Fig. 3.3 in the mass basis after EWSB. The diagrams in Fig. 3.3 contribute as well to the cLFV decays $\mu \to e\gamma$ and $\tau \to \mu\gamma$. Especially the first is strongly constrained by the experimental upper limit to its branching ratio of $\mathrm{BR}[\mu \to e\gamma] < 4.2 \times 10^{-13}$ (Baldini et al. 2016). All remaining cLFV observables set as constraints can be found in Tab. 2 in Alvarez et al. (2023). They showed that for a selected region of the parameter space it is possible to produce the measured value of $a^{\mathrm{BSM}}_\mu = a^{\mathrm{exp}}_\mu - a^{\mathrm{SM}}_\mu = (251 \pm 59) \times 10^{-11}$ (Abi et al. 2021) while keeping the cLFV contributions under control by using g^μ_R and the remaining degrees of freedom in g^k_Ψ and $g^k_{F_j}$.

3.3.3 Dark Matter Observables

WIMPs are believed to have been produced thermally in the early Universe (Jungman et al. 1996, see e.g. review by). The idea of a thermal relic particle χ is that it has been in thermal equilibrium with the primordial plasma at temperatures above the mass m_χ of the particle. This means that an equivalent amount of particle-antiparticle pairs $\chi\bar{\chi}$ is constantly being created and destroyed by annihilation into other particles. With the expansion of the Universe, its temperature decreases and as soon as it drops below m_χ, no more pairs $\chi\bar{\chi}$ are produced and eventually their number density decreases exponentially.

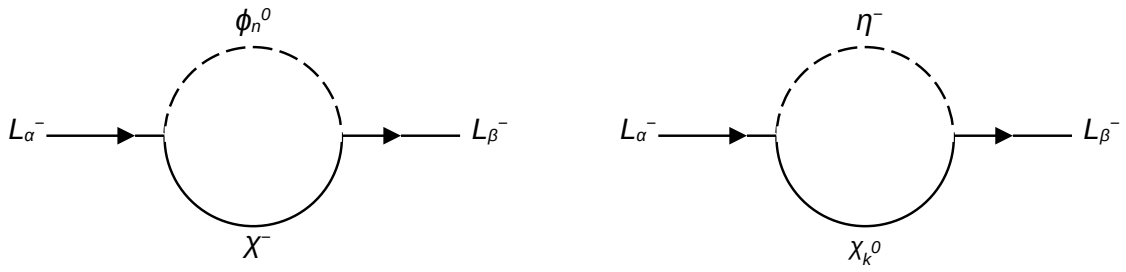

Figure 3.3: Leading contributions to the magnetic moment a_α of the charged left-handed SM leptons L_α^-, where $\alpha = \{e, \mu, \tau\}$, and to cLFV decays in the mass basis after EWSB. The loop contains either the charged fermion χ^- and a neutral scalar Φ_n^0, $n = \{1, 2, 3\}$, or the charged scalar η^- and one of the neutral fermions χ_k^0, $k = \{1, 2, 3, 4\}$.

The destruction of $\chi\bar{\chi}$ stops as soon as the annihilation rate of the particle is lower than the expansion rate of the Universe resulting in a constant number density of χ, which is equivalent to its relic cosmological abundance. This is known as the freeze-out mechanism and can be described by the Boltzmann equation:

$$\frac{dn_\chi}{dt} + 3Hn_\chi = -\langle\sigma v\rangle[(n_\chi)^2 - (n_\chi^{\mathrm{eq}})^2]\,, \tag{3.5}$$

where $n_\chi(t)$, $H(t)$, $\langle\sigma v\rangle$ and $n_\chi^{\mathrm{eq}}(t)$ are the number density of the particle χ, the Hubble expansion rate, the thermally averaged annihilation cross section and the equilibrium number density. The first term on the right-hand side of Eq. 3.5 describes the annihilation of χ, whereas the second term accounts for the creation of χ. If $n_\chi = n_\chi^{\mathrm{eq}}$, the rates of destruction and creation of the thermal particle are equal, consequently the right-hand side of Eq. 3.5 is zero. Since $H(t) = \dot{a}(t)/a(t)$, where a is the scale factor of the Universe, it follows that $n_\chi^{\mathrm{eq}} \propto a^{-3}$. The numerical solutions of Eq. 3.5 are plotted in Fig. 3.4 for different annihilation cross sections.

As long as the decrease of number density due to expansion is negligible, n_χ follows the equilibrium density n_χ^{eq}. At a certain freeze-out temperature T_{f}, where the annihilation rate is equal to the expansion rate, n_χ drops out of equilibrium and remains constant. The larger the annihilation cross section, the later the particles freeze-out resulting in a smaller relic abundance. Assuming that the annihilation cross section $\langle\sigma v\rangle$ is energy independent, the relic abundance in units of the critical density can be derived from the freeze-out condition to be approximately (Jungman et al. 1996):

$$\Omega_\chi h^2 = \frac{m_\chi n_\chi}{\rho_{\mathrm{c}}} \simeq \frac{3 \times 10^{-27}\,\mathrm{cm^3\,s^{-1}}}{\langle\sigma v\rangle}\,. \tag{3.6}$$

According to Bauer & Plehn (2018), the annihilation cross section of a particle heavier than the Z-boson ($m_\chi > m_Z = 91\,\mathrm{GeV}$) interacting on the weak scale (energy scale

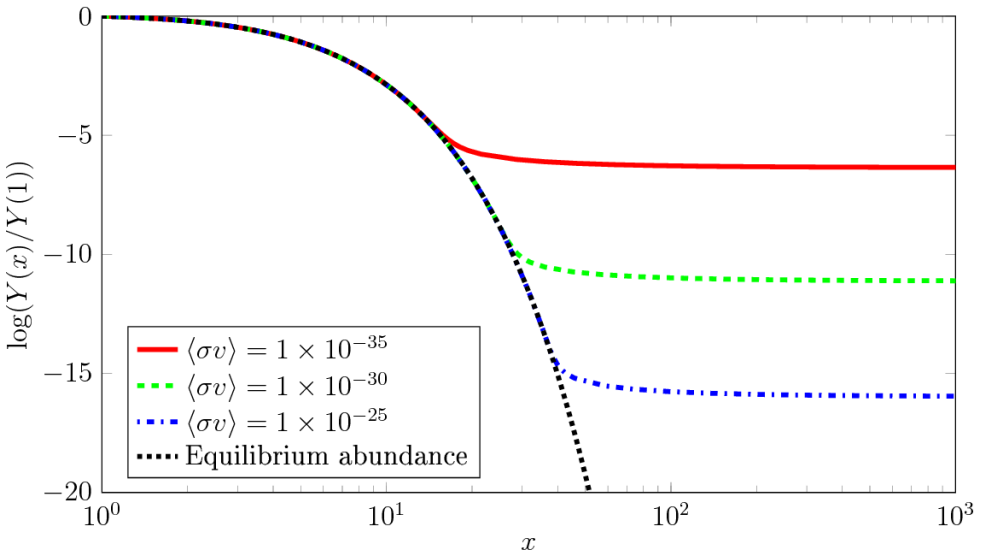

Figure 3.4: Numerical solutions of the Boltzmann equation (see Eq. 3.5). $x = m_\chi/T$ is a measure of the time evolution. The variable $Y = n_\chi/s$ is the number density divided by the entropy density s. Figure from Alp & Modée (2014).

around 250 GeV) is of the order $\langle\sigma v\rangle \approx 2 \times 10^{-26}\,\mathrm{cm}^3\,\mathrm{s}^{-1}$ corresponding to a relic density $\Omega_\chi h^2 \approx 0.15$. The fact that this is close to the measured DM abundance (see Sec. 2.1.2) is known as "WIMP miracle". While Eq. 3.6 is used as a canonical value, Steigman et al. (2012) calculated the cross section required for the observed DM density as a function of WIMP mass (see Fig. 3.5).

Alvarez et al. (2023) takes the observed DM relic density as an explicit constraint in the MCMC (Markov chain Monte Carlo) scan of the parameter space. For this purpose, they use `micrOMEGAs`, a code written in *C* to compute WIMP properties for direct and indirect detection given certain particle interactions (Belanger et al. 2014). To calculate the relic density, `micrOMEGAs` solves Eq. 3.5 numerically without any approximation. Therefore, the co-annihilation of all pairs of supersymmetric particles into some SM particles is considered in the annihilation cross section $\langle\sigma v\rangle$ (see Eq. 21 in Bélanger et al. 2006). The annihilation cross section of the DM candidate depends strongly on whether it has SM gauge interactions or not. Alvarez et al. (2023) found that in the case of SM gauge doublets yielding the observed relic abundance, the allowed mass range is strongly constrained: for scalar DM it is in the range of 650–750 GeV and for fermionic DM the corresponding range is 1000–1100 GeV.

Alvarez et al. (2023) also excluded points in the parameter space which do not satisfy the upper limit for the spin-independent direct detection cross section σ_{SI} set by the XENON1T experiment (Aprile et al. 2018). Fig. 2.15 shows the XENON1T limits of σ_{SI} as a function of WIMP mass. However, there are no constraints from direct detection in the case of fermionic DM since its cross section is below the neutrino floor.

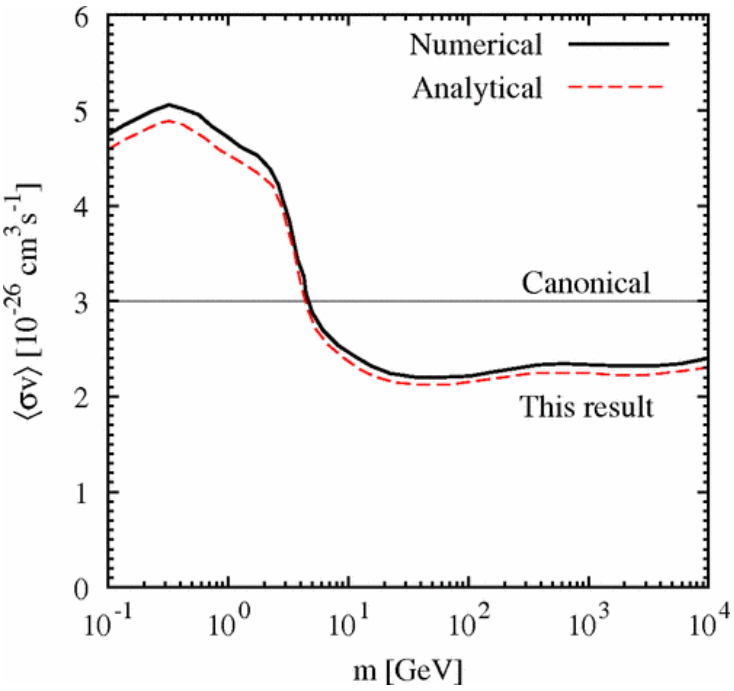

Figure 3.5: The thermal annihilation cross section required for a DM density of $\Omega_\chi h^2 = 0.11$ as a function of WIMP mass compared to the canonical value (see Eq. 3.6). Figure from Steigman et al. (2012).

3.4 Dark Matter Candidates

In summary, the scotogenic model has three types of possible DM candidates: the lightest dark neutral fermion χ_1^0, the lighter scalar Φ_1^0 or the pseudo-scalar Φ_3^0. Setting constraints on the relic density leads to a preference of fermionic DM with a mass around 1.1 TeV. The spin-independent direct cross section of all fermionic DM candidates is far below the experimental limits meaning that there are no further constraints. Another finding in favor of fermionic DM is that 25 out of 26 points in the parameter space, which possibly explain the baryon asymmetry via leptogenisis, suggest a fermionic DM candidate. For this reason, a viable point of the parameter space resulting in a fermionic WIMP DM type with $m_\chi = 1050\,\text{GeV}$ stemming mainly from a $SU(2)_L$ doublet is chosen for the following analysis.

Now that the parameters of the scotogenic model are specified, the annihilation cross section $\langle \sigma v \rangle$ and spectra can be computed by `micrOMEGAs` (see Sec. 4.1).

The methodology and results presented in Ch. 4–7 have been published in MNRAS (Eisenberger et al. 2024). In this thesis, the detailed descriptions are provided.

4 Indirect Multiwavelength Approach

The indirect search for DM is often restricted to the high-energy photons directly produced by DM annihilation (primary emission). Many studies focus on individual photon bands and instruments, for example, Fermi/LAT (e.g. Ackermann et al. 2017, 2014), MAGIC (e.g. MAGIC_Collaboration 2016), HESS (e.g. Abdalla et al. 2022), or INTEGRAL (e.g. Siegert et al. 2022b). Such prompt signals alone are dominated by systematic uncertainties and are probably too weak to be measurable in large astrophysical fore- and backgrounds, as shown in this work (see Ch. 6). WIMP annihilation generates photons directly but also highly energetic leptons which again produce strong fluxes of electromagnetic radiation via IC scattering, bremsstrahlung and synchrotron radiation, among other weaker subsequent emission processes. Following a multiwavelength approach, this secondary emission from charged annihilation products should be also taken into account which has only been attempted by a few studies (e.g., Acciari et al. 2022; Cirelli et al. 2021, 2023; Cirelli & Panci 2009; Djuvsland et al. 2023; Saxena et al. 2011).

In this chapter, it is presented how the primary and secondary spectra, customized for the dwarf galaxies of the MW, are calculated.

4.1 Primary/Prompt Emission

DM particles annihilate into pairs of SM particles which hadronize and finally decay into stable SM particles, which is referred to as prompt emission (see Fig. 2.16). The differential flux of a particle species a produced directly by annihilation of Majorana DM particles and measured from the direction ψ is

$$\frac{d\Phi_a}{dE} = \frac{1}{4\pi} \frac{\langle \sigma v \rangle}{2m_\chi^2} \frac{dN_a}{dE} \times J(\psi) \tag{4.1}$$

where $\langle \sigma v \rangle$, m_χ and dN_a/dE are the thermally-averaged annihilation cross section (see Sec. 3.3.3), the mass of the DM particle (see Sec. 3.4), and the distribution of the produced particle a per annihilation, respectively. The second part of Eq. (4.1) is referred to as the astronomical "J-factor" and incorporates the astrophysical dependencies:

$$J = \frac{1}{\Delta\Omega} \int_{\Delta\Omega} d\Omega \int_{\text{los}} \rho^2(\psi, l)\, dl\,. \tag{4.2}$$

It consists of the line-of-sight integral over the squared DM density $\rho(\psi, l)$, averaged over the chosen solid angle $\Delta\Omega$.

The annihilation cross section and the direct annihilation spectra dN_a/dE depend on the respective particle model. For the calculation in this work, `micrOMEGAs`, a code written in *C* to compute DM properties (Belanger et al. 2014), is used (see Sec. 3.3.3). Therefore, the parameters of the chosen scotogenic model, where $m_\chi = 1.05\,\text{TeV}$ (see Sec. 3.4), are used as input to `micrOMEGAs`. `micrOMEGAs` evaluates $\langle\sigma v\rangle$ in the limit $v = 0$, which is a good approximation for s-wave annihilation. To generate the annihilation spectra for a given particle model, `micrOMEGAs` first computes the cross sections for all channels with two body SM final states (ZZ, W^+W^-, $b\bar{b}$, e^+e^-, ...), which are finally used to create spectra for interesting stable SM particles (γ, $e^{-/+}$, $\nu_{e/\mu}$, ...) with `Pythia`, a Monte Carlo generator (Sjöstrand et al. 2015).

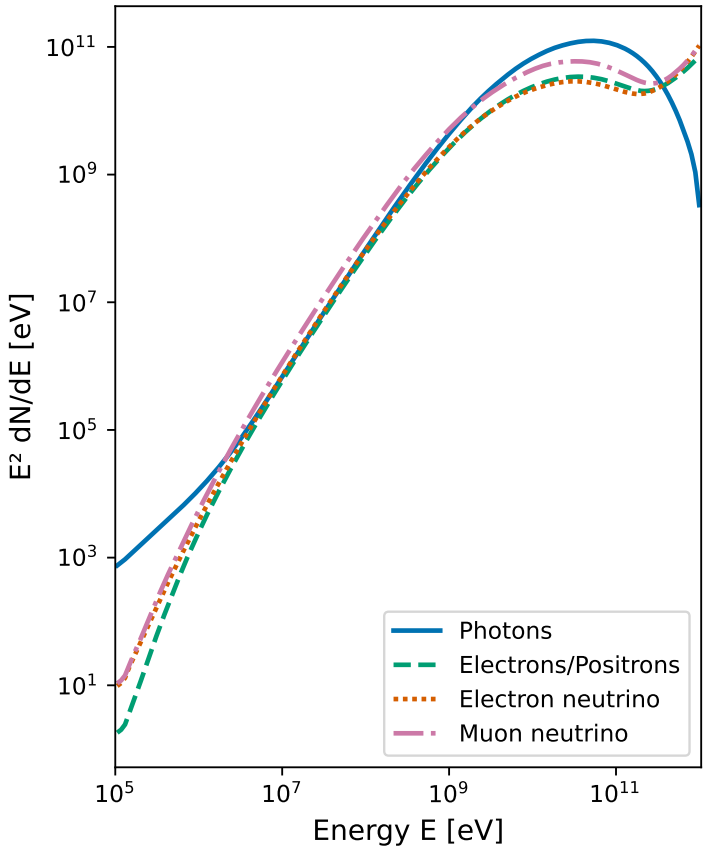

Figure 4.1: Annihilation spectra of the scotogenic WIMP candidate with a mass of 1.1 TeV computed by `micrOMEGAs`. The distributions refer to different particles produced per annihilation. The underlying scotogenic model is described in Chapter 3.

The annihilation cross section was determined to be $\langle\sigma v\rangle = 9.52 \times 10^{-27}\,\text{cm}^3\,\text{s}^{-1}$ for the chosen DM candidate. The main channels of the scotogenic WIMP DM annihilation are $\chi\chi \to W^+W^-$ (51.7 %) and $\chi\chi \to ZZ$ (41.6 %). Fig. 4.1 shows the final distributions of γ-rays, electrons, positrons and neutrinos per annihilation for the scotogenic model described

in Chapter 3. Note that the electron and positron spectra are identical. The computation of the annihilation spectra is limited to a minimum energy of $E_{\mathrm{min}} = 10^{-7}\, E_{\mathrm{max}}$, where $E_{\mathrm{max}} = 1.1\,\mathrm{TeV}$ is the mass of the annihilating DM particle. All spectra exhibit a (local) maximum at around 50 GeV, which corresponds to 5% of the DM mass and is expected for pion decays after hadronization. It should be noted that no line feature was calculated for the photon spectrum since direct annihilation into γ-rays is loop-suppressed. Electrons and electron neutrinos are produced at the same amount by charged pion decays leading to similar spectra, while twice as many muon neutrinos are created per pion decay (see Fig. 2.16). The second peak of the electron and neutrino spectrum at the maximum energy around 1 TeV stems from the decay $W^{\pm} \rightarrow e^{\pm} + \nu_e/\bar{\nu}_e$, where one of the decay products carries almost the entire energy of the DM particle.

While the annihilation spectra of photons and neutrinos can be directly converted into observable fluxes according to Eq. 4.1 (primary emission), the propagation of charged particles is governed by diffusion and energy losses and depends on magnetic and radiation fields. The relativistic electrons and positrons will lead to secondary photons (see Sec. 4.2). The importance of neutrinos generated by DM annihilation is discussed in Sec. 4.3.

4.2 Secondary Gamma-Ray Emission

Charged particles produced by DM annihilation will interact with their environment and thereby create gamma-rays via different mechanisms.
Highly energetic electrons and positrons will IC scatter off the low-energy photons of the interstellar radiation field (ISRF) (see Fig. 4.2) consisting of approximately three blackbody spectra of different temperatures: the CMB, the infrared (IR) dust emission and the optical starlight (SL), where $T_{\mathrm{CMB}} = 2.753\,\mathrm{K}$, $T_{\mathrm{IR}} \approx 3.5\,\mathrm{meV}$ and $T_{\mathrm{SL}} \approx 0.3\,\mathrm{eV}$ (e.g., Cirelli & Panci 2009). While the CMB photon field is present everywhere to the same amount, the IR and SL photon densities depend on the respective environment. Due to the low content of dust in dwarf spheroidal galaxies, the IR photon field is assumed to be negligible in this case. The energy density of the SL photon field depends on the average temperature of the stellar population and on the luminosity and size of the respective galaxy.

Bremsstrahlung is produced when relativistic particles interact with another charged particle population and therefore depends on the particle density of the respective surroundings. Since dwarf galaxies are probably devoid of interstellar medium (ISM), the DM contribution to bremsstrahlung in the further vicinity of the MW halo is expected to be subdominant but calculated here for completeness.
Under presence of magnetic fields, charged particles are deflected and thus emit synchrotron radiation. In dwarf galaxies, in which the magnetic field might only be a factor of a few larger than that of the intergalactic medium, the synchrotron emission due to

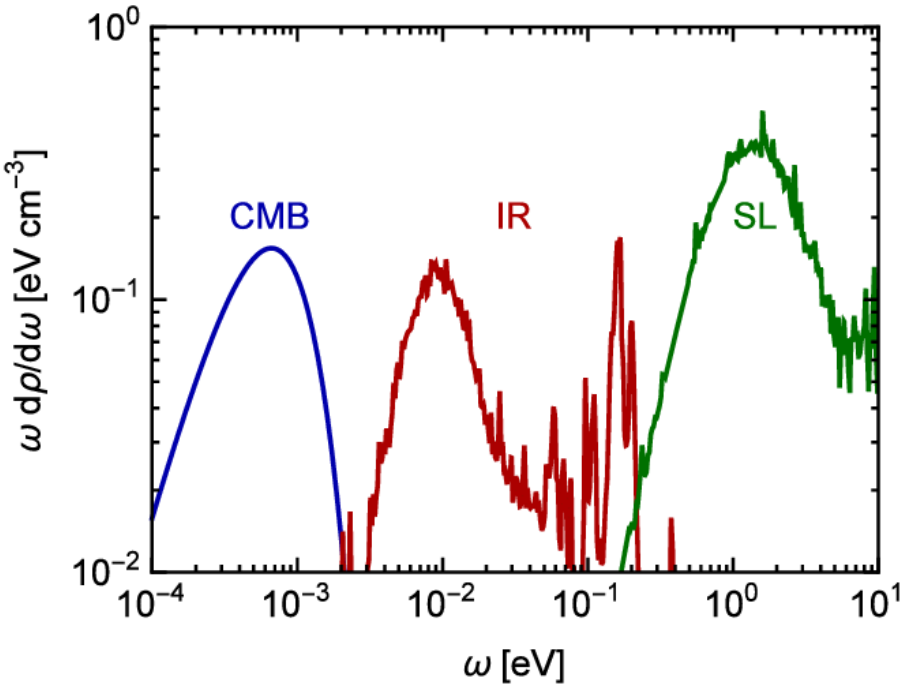

Figure 4.2: Interstellar radiation field of the MW consisting of approximately three blackbody spectra: the CMB, the infrared (IR) emission and the starlight (SL). Figure from Dobrynina et al. (2015).

particles from DM is expected to be weak, but nevertheless relevant for a multiwavelength analysis. The calculation of the secondary emission (IC, bremsstrahlung and synchrotron) is performed with the `Naima` `Python` package (Zabalza 2015), which uses the total number of electrons/positrons n_e per unit energy as input. Given the number of electrons dN/dE per annihilation as calculated by `micrOMEGAs`, n_e is determined in a certain region. Therefore, the diffusion-loss equation for electrons in each point of the volume would have to be solved (Cirelli & Panci 2009):

$$-\frac{1}{r^2}\frac{\partial}{\partial r}\left[r^2 D \frac{\partial n_\mathrm{e}}{\partial r}\right] + \frac{\partial}{\partial p}\left[\dot{p}\, n_\mathrm{e}\right] = Q_\mathrm{e}(E, r)\,, \tag{4.3}$$

where D, p and $Q_\mathrm{e}(E, r)$ are the diffusion coefficient, the electron momentum and the source term depending on the electron energy E. While advection and convection are neglected, the first and second term of Eq. 4.3 describe diffusion and radiative losses respectively. Following the approach of Cirelli & Panci (2009), it is assumed that the electrons radiate all their energy at the point where they are produced. Neglecting diffusion, Eq. 4.3 is solved in the highly relativistic regime by

$$n_\mathrm{e}(E) = \frac{1}{b(E)} \int_E^{m_\chi} Q_\mathrm{e}(\tilde{E})\, d\tilde{E}\,, \tag{4.4}$$

where $b(E)$ is the total rate of electron energy loss. The maximum energy of the electrons produced by DM annihilation corresponds to the mass m_χ of the DM particle. For a point source at distance d, the luminosity source term of DM annihilation is given by

$$Q_{\rm e}(E) = \frac{d\Phi_{\rm e}(E)}{dE} \times 4\pi d^2 \,, \tag{4.5}$$

where the differential flux $d\Phi_{\rm e}/dE$ for electrons/positrons is given by Eq. 4.1. The energy losses of IC, synchrotron and bremsstrahlung are summed up in the function $b(E)$ in Eq. (4.4). As the produced electrons are mostly relativistic, the following formulas are presented in their high-energy limits. The synchrotron and IC losses (Aharonian et al. 2010; Khangulyan et al. 2014) are both given by

$$b(E)_{\rm IC/Syn} = \frac{4}{3}\sigma_{\rm T} c U_{\rm rad/B} \left(\frac{E}{E_0}\right)^2 , \tag{4.6}$$

where $\sigma_{\rm T}$, $U_{\rm rad/B}$ and E_0 are the Thomson cross section, the energy density of the respective field, and the electron rest energy, respectively. The energy losses of electron-electron bremsstrahlung (Baring et al. 1999) are calculated by

$$b(E)_{\rm e\text{-}e} = \frac{e^6 n_0 \ln(192)}{12\pi^3 \epsilon_0^3 \hbar E_0} \frac{E}{E_0} \,, \tag{4.7}$$

where n_0 is the density of the electron gas.

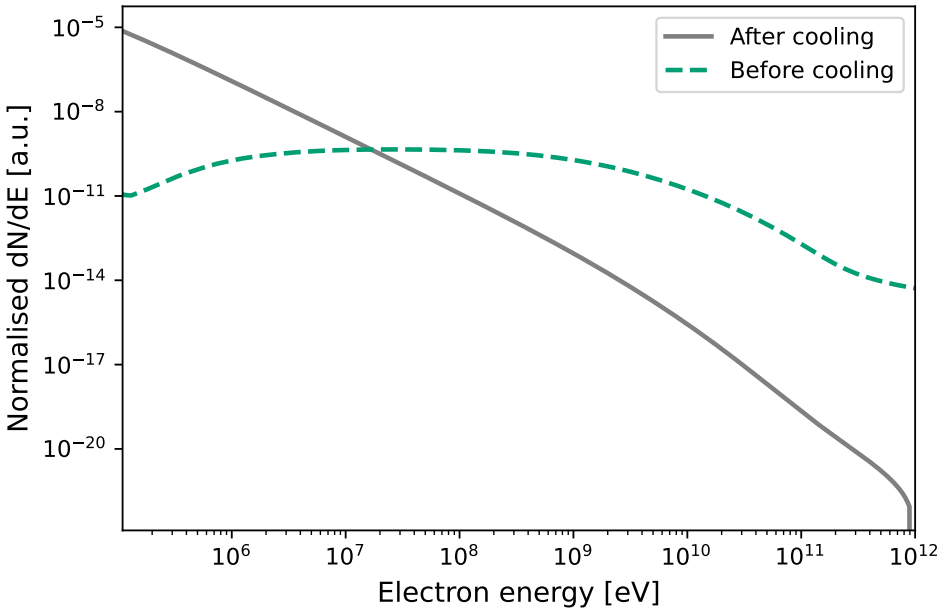

Figure 4.3: Normalised distribution of electrons/positrons before and after radiative cooling. The green dashed spectrum corresponds to the electron annihilation spectrum in Fig. 4.1. The gray spectrum is calculated from Eq. 4.4 including IC, synchrotron and bremsstrahlung losses.

Fig. 4.3 shows the normalised distribution of electrons/positrons before and after radiative cooling in a steady state corresponding to the annihilation spectrum dN_e/dE (see Fig. 4.1) and n_e (see Eq. 4.4), respectively. As expected, radiative energy losses of the charged particles lead to a steepening of the spectrum towards lower energies. In the following subsections, it will be explained how the photon spectrum is computed from the electron spectrum n_e for each process. A detailed derivation of the general IC, synchrotron and bremsstrahlung spectrum can be found in Blumenthal & Gould (1970) or Cirelli & Panci (2009).

4.2.1 Inverse Compton scattering

The CMB with a temperature of $T = 2.7\,\mathrm{K}$ and a radiation energy density of $U_{\mathrm{CMB}} = 0.26\,\mathrm{eV\,cm^{-3}}$ is the most relevant photon field for IC scattering of electrons in dwarf galaxies. The SL radiation field can be estimated from the absolute visual magnitude M_V of a source and its half-light radius r. The energy density is then approximately given by

$$U_{\mathrm{SL}} = \frac{f_V}{4\pi c r^2} L_\odot \times 10^{0.4(M_{V,\odot} - M_V)}\,, \tag{4.8}$$

where a scaling factor f_V takes into account the fact that the approximate blackbody spectrum extends outside of the visual range. In other words, f_V is the ratio of total to visual luminosity of the galaxy (see Eq. 4.9). The solar parameters are needed as a scale to convert magnitude into luminosity.

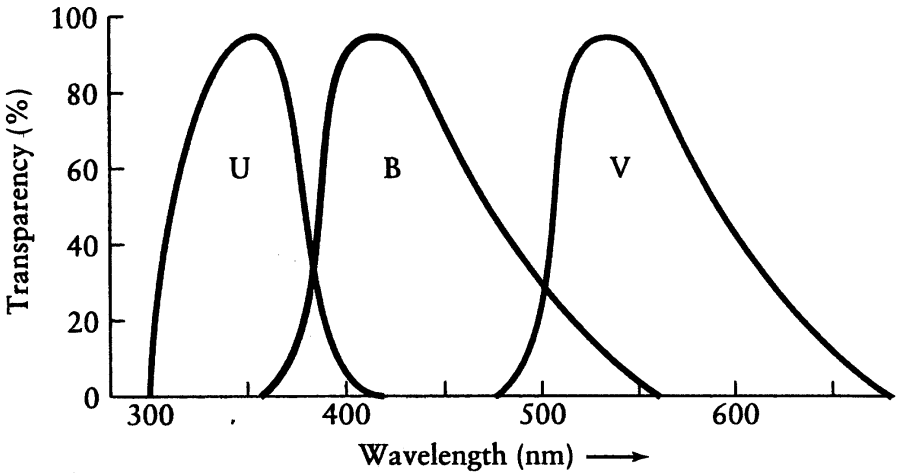

Figure 4.4: Spectral range of UBV filters (Johnson & Morgan 1953). The U-, B- and V-bands are centered on the ultraviolet, blue and visual range, respectively. Figure from Hawley Lectures[1].

[1] https://www.astro.bas.bg/~petrov/hawley99.html

Given the single data points for the visual magnitude, and therefore luminosity, the total spectrum of dwarf galaxies cannot be determined and therefore it is difficult to estimate f_V directly. Since dwarf galaxies are characterized by an older stellar population, the temperature of the SL photon field is estimated to be around 5000 K. Therefore, the spectrum can be approximated by a 5000 K blackbody spectrum that meets the observed visual flux. The V-band filter (Johnson & Morgan 1953) is almost Gaussian-shaped with a peak around 540 nm and a FWHM of 40 nm (see Fig. 4.4). Integrating a 5000 K blackbody spectrum $B_\lambda(T)$ over this range, the flux included in the V-band is found to be about 1% of the total flux, which would correspond to a value of f_V of 100 according to:

$$f_\mathrm{V} = \frac{\int_0^\infty B_\lambda(T)\,d\lambda}{\int_\mathrm{V} B_\lambda(T)\,d\lambda}\,. \tag{4.9}$$

The V-band flux for blackbody spectra of different temperatures is visualized in Fig. 4.5. Because the average temperature is also uncertain, a conservative approach is used and f_V is set to 1 in the estimates for the SL IC contribution.

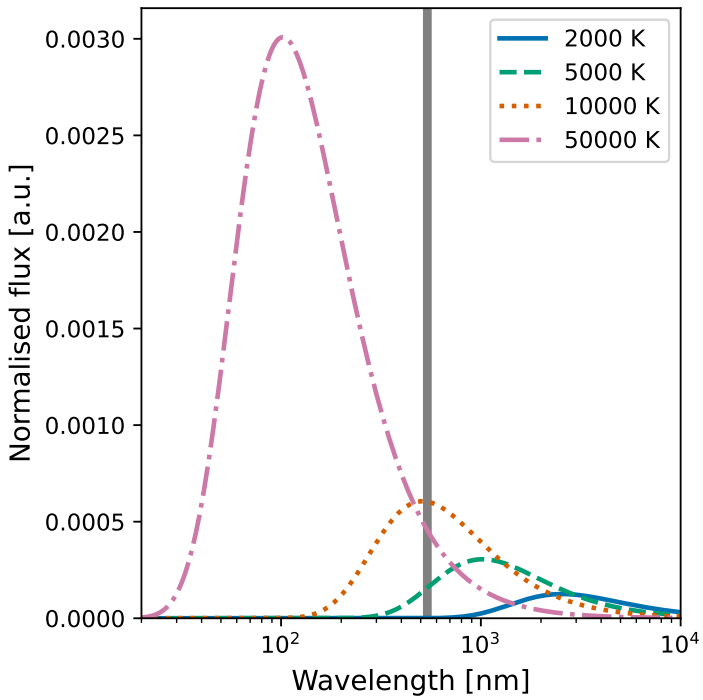

Figure 4.5: Blackbody spectra for a stellar temperature range reaching from the coldest class-M to the hottest class-O stars. The spectra are normalised by the total flux integrated over all wavelengths. The V-band (520-560 nm) is indicated by the gray line. For temperatures hotter than 10000 K, the ratio of visible flux to total flux is decreasing again.

For faster computation the `Naima` package uses the analytical approximation from Khangulyan et al. (2014) for the interaction rate of charged particles with an isotropic blackbody target photon field of temperature T:

$$\left(\frac{dN}{d\omega\, dt}\right)_{\mathrm{IC}} = \frac{2e^4 E_0 \kappa T^2}{\pi\hbar^3 c^2 E^2} \times \left[\frac{z^2}{2(1-z)} F_3(x_0) + F_4(x_0)\right], \tag{4.10}$$

where $x_0 = \frac{z}{4ET(1-z)}$ and $z = \frac{\omega}{E}$ is the ratio of photon and electron energy. The functions $F_3(x_0)$ and $F_4(x_0)$ can be found in Khangulyan et al. (2014). The dilution factor κ is smaller than 1 in the case of greybody radiation and is defined by the ratio of the actual radiation energy density U_{rad} to the blackbody energy density:

$$\kappa = \frac{cU_{\mathrm{rad}}}{4\sigma_{\mathrm{SB}} T^4}\,. \tag{4.11}$$

Finally, the differential spectrum of a point source at distance d is given by

$$\frac{d\Phi}{d\omega} = \frac{1}{4\pi d^2} \int_{E_{\mathrm{min}}}^{E_{\mathrm{max}}} 2n_{\mathrm{e}}(E) \times \frac{dN}{d\omega\, dt}\, dE\,, \tag{4.12}$$

where E_{min} is the lower bound of the electron spectrum shown in Fig. 4.1 and E_{max} is the mass m_χ of the DM particle. The factor of 2 takes into account the equal amounts of positrons and electrons produced by DM annihilation. The number of electrons per energy n_{e} is given by Eq. 4.4.

4.2.2 Synchrotron radiation

The magnetic field strengths of dwarf spheroidals, that is, such sources which are suitable for DM search, are hardly known. However, one can assume that the magnetic field of the MW prevails at the location of its satellites and that it decreases with distance cubed. This provides a lower limit on the magnetic field strength at a location in the Galactic halo. The magnetic field strength in the local neighbourhood is about $6\,\mu$G (Beck 2011). Thus, the magnetic field B at distance d and its energy density can be estimated by

$$B(d) = 6\,\mu\mathrm{G}\left(\frac{8\,\mathrm{kpc}}{d}\right)^3 \quad \text{and} \quad U_{\mathrm{B}} = \frac{B^2}{2\mu_0}\,. \tag{4.13}$$

For distant satellites, an intergalactic magnetic field strength of $1\,n$G (Dolag et al. 1999) is used as an absolute lower boundary for B.

Again, the `Naima` package is used to calculate the spectrum. It uses the function $\tilde{G}(x)$ (see Eq. D7 of Aharonian et al. 2010) to approximate the synchrotron emissivity averaged over the directions of magnetic field B:

$$\left(\frac{dN}{d\omega\, dt}\right)_{\mathrm{Syn}} = \frac{\sqrt{3}}{2\pi} \frac{e^3 B}{E_0 \hbar\omega} \tilde{G}\left(\frac{\omega}{E_{\mathrm{c}}}\right), \text{ where } E_{\mathrm{c}} = \frac{3e\hbar c B}{2E_0}\left(\frac{E}{E_0}\right)^2. \tag{4.14}$$

The differential spectrum is then again given by Eq. 4.12.

4.2.3 Bremsstrahlung

As the gas densities of dwarf galaxies are also hardly known, the particle density of the MW halo scaled with distance is used to estimate the amount of gas in the MW satellites. The best-fit spherical model according to Miller & Bregman (2013) yields, for large radii, an electron density of

$$n_0(d) = 0.46\,\mathrm{cm}^{-3}\left(\frac{d}{0.35\,\mathrm{kpc}}\right)^{-2.13}. \tag{4.15}$$

`Naima` uses the approximations for the cross-section $\sigma_{\text{e-e}}(E)$ of electron-electron bremsstrahlung, which are given by Baring et al. (1999) in Eqs. A1 and A5 for the relativistic ($E > 2\,\mathrm{MeV}$) and non-relativistic case. The differential bremsstrahlung spectrum is then given by

$$\left(\frac{d\Phi}{d\omega}\right)_{\text{e-e}} = \frac{cn_0}{4\pi d^2}\int_{E_{\min}}^{E_{\max}} 2n_{\text{e}}(E)\times\sigma_{\text{e-e}}(E)\,dE\,. \tag{4.16}$$

4.3 Neutrino Emission

In addition to primary and secondary radiation, the neutrino emission can be calculated using the prompt emission, Eq. 4.1, with the neutrino spectra from Fig. 4.1. However, the background, for example, from atmospheric neutrinos is expected to be much larger than the neutrino flux from DM. A total neutrino spectrum at Earth is given in Vitagliano et al. (2020) and shown in Fig. 4.6.

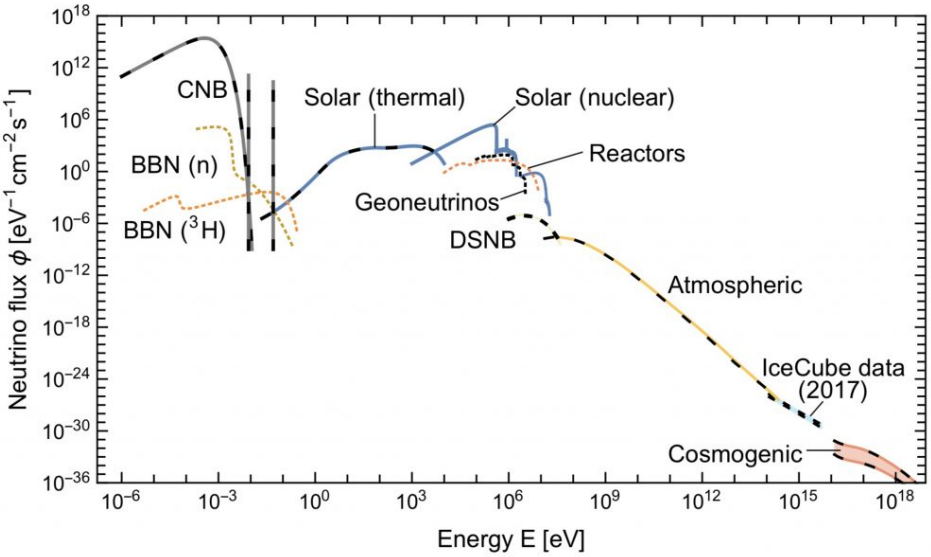

Figure 4.6: Grand Unified Neutrino Spectrum at Earth. In the GeV to TeV range, the spectrum is dominated by atmospheric neutrinos, while in the MeV regime there are contributions from solar neutrinos, geoneutrinos, reactor neutrinos and from the DSNB. Figure from Vitagliano et al. (2020).

In the GeV to TeV range, the spectrum is dominated by atmospheric neutrinos, while in the MeV regime there are contributions from solar neutrinos, geoneutrinos, reactor neutrinos and from the diffuse supernova neutrino background (DSNB). Solar neutrinos emerge from nuclear reactions through the *pp* chains and the CNO cycle. Thereby, electron neutrinos at MeV energies originate from β^+-decay of the effective form $p \to n + e^+ + \nu_e$. Geoneutrinos are produced by the decay of long-lived natural radioactive isotopes in the Earth, such as ^{238}U, ^{232}Th and ^{40}K. In this case, electron antineutrinos originate from β^--decay: $n \to p + e^- + \bar{\nu}_e$. Electron antineutrinos are also generated by the decay of fission products in nuclear power plants. The contribution of diffuse flux from reactor neutrinos is of the same order than from solar and geoneutrinos (see Fig. 4.6). A smaller contribution comes from the DSNB. Supernova neutrinos originate from collapsing stars in the visible Universe. During the core collapse of a massive star, its gravitational binding energy is released in the form of neutrinos. At higher energies, neutrinos emerge from CR interactions in the atmosphere. Cosmic rays, which are highly energetic and charged particles like electrons, protons and heavier nuclei, cause particle showers when they scatter in the atmosphere. Among the resulting secondary particles are charged pions and kaons, which finally decay also into neutrinos (for $\pi^\pm$-decay see Fig. 2.16).

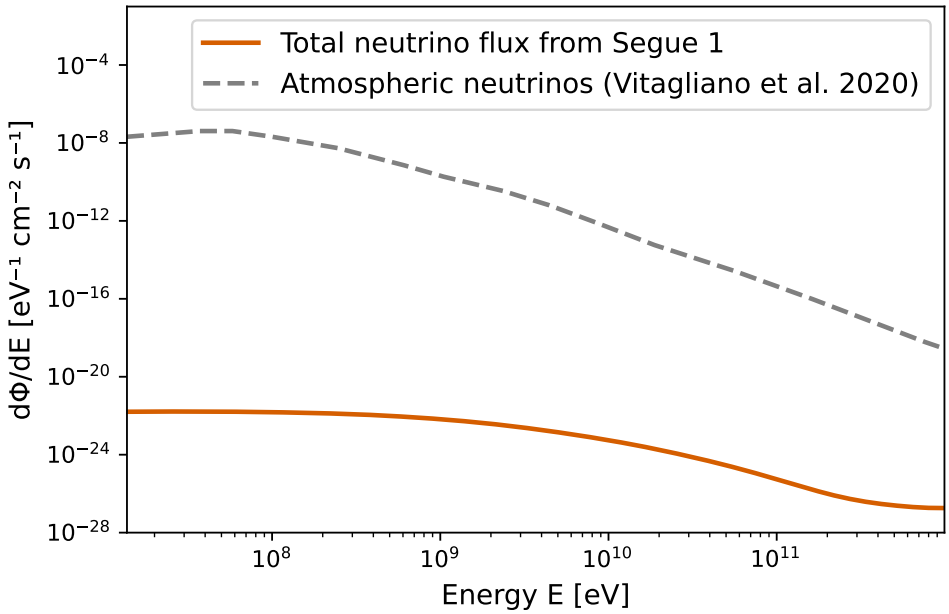

Figure 4.7: Total neutrino spectrum as expected from the scotogenic DM model for the dwarf galaxy Segue 1 compared to the atmospheric neutrino background integrated over directions.

Considering the prompt neutrino emission from Fig. 4.1, a possible contribution from DM to the neutrino background can be estimated for individual galaxies. Since the neutrino flux is even higher at (sub)-MeV energies, the focus of the comparison is on atmospheric neutrinos ranging from about 10 MeV to 1 TeV. Because the oscillation of

neutrinos will change the fractions of *measured* neutrinos at Earth, it will be summed over the different flavors. The prompt emission is converted into a flux according to Eq. 4.1 for the scotogenic DM model. As an example galaxy Segue 1 is chosen, which has the largest J-factor of the sample of dwarf spheroidals considered in Chapter 5. The total neutrino spectrum for Segue 1 compared to the atmospheric neutrino background is shown in Fig. 4.7. It should be noted that the background is integrated over directions. The signal-to-background ratio is largest at 1 TeV but still only of the order of 10^{-7} if the background flux is divided by 4π. To estimate the entire Cosmic Neutrino Background from this model, DM halos from all known galaxies including the MW would need to be taken into account, which would still be several orders of magnitude below the atmospheric neutrino flux. With photon measurements, the chance of finding a DM signal is higher, especially when a multiwavelength spectrum including primary and secondary emission from DM annihilation is considered.

4.4 Dark Matter Spectral Energy Distribution

The major goal of this study is to create Spectral Energy Distributions (SEDs) for different dwarf galaxies regarding their expectations from scotogenic WIMP DM. For this purpose, a parametrized SED model is developed, which calculates both the primary and secondary emission depending on characteristic parameters of a galaxy. In general, the IC, synchrotron and bremsstrahlung emission depend on the temperature T and radiation density of the photon field U_{rad}, the magnetic field B and the electron density n_0, respectively. For the special case of MW satellites galaxies, the quantities mentioned above are modeled (see Eqs. 4.8, 4.13, 4.15), so that the magnetic field and the electron density only depend on the distance d of the galaxy to the Sun and U_{rad} of the SL photon field is a function of the visual magnitude M_{V} of the galaxy and its half-light radius r. T_{SL} is set to 5000 K as an estimate of the average temperature of dwarf galaxies.
From the input parameters J, d, r and M_{V} and their uncertainties, the DM model spectrum for dwarf galaxies includes five SED components. These are the prompt photons, the CMB and SL IC emission, bremsstrahlung and synchrotron radiation. The corresponding differential fluxes are calculated according to Eqs. 4.1, 4.12 and 4.16, respectively, and then converted to energy fluxes by multiplying with E^2. From the uncertainties of the input parameters, a maximum uncertainty band is shown for each component. An example SED for the parameters of the dwarf galaxy Draco is given in Fig. 4.8. It can be seen that the peak emission of the IC contribution from the CMB is about $10^{-16}\,\mathrm{erg\,cm^{-2}\,s^{-1}}$ at 2 MeV, which is almost on the order of the prompt emission of $6 \times 10^{-16}\,\mathrm{erg\,cm^{-2}\,s^{-1}}$ at 50 GeV. The total fluxes of the CMB IC and prompt components integrated over all energies are $1 \times 10^{-15}\,\mathrm{erg\,cm^{-2}\,s^{-1}}$ and $2 \times 10^{-15}\,\mathrm{erg\,cm^{-2}\,s^{-1}}$, respectively. The dependence of each SED component from the model parameters is discussed below.

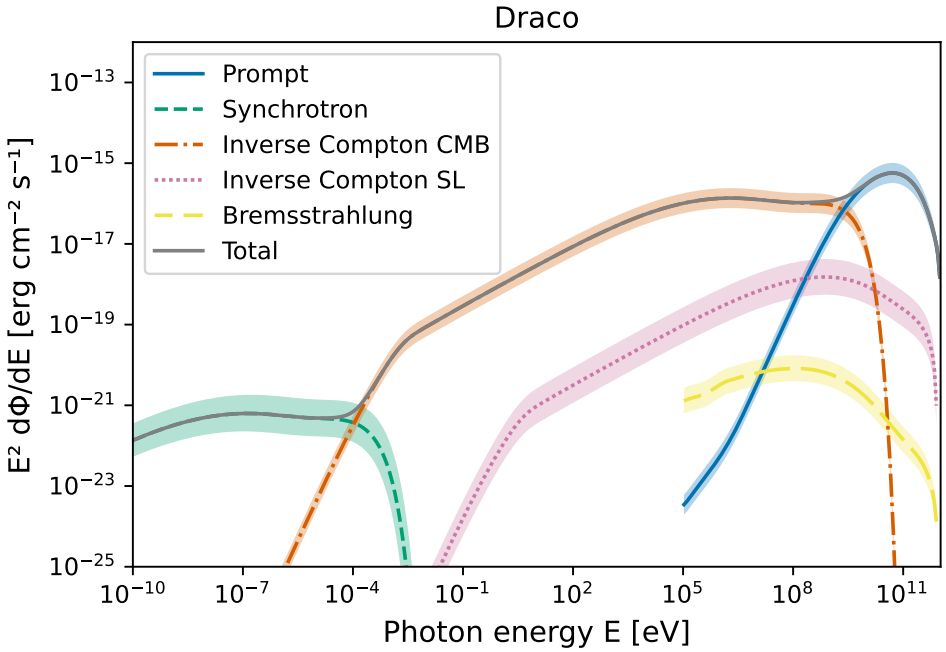

Figure 4.8: Multiwavelength DM spectrum. Shown are the expectations from the direction of the Draco dwarf galaxy of prompt emission of DM co-annihilation, and the secondary emission of electrons and positrons from the DM annihilation undergoing IC scattering off the CMB and stellar light (SL), bremsstrahlung, and synchrotron radiation. The colored bands indicate the uncertainties from taking into account the minimum and maximum values of magnetic fields, densities, etc., from modeling the individual components.

Referring to Eq. 4.1, the primary emission depends only on the J-factor of the respective galaxy since the particle physics parameters of the scotogenic DM candidate are fixed. The total prompt flux, integrated over all energies, scales with the J-factor according to: $2 \times 10^{-14}\,(J/10^{20}\,\mathrm{GeV^2\,cm^{-5}})\,\mathrm{erg\,cm^{-2}\,s^{-1}}$. Fig. 4.9a shows the primary spectrum for different J-factors having the same shape as the annihilation spectrum in Fig. 4.1 with a peak around 50 GeV.

As calculated in Sec. 4.2, all spectral components of the scotogenic DM model depend linearly on J, which means that the total SED scales with J. At the same, due to the unknown DM distribution in galaxies the J-factor typically has a large uncertainty which makes up a major part of the uncertainty band of the total SED model.
The IC spectra do effectively not depend on the distance since d^2 cancels in Eqs. 4.5 and 4.12. A small dependence on d comes from the energy loss rate $b(E)$ of the electrons (see Eqs. 4.6, 4.7) since synchrotron and bremsstrahlung losses depend on magnetic field $B(d)$ and gas density $n_0(d)$. However, it can be seen from Fig. 4.10 that the loss rate from IC scattering with the CMB dominates $b(E)$ almost over all energies even for small distances such as $d = 20\,\mathrm{kpc}$. The loss rate from IC scattering with SL strongly depends on the magnitude M_V and size r of the source and can also be higher than $b_\mathrm{CMB}(E)$. Note that at smaller energies, $E \lesssim 1\,\mathrm{MeV}$, also ionization and other Coulomb losses will add to the

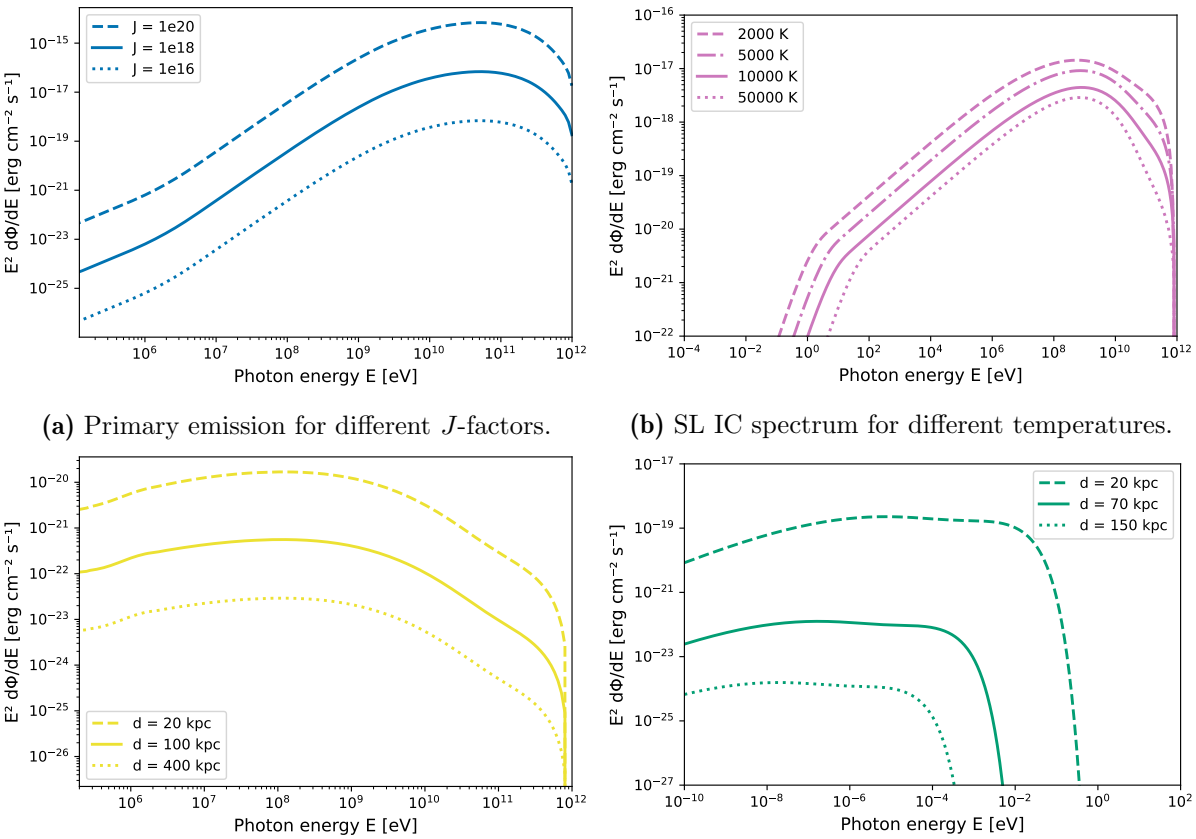

(a) Primary emission for different J-factors.

(b) SL IC spectrum for different temperatures.

(c) Bremsstrahlung for different distances d.

(d) Synchrotron spectrum for different distances d.

Figure 4.9: Dependence of different SED components on the model parameters. The respective remaining parameters from (a) to (d) are set to $J = 10^{18}\,\mathrm{GeV^2\,cm^{-5}}$, $d = 100\,\mathrm{kpc}$, $M_\mathrm{V} = -6$ and $r = 200\,\mathrm{pc}$.

cooling function. Since the gas properties in dwarf galaxies are highly uncertain, these losses are omitted for further discussion of the secondary emission. In fact, they become important for tertiary emission (see Ch. 7).

Consequently, the CMB IC component effectively also only depends on J. Note that the J-factor itself depends intrinsically on the distance d of the source due to the line-of-sight integral. The amplitude of the SL IC spectrum additionally scales with r^{-2} and $10^{-0.4M_\mathrm{V}}$ which can be interpreted as follows: The brighter the galaxy is in the visual band, the larger is the radiation density U_rad of its starlight. For a fixed magnitude M_V, the density of stars and thus U_rad decreases with the size r of the galaxy. In general, there is one more parameter: the temperature T_SL of the SL photon field, which also determines the scaling factor f_V of U_rad. Fig. 4.9b shows the IC component for different temperatures as calculated from U_rad including a scaling factor dependent on temperature. In this case, U_rad scales with f_V which can be determined by integrating the Planck spectrum. It can be seen in Fig. 4.5 that the V-band flux increases up to 10000 K until the peak of the blackbody spectrum is shifted towards higher energies exceeding the visual range. Calculating the scaling factors for 2000 K, 5000 K, 10000 K and 50000 K yields 70000, 200,

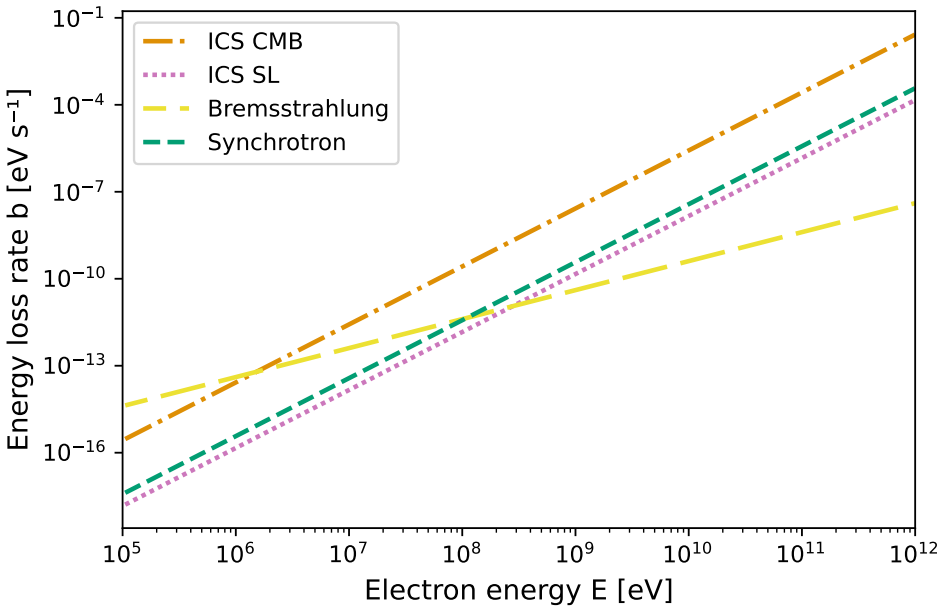

Figure 4.10: Contributions to the total energy loss rate of electrons produced by DM annihilation (see Eqs. 4.6, 4.7). The loss rates are plotted for $d = 20\,\mathrm{kpc}$, $M_\mathrm{V} = -6$ and $r = 100\,\mathrm{pc}$.

40 and 50, respectively. Assuming a fixed magnitude M_V and radius r, the SL radiation density U_rad must be much larger for a colder star population to reach the same visual flux which is reflected by the increasing scaling factor f_V. The IC spectra in Fig. 4.9b scale with U_rad and therefore with f_V but also with T^{-2} (see Eq. 4.10) considering the dilution factor κ (see Eq. 4.11). Besides, they are proportional to the electron distribution including energy losses (see Eq. 4.4). In the case of $T = 2000\,\mathrm{K}$, U_rad is much larger than U_CMB so that all other energy losses can be neglected which means that the spectrum effectively only scales with T^{-2} as f_V cancels. For the other temperatures, the energy loss through IC scattering of SL photons is equal to or smaller than through CMB scattering, which makes the spectrum dependent on f_V to some extent.

In general, the average temperature of the star population in dwarf galaxies is unknown which is why a conservative approach is used and T_SL estimated to be about 5000 K while setting f_V to 1. In any case, assuming a blackbody spectrum of an average temperature is just an approximation. It would be needed to measure the true spectrum of a galaxy, which is the cumulative spectrum of many stars with different temperatures. Even if the SL IC emission was enhanced by a scaling factor of the order of 100, it would not exceed the CMB and prompt component in the case of Draco (see Fig. 4.8). It should be kept in mind that in some cases the peak of the SL component could show up around 1 GeV between the peak of the CMB component at 1 MeV and the prompt emission peak at 50 GeV. The peak energy of the IC spectrum depends only weakly on the temperature of the SL photon field (see Fig. 4.9b) since the underlying electron distribution is always the same which means that the electrons have a limited amount of energy to upscatter

photons.

Besides a dependence on J and slightly on M_{V} and r due to $b(E)$, the bremsstrahlung and synchrotron spectra are mainly subject to the distance d. The bremsstrahlung amplitude decreases with declining electron gas density $n_0(d)$ as $d^{-2.13}$. The synchrotron spectrum is a complex function of magnetic field and thus of the distance d. Figs. 4.9c and 4.9d show the bremsstrahlung and synchrotron SED according to the model for different distances. Note that for distances of $d \approx 145\,\mathrm{kpc}$ and larger, the synchrotron component remains constant since a lower boundary for the magnetic field of $B = 1\,\mathrm{nG}$ is assumed, which results in a minimum peak flux of about $10^{-24}\,\mathrm{erg\,cm^{-2}\,s^{-1}}$.
In the next chapter, the parametrized DM model will be applied to a sample of selected dwarf galaxies.

5 Application to Dwarf Galaxies

5.1 Sample of Dwarf Galaxies

Dwarf galaxies typically have large mass-to-light ratios up to the order of 1000 (Strigari et al. 2008), which means that they are the most DM dominated objects in the Universe. Apart from that, the fact that the faint satellites of the MW are relatively close and have a very low intrinsic emission makes them promising targets for the indirect DM search. In order to determine a DM annihilation signal from a galaxy, it is crucial to estimate its DM density distribution and therefore its J-factor. In particular, dwarf spheroidal galaxies (dSphs) are very faint objects having a spheroidal shape and possibly a cusped DM density profile. Evans et al. (2016) analytically determined the J-factors for 27 dSphs by assuming spherical NFW profiles (see Eq. 2.2). The parameter ρ_s can be determined from the mass enclosed within the half-light radius r, which can be constrained from the luminosity weighted square of the velocity dispersion of stars.

Tab. 5.1 summarizes important properties of the 27 selected dwarf galaxies, which are needed for the DM analysis in this work. The J-factors are given for a scaling radius of $r_s = 5r$ and an integration angle between the center and the outermost star of the dwarf. While the subhalo boost factor may range between 1 and 5 for dwarf galaxies (see Sec. 2.3.3), the assumption throughout this chapter is that the boost factor for each galaxy is equal to 1.

5.2 Expectations in Dwarf Galaxies

For each dSph the expected fluxes from DM annihilation are calculated as described in the previous chapter from the parameters J, d, M_V, r given in Tab. 5.1, also taking their uncertainties into account. Fig. 5.1 shows the modeled spectra for selected galaxies. It can be seen that the fluxes for the nearest dwarf, Segue 1, are expected to be at least a hundred times higher than for the respective galaxies with the largest distance, the smallest J-factor or the lowest total flux. Especially the synchrotron component is significantly larger for Segue 1 due to the influence of the magnetic field of the MW. Adding the fluxes of all dwarfs results in the total spectrum shown in Fig. 5.2.

Galaxy	$\log_{10}$J (GeV cm^{-5})	Distance (kpc)	Magnitude	Radius (pc)	RA (deg)	DEC (deg)
Carina	$18.03^{+0.34}_{-0.34}$	105 ± 6	-9.1 ± 0.5	$250.0^{+39.0}_{-39.0}$	100.40	-50.97
Draco	$18.92^{+0.25}_{-0.25}$	76 ± 6	-8.8 ± 0.3	$221.0^{+19.0}_{-19.0}$	260.05	57.92
Fornax	$18.27^{+0.17}_{-0.17}$	147 ± 12	-13.4 ± 0.3	$710.0^{+77.0}_{-77.0}$	40.00	-34.45
Leo I	$17.80^{+0.28}_{-0.28}$	254 ± 15	-12.0 ± 0.3	$251.0^{+27.0}_{-27.0}$	152.12	12.31
Leo II	$17.41^{+0.25}_{-0.25}$	233 ± 14	-9.8 ± 0.3	$176.0^{+42.0}_{-42.0}$	168.37	22.15
Sculptor	$18.73^{+0.29}_{-0.29}$	86 ± 6	-11.1 ± 0.5	$28.3^{+45.0}_{-45.0}$	15.04	-33.71
Sextans	$18.04^{+0.29}_{-0.29}$	86 ± 4	-9.3 ± 0.5	$695.0^{+44.0}_{-44.0}$	153.26	-1.61
Ursa Minor	$19.18^{+0.24}_{-0.24}$	76 ± 3	-8.8 ± 0.5	$181.0^{+27.0}_{-27.0}$	227.29	67.22
Boötes I	$16.64^{+0.64}_{-0.38}$	66 ± 2	-6.3 ± 0.2	$242.0^{+21.0}_{-21.0}$	210.03	14.50
Coma Berenices	$18.64^{+0.32}_{-0.32}$	44 ± 4	-4.1 ± 0.5	$77.0^{+10.0}_{-10.0}$	186.75	23.90
Canes Venatici I	$17.27^{+0.11}_{-0.11}$	218 ± 10	-8.6 ± 0.2	$564.0^{+36.0}_{-36.0}$	202.01	33.56
Canes Venatici II	$17.63^{+0.40}_{-0.40}$	160 ± 4	-4.9 ± 0.5	$74.0^{+14.0}_{-14.0}$	187.83	44.05
Hercules	$16.79^{+0.45}_{-0.45}$	133 ± 12	-6.6 ± 0.4	$330.0^{+75.0}_{-52.0}$	252.78	4.99
Leo IV	$16.56^{+0.90}_{-0.90}$	154 ± 6	-5.8 ± 0.4	$206.0^{+37.0}_{-37.0}$	173.24	-0.53
Leo V	$16.82^{+1.05}_{-0.70}$	178 ± 10	-5.2 ± 0.4	$135.0^{+32.0}_{-32.0}$	172.79	2.22
Leo T	$17.28^{+0.37}_{-0.37}$	417 ± 19	-8.0 ± 0.5	$120.0^{+9.0}_{-9.0}$	143.72	17.05
Segue 1	$19.39^{+0.39}_{-0.39}$	23 ± 2	-1.5 ± 0.8	$29.0^{+8.0}_{-5.0}$	151.77	16.08
Segue 2	$17.06^{+0.86}_{-1.75}$	35 ± 2	-2.5 ± 0.3	$35.0^{+3.0}_{-3.0}$	34.82	20.18
Ursa Major I	$18.47^{+0.25}_{-0.25}$	97 ± 4	-5.5 ± 0.3	$319.0^{+50.0}_{-50.0}$	158.72	51.92
Ursa Major II	$19.38^{+0.39}_{-0.39}$	32 ± 4	-4.2 ± 0.6	$149.0^{+21.0}_{-21.0}$	132.88	63.13
Willman 1	$19.29^{+0.91}_{-0.62}$	38 ± 7	-2.7 ± 0.8	$25.0^{+6.0}_{-6.0}$	162.34	51.05
Reticulum II	$18.72^{+0.85}_{-0.32}$	30 ± 3	-2.7 ± 0.1	$32.0^{+1.9}_{-1.1}$	53.93	-54.05
Tucana II	$19.10^{+0.88}_{-0.58}$	57 ± 5	-3.8 ± 0.1	$165.0^{+27.8}_{-18.5}$	342.98	-58.57
Horologium I	$18.64^{+0.95}_{-0.39}$	79 ± 7	-3.4 ± 0.1	$30.0^{+4.4}_{-3.3}$	43.88	-54.12
Hydra II	$16.56^{+0.87}_{-1.85}$	134 ± 10	-4.8 ± 0.3	$68.0^{+11.0}_{-11.0}$	185.43	-31.99
Pisces II	$17.90^{+1.14}_{-0.80}$	182 ± 18	-5.0 ± 0.0	$58.0^{+99.0}_{-99.0}$	344.63	5.95
Grus I	$17.96^{+0.90}_{-1.93}$	120 ± 11	-3.4 ± 0.3	$62.0^{+29.8}_{-13.6}$	344.18	-50.16

Table 5.1: List of selected dSphs in this study. J-factors are given for a NFW profile with $r_s = 5r$ and for an integration angle between the centre and the outermost star of the dwarf. For J-factors and distances d see Evans et al. (2016). Absolute visual magnitudes M_V and half-light radii r are taken from McConnachie (2012), Koposov et al. (2015) and Martin et al. (2015).

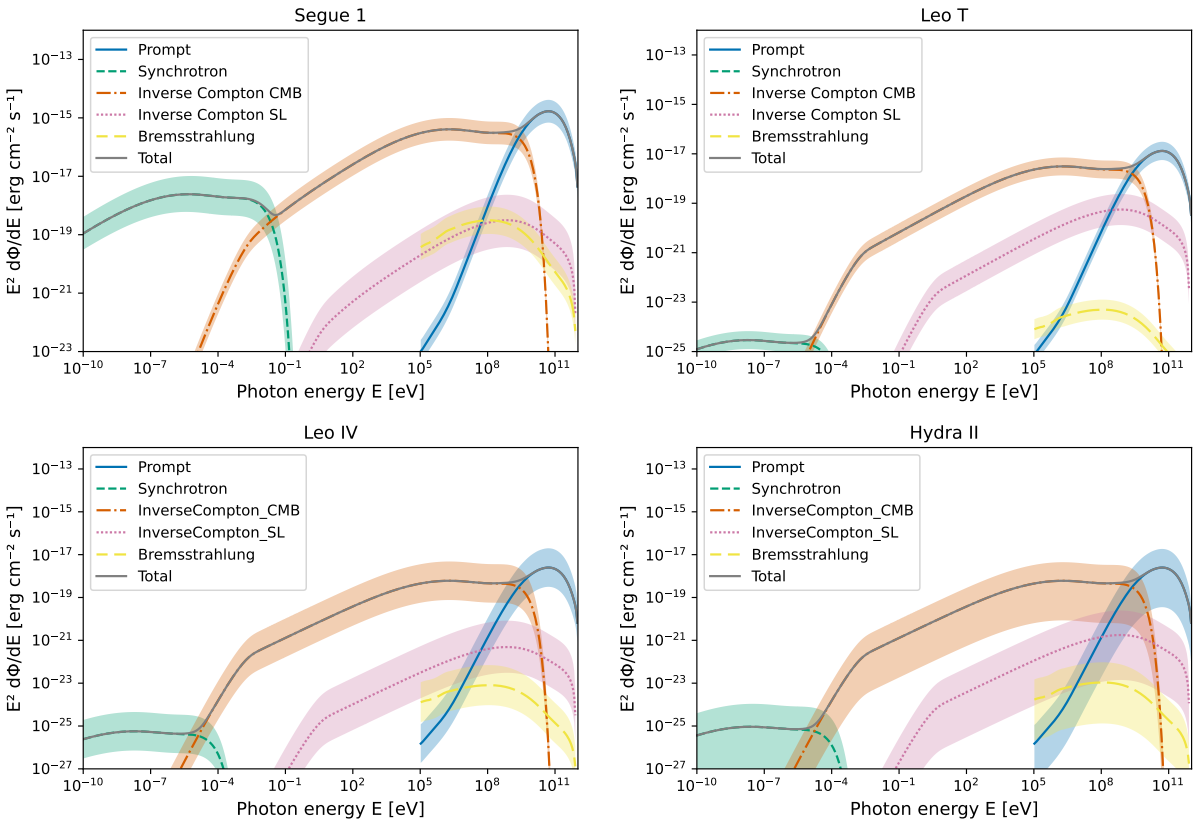

Figure 5.1: Same as Fig. 4.8 but for selected dwarf spheroidals. **Upper left:** smallest distance / largest J-factor / largest total flux (Segue I). **Upper right:** Largest distance (Leo T). **Lower left:** Smallest J-factor (Leo IV). **Lower right:** Smallest total flux (Hydra II).

Relating the predictions from the scotogenic DM model to an observational framework, the calculated fluxes are integrated over relevant instrument energy bands in the X-ray to the high-energy gamma-ray range. The results are summarised in Tab. 5.2, where the respective energy flux F_{E} was determined by a weighted integration of the differential flux $d\Phi/dE$:

$$F_{\mathrm{E}} = \int_{E_{\mathrm{min}}}^{E_{\mathrm{max}}} E \frac{d\Phi}{dE} dE \,, \tag{5.1}$$

where the integration limits correspond to the energy coverage of the respective instrument. In particular, integrated fluxes are calculated in the bands according to the sensitive range for INTEGRAL/ISGRI and JEM-X (1–30 keV, Winkler et al. 2003), Swift/BAT (14–195 keV, Barthelmy et al. 2005), INTEGRAL/SPI (0.1–1.0 MeV, Vedrenne et al. 2003), CGRO/COMPTEL (1–30 MeV, Schönfelder et al. 1992), and Fermi/LAT (30–100 MeV and 0.1–100 GeV, Atwood et al. 2009), respectively. The chosen instruments present the currently best available set of observatories from X- to gamma-rays and are introduced below. However, the calculated flux values do not depend on the choice of the instrument.

On board of the International Gamma-Ray Astrophysics Laboratory (INTEGRAL,

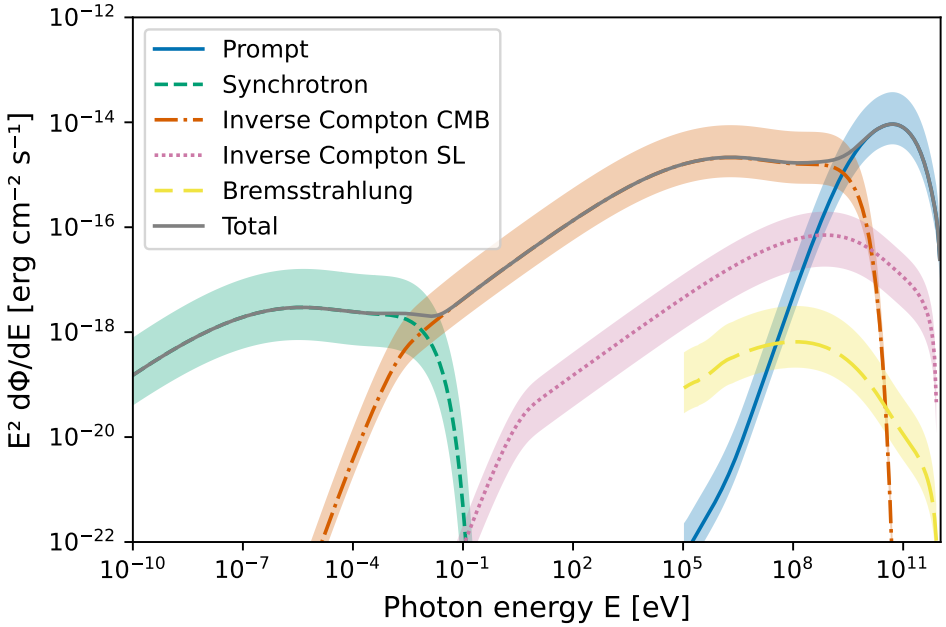

Figure 5.2: Same as Fig. 4.8 but for the cumulative signal of all 27 selected dwarf galaxies.

Winkler et al. 2003) satellite launched in 2002 are the telescopes ISGRI (INTEGRAL Soft Gamma-Ray Imager) and JEM-X (Joint European X-ray Monitor) as well as the spectrometer SPI (Vedrenne et al. 2003). JEM-X plays an important role in the detection of gamma-ray sources, while ISGRI is the low-energy camera of IBIS (Imager on Board the Integral Satellite).

The Burst Alert Telescope (BAT, Barthelmy et al. 2005) of the Swift satellite launched in 2004 has a large field-of-view and is designed to detect gamma-ray bursts.

One instrument of the Compton Gamma-Ray Observatory (CGRO) operating from 1991 to 1999 was the Imaging Compton Telescope (COMPTEL, Schönfelder et al. 1992) which has surveyed the sky at MeV energies.

The Large Area Telescope (LAT, Atwood et al. 2009) of the Fermi Gamma-ray Space Telescope operates since 2008 to perform long term and high sensitivity observations up to hundreds of GeV.

Fig. 5.3 shows the continuum sensitivity curves of the instruments above. In comparison with the integrated fluxes in Tab. 5.2, it can be seen that the expected fluxes from the scotogenic DM model are at least three orders of magnitude below the sensitivity of current instruments gauged for observation times of 1 Ms. Especially in the MeV range, there is a lack of highly sensitive observatories (Siegert et al. 2022). However, the sensitivity between 0.2 and 5 MeV will be enhanced immensely with the launch of the Compton Spectrometer and Imager (COSI; Tomsick et al. 2019, 2023) in 2027, which will favor the detection of the IC emission peak in the MeV band (see Fig. 5.1 and 5.2).

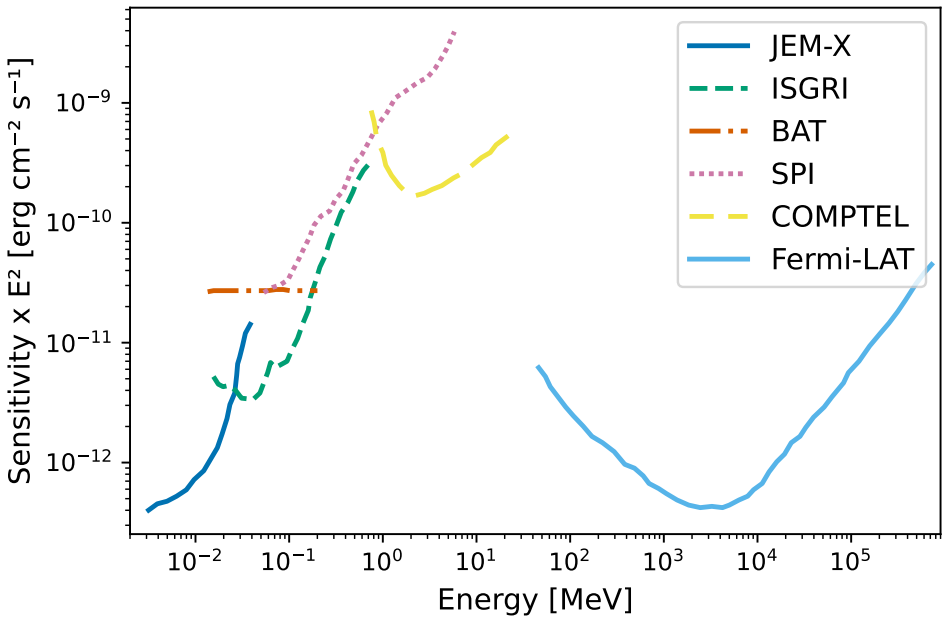

Figure 5.3: Continuum sensitivity (3σ) of X- and gamma-ray instruments for an observation time of 1 Ms.

Even if such faint signals might be detectable in the future, signatures from DM have to be disentangled from large astrophysical fore- and backgrounds. In the next chapter, different background emission components will be discussed in order to estimate signal-to-background ratios for the selected dwarf galaxies.

Galaxy	JEM-X|ISGRI 1 keV-30 keV	Swift/BAT 14 keV-195 keV	SPI 100 keV-1 MeV	COMPTEL 1 MeV-30 MeV	Fermi/LAT 30 MeV-100 MeV	Fermi/LAT 100 MeV-100 GeV	Total 1 keV-100 GeV
Carina	2.05e-17	2.85e-17	3.35e-17	5.60e-17	1.52e-17	2.25e-16	4.38e-16
Draco	1.59e-16	2.22e-16	2.60e-16	4.35e-16	1.18e-16	1.75e-15	3.40e-15
Fornax	3.30e-17	4.60e-17	5.42e-17	9.21e-17	2.57e-17	3.94e-16	7.48e-16
Leo I	1.01e-17	1.42e-17	1.68e-17	2.91e-17	8.45e-18	1.35e-16	2.48e-16
Leo II	4.72e-18	6.58e-18	7.74e-18	1.30e-17	3.59e-18	5.42e-17	1.04e-16
Sculptor	1.57e-17	2.44e-17	3.42e-17	1.05e-16	5.44e-17	1.21e-15	1.77e-15
Sextans	2.12e-17	2.95e-17	3.47e-17	5.79e-17	1.56e-17	2.30e-16	4.49e-16
Ursa Minor	2.87e-16	4.00e-16	4.71e-16	7.88e-16	2.14e-16	3.18e-15	6.17e-15
Boötes I	8.46e-19	1.18e-18	1.38e-18	2.30e-18	6.21e-19	9.17e-18	1.79e-17
Coma Berenices	8.45e-17	1.18e-16	1.38e-16	2.30e-16	6.20e-17	9.17e-16	1.79e-15
Canes Venatici I	3.61e-18	5.02e-18	5.90e-18	9.83e-18	2.65e-18	3.91e-17	7.63e-17
Canes Venatici II	8.25e-18	1.15e-17	1.35e-17	2.25e-17	6.06e-18	8.96e-17	1.75e-16
Hercules	1.20e-18	1.66e-18	1.95e-18	3.26e-18	8.77e-19	1.30e-17	2.53e-17
Leo IV	7.04e-19	9.80e-19	1.15e-18	1.92e-18	5.16e-19	7.63e-18	1.49e-17
Leo V	1.28e-18	1.78e-18	2.09e-18	3.49e-18	9.39e-19	1.39e-17	2.71e-17
Leo T	3.61e-18	5.03e-18	5.91e-18	9.90e-18	2.69e-18	4.01e-17	7.77e-17
Segue 1	4.72e-16	6.58e-16	7.73e-16	1.29e-15	3.47e-16	5.15e-15	1.01e-14
Segue 2	2.22e-18	3.09e-18	3.63e-18	6.06e-18	1.63e-18	2.41e-17	4.70e-17
Ursa Major I	5.72e-17	7.97e-17	9.36e-17	1.56e-16	4.20e-17	6.20e-16	1.21e-15
Ursa Major II	4.65e-16	6.47e-16	7.60e-16	1.27e-15	3.41e-16	5.04e-15	9.83e-15
Willman 1	3.76e-16	5.24e-16	6.16e-16	1.03e-15	2.77e-16	4.10e-15	7.98e-15
Reticulum II	1.01e-16	1.41e-16	1.66e-16	2.77e-16	7.45e-17	1.10e-15	2.15e-15
Tucana II	2.44e-16	3.40e-16	3.99e-16	6.65e-16	1.79e-16	2.64e-15	5.16e-15
Horologium I	8.42e-17	1.17e-16	1.38e-16	2.30e-16	6.20e-17	9.17e-16	1.79e-15
Hydra II	7.02e-19	9.77e-19	1.15e-18	1.91e-18	5.16e-19	7.63e-18	1.49e-17
Pisces II	1.53e-17	2.13e-17	2.50e-17	4.18e-17	1.13e-17	1.67e-16	3.25e-16
Grus I	1.77e-17	2.46e-17	2.89e-17	4.82e-17	1.30e-17	1.92e-16	3.74e-16
Total	2.49e-15	3.47e-15	4.09e-15	6.87e-15	1.88e-15	2.83e-14	5.45e-14

Table 5.2: Expected fluxes from the scotogenic WIMP DM model including prompt emission from DM annihilation and secondary emission from IC scattering, bremsstrahlung, and synchrotron radiation, integrated over different energy bands. All values are calculated according to Eq. (5.1) and given in units of $\mathrm{erg\,cm^{-2}\,s^{-1}}$.

6 Astrophysical Fore- and Background

In the following, the diffuse emission component of the MW itself is estimated, including its own DM halo from the same scotogenic DM model. For the calculation of the diffuse MW foreground, GALPROP v57 (Porter et al. 2022), a numerical code for CR transport and resulting photon emission, is used. An NFW halo is assumed for estimating the prompt emission from DM in the MW. In addition, it is searched for X- and γ-ray sources in small angular separation from the galaxies in the selected sample which would lead to a contamination of the DM signal. To obtain a signal-to-background ratio in different bands for each galaxy, all mentioned contributions are integrated in the selected regions of interest.

6.1 Diffuse Galactic Emission

Nonthermal diffuse emission is induced by cosmic rays (CRs), such as electrons, positrons, protons and light nuclei, via different mechanisms. On the one hand, gamma-rays from π^0-decay and bremsstrahlung are produced when highly energetic charged particles interact with gas of the ISM. On the other hand, CRs IC scatter off the ISRF (see Fig. 4.2) contributing to the gamma-ray emission. Furthermore, synchrotron radiation in the radio regime is produced by CRs interacting with the Galactic magnetic field (GMF). Another component of the diffuse galactic background in the radio wavelength range is free-free emission, which is in the astrophysical context usually equal to thermal bremsstrahlung generated by the thermal motion of free electrons in a hot and dense plasma.

The GALPROP framework is used as a standard for the modeling of the diffuse photon emissions in the MW from radio to gamma-rays. The idea of GALPROP is to implement real data from astrophysics and particle physics to provide realistic and self-consistent models. For this analysis, simulated gamma-ray and synchrotron intensity sky maps, which are obtained from the line-of-sight integration of the different emissivity components, are created. To calculate the emissivities, GALPROP uses the propagated CR distributions including secondary particles.

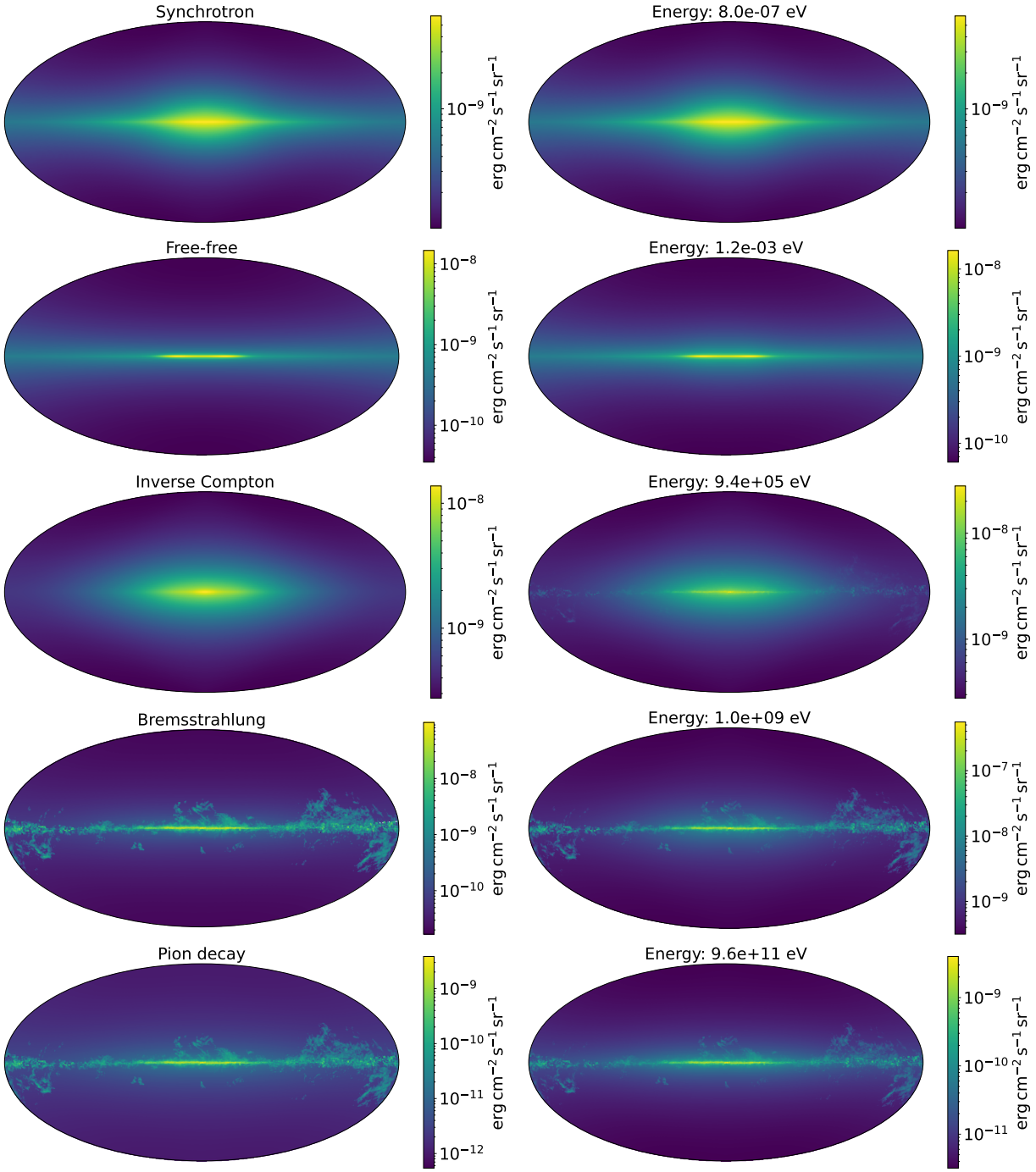

Figure 6.1: GALPROP (v57) simulations at around 1 μeV, 1 meV, 1 MeV, 1 GeV and 1 TeV. The left column shows the contributions of individual components, while the right column includes all fluxes. The photon energy is the same in each row.

The propagation of a particle species is described by the following Fokker-Planck-like equation (Strong et al. 2007),

$$\frac{\partial \psi}{\partial t} = S(\boldsymbol{r}, p) + \nabla \cdot (K \nabla \psi - \boldsymbol{V} \psi) + \frac{\partial}{\partial p}\left[p^2 K_p \frac{\partial}{\partial p}\frac{1}{p^2}\psi + \frac{p}{3}(\nabla \cdot \boldsymbol{V})\psi - \dot{p}\psi\right] - \frac{\psi}{\tau}\,, \quad (6.1)$$

where $\psi = \psi(\boldsymbol{r}, p, t)$ is the CR density per unit of total particle momentum p at position $\boldsymbol{r}$. The source term S takes primary and secondary CR production such as spallation and decay into account. The variables K and $\boldsymbol{V}$ are the diffusion coefficient and the convection velocity, respectively. The latter is determined by the gradient in the Galactic wind. The diffusion coefficient in momentum space K_p describes reacceleration and is related to K and the Alfvén wave speed V_A. The term with $\nabla \cdot \boldsymbol{V}$ considers adiabatic momentum change due to scattering of CRs by magnetic inhomogeneities. All forms of energy losses are represented by the momentum loss rate $\dot{p}$. The timescale τ includes particle losses by fragmentation of nuclei and radioactive decay. In summary, the free parameters of the GALPROP code are the diffusion coefficient K depending on particle momentum and charge, the Alfvén wave speed V_A and the convection velocity gradient dV/dz. Apart from that, the primary CR source term requires a definition of injection spectra, for example as broken power laws, and values of nuclear abundances. In this analysis, the input parameters are specified according to the latest GALPROP model by Bisschoff et al. (2019) which reproduces the observed CR spectra. It should be noted that the model underestimates the diffuse emission in the MeV band as Siegert et al. (2022a) have shown. The chosen spatial geometry for CR propagation in GALPROP is a cylindrical volume with azimuthal symmetry corresponding to a 2D model depending on radius and height above the Galactic plane. GALPROP version 57 (Porter et al. 2022) is used to calculate the diffuse emission from the specified model. Therefore, contributions from synchrotron and free-free emission, bremsstrahlung, pion decay and IC scattering are included. Fig. 6.1 shows examples of how the diffuse MW foreground appears as a function of photon energy and individual contributions to the total flux. It can clearly be seen that the bremsstrahlung and pion decay components reflect the structure of gas in the Galaxy, while the synchrotron, free-free and IC sky maps are characterized by a bright GC and disk creating diffuse emission. The scale and structure of the images in Fig. 6.1 suggest that at 1 μeV and 1 meV the total fluxes are dominated by synchrotron and free-free emission respectively. At 1 MeV, a strong IC component as well as faint structures of gas, indicating a small contribution from bremsstrahlung, become visible. Since neutral pions have a rest mass of about 135 MeV, photons from pion decay only become relevant at higher energies. Clear structures appear above 1 GeV where all high energy processes, such are IC scattering, bremsstrahlung and pion decay, contribute. At 1 TeV, the visible structure is dominated by CR induced pion production.

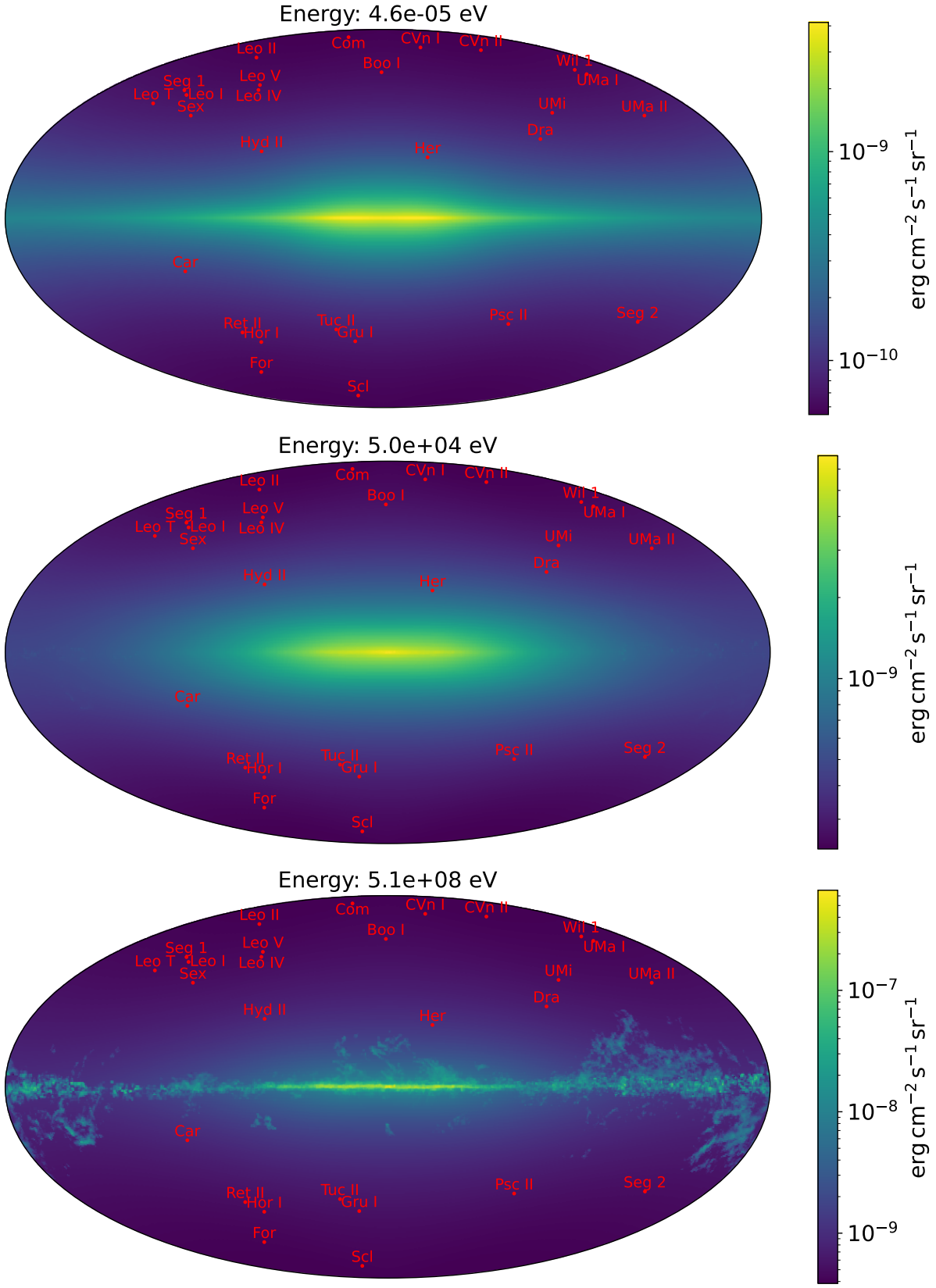

Figure 6.2: GALPROP (v57) simulations at around 50 μeV, 50 keV and 500 MeV. The upper plot includes synchrotron and free-free emission, while the middle and the lower one contain fluxes from bremsstrahlung, IC scattering and pion decay. The positions of the dSph sample are marked in red.

Fig. 6.2 shows the total MW foreground for another set of photon energies with positions of the dSphs indicated. The fact that the selected galaxies are located at higher latitudes makes them less affected by the presence of gas where bremsstrahlung and pion decay prevail. Instead, they are mostly exposed to a synchrotron and IC glow at low and high energies, respectively.

For a quantitative comparison of the different contributions, Fig. 6.3 shows the resulting spectra integrated over the total sky and over a circular region with a radius of 1° in the direction of the GC and Draco, respectively. Below 1 meV, synchrotron radiation is dominating over free-free emission for all regions. The diffuse foreground in the infrared and optical range stems from thermal dust emission, optical SL and ionized gas and is not included in GALPROP. Their expected fluxes are several orders of magnitude above the non-thermal emission considered here (see Fig. 4.2). In the soft gamma-ray regime from 1 keV to 1 MeV, the total diffuse emission is completely dominated by IC scattering ($> 99\%$) with only small contributions from bremsstrahlung. This can be seen for example in the middle panel of Fig. 6.2 where the missing structure from gas in the Galaxy is being outshined by the IC glow. After its peak around 0.2 GeV where it is equally bright compared to pion emission, the bremsstrahlung spectrum falls quickly. The pion decay spectrum rises steeply to its peak at 0.6 GeV where it takes over as strongest emission component in the GC up to 1 TeV. In the total sky, the flux levels of IC and pion decay are comparable from 0.5 GeV to 1 TeV. In the case of Draco, the presence of gas is minimal and only the IC component is significant up to ~ 1 GeV. Above, a $\sim 10\%$ fraction of the flux can also be expected from pion decay.

As a summary, Tab. 6.1 shows the diffuse Galactic emission fluxes integrated according to Eq. 5.1 across different bands as typically measured by the instruments introduced in Sec. 5.2. The integration angle corresponds to the respective resolution of the instrument in each band. It can be seen that the MW foreground as calculated by GALPROP is largest in the SPI and COMPTEL band. However, given the current measurements, the fluxes below ~ 100 keV are very uncertain because the strong contribution from unresolved point sources in hard X-rays (Krivonos et al. 2007) is neglected. Likewise, between 200 and 511 keV, the additional component of positron annihilation in the form of Positronium (Ps) decay (ortho-Ps continuum and para-Ps line) would enhance the diffuse emission in the Galactic bulge and disk (Siegert 2023; Siegert et al. 2016). In fact, the Ps decay makes the largest contribution in terms of foreground emission in the SPI band (0.1–1.0 MeV), amounting to $\sim 9 \times 10^{-9}\,\mathrm{erg\,cm^{-2}\,s^{-1}}$ for the full sky, and about $3 \times 10^{-10}\,\mathrm{erg\,cm^{-2}\,s^{-1}}$ towards the GC. At higher latitudes, for example in the direction of Draco, the Galactic Ps contribution is weak and estimated to be $4 \times 10^{-16}\,\mathrm{erg\,cm^{-2}\,s^{-1}}$ according to the model by Siegert et al. (2016). Based on Ackermann et al. (2012), the systematic uncertainty of the calculated GALPROP foreground is estimated to be about 30% on average since it strongly depends on Galactic latitude and energy.

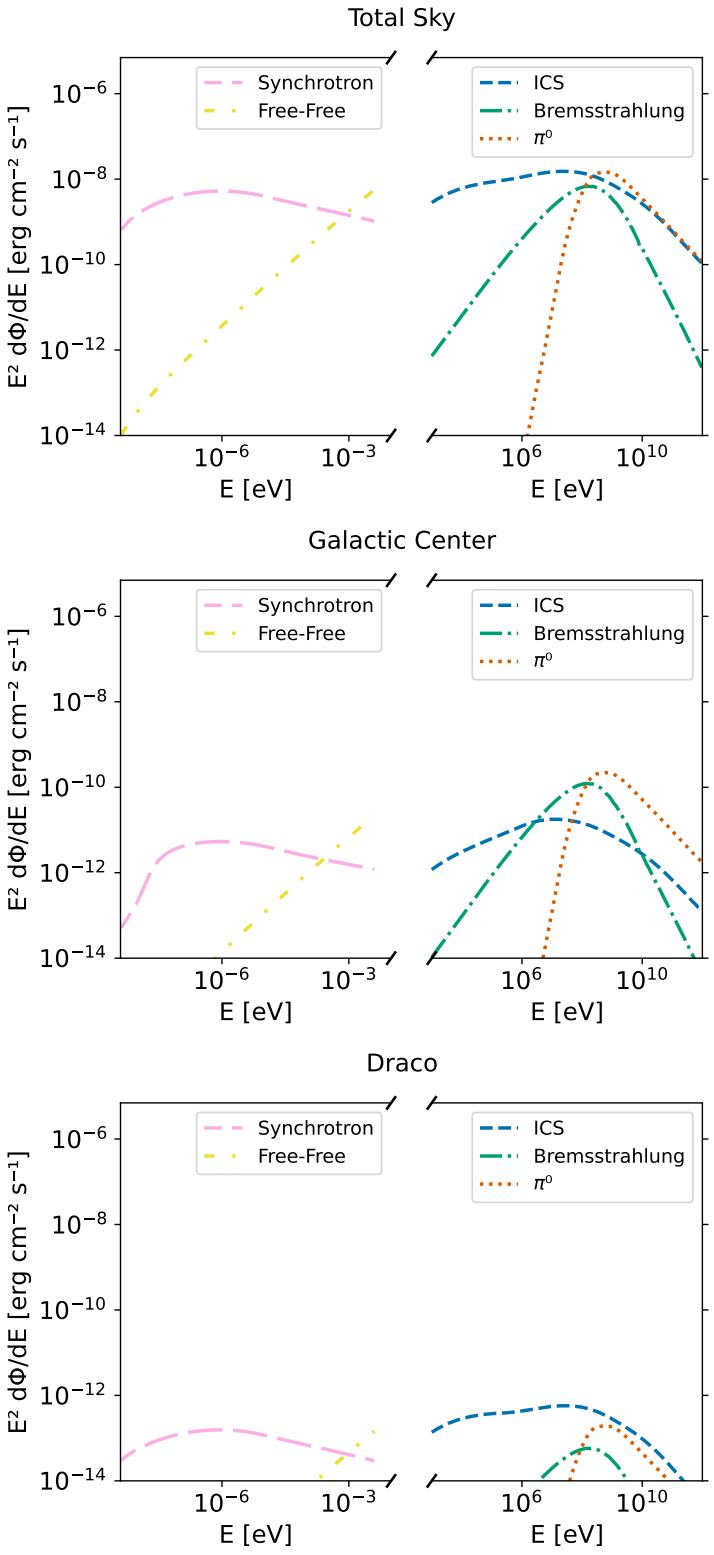

Figure 6.3: GALPROP (v57) spectral components of the total sky, towards the direction of the GC, and towards the direction of Draco. The latter two were calculated for an angular region of 1° each.

Galaxy	JEM-X|ISGRI 0.6° 1 keV-30 keV	Swift/BAT 1° 14 keV-195 keV	SPI 4° 100 keV-1 MeV	COMPTEL 3° 1 MeV-30 MeV	Fermi/LAT 3° 30 MeV-100 MeV	Fermi/LAT 1° 100 MeV-100 GeV	Total 1 keV-100 GeV
Carina	5.00e-13	1.17e-12	1.90e-11	1.97e-11	8.14e-12	2.93e-12	1.51e-10
Draco	3.51e-13	8.89e-13	1.54e-11	1.68e-11	6.89e-12	2.23e-12	1.22e-10
Fornax	1.80e-13	6.01e-13	9.37e-12	1.01e-11	4.14e-12	1.49e-12	7.43e-11
Leo I	1.90e-13	6.86e-13	1.03e-11	1.10e-11	4.53e-12	1.69e-12	8.12e-11
Leo II	1.96e-13	5.50e-13	9.02e-12	9.62e-12	3.94e-12	1.36e-12	7.14e-11
Sculptor	1.88e-13	5.84e-13	9.35e-12	1.03e-11	4.18e-12	1.47e-12	7.44e-11
Sextans	3.25e-13	7.01e-13	1.17e-11	1.23e-11	5.05e-12	1.73e-12	9.26e-11
Ursa Minor	3.13e-13	7.15e-13	1.18e-11	1.24e-11	5.10e-12	1.78e-12	9.34e-11
Boötes I	2.17e-13	6.75e-13	1.09e-11	1.23e-11	5.00e-12	1.72e-12	8.69e-11
Coma Berenices	1.78e-13	5.78e-13	9.11e-12	9.94e-12	4.06e-12	1.44e-12	7.24e-11
Canes Venatici I	1.96e-13	5.78e-13	9.38e-12	1.03e-11	4.21e-12	1.45e-12	7.47e-11
Canes Venatici II	1.75e-13	5.68e-13	9.05e-12	9.75e-12	3.99e-12	1.41e-12	7.18e-11
Hercules	3.85e-13	1.53e-12	2.83e-11	3.60e-11	1.41e-11	4.08e-12	2.28e-10
Leo IV	2.16e-13	6.72e-13	1.07e-11	1.18e-11	4.83e-12	1.68e-12	8.54e-11
Leo V	1.99e-13	6.47e-13	1.04e-11	1.12e-11	4.60e-12	1.61e-12	8.29e-11
Leo T	2.18e-13	6.66e-13	1.06e-11	1.11e-11	4.56e-12	1.64e-12	8.37e-11
Segue 1	2.40e-13	6.49e-13	1.00e-11	1.06e-11	4.34e-12	1.60e-12	7.91e-11
Segue 2	2.09e-13	6.77e-13	1.12e-11	1.14e-11	4.71e-12	1.66e-12	8.81e-11
Ursa Major I	2.07e-13	6.16e-13	9.49e-12	9.94e-12	4.09e-12	1.52e-12	7.50e-11
Ursa Major II	2.12e-13	7.31e-13	1.12e-11	1.13e-11	4.67e-12	1.80e-12	8.80e-11
Willman 1	2.16e-13	5.45e-13	9.27e-12	9.79e-12	4.03e-12	1.34e-12	7.33e-11
Reticulum II	2.40e-13	6.71e-13	1.15e-11	1.24e-11	5.07e-12	1.67e-12	9.14e-11
Tucana II	2.89e-13	7.55e-13	1.38e-11	1.60e-11	6.47e-12	1.95e-12	1.11e-10
Horologium I	2.34e-13	6.35e-13	1.10e-11	1.19e-11	4.88e-12	1.59e-12	8.77e-11
Hydra II	3.84e-13	1.18e-12	2.06e-11	2.36e-11	9.60e-12	3.05e-12	1.65e-10
Pisces II	2.36e-13	7.70e-13	1.29e-11	1.41e-11	5.76e-12	1.94e-12	1.03e-10
Grus I	3.15e-13	6.95e-13	1.24e-11	1.43e-11	5.77e-12	1.79e-12	9.95e-11
total	6.81e-12	1.97e-11	3.28e-10	3.60e-10	1.47e-10	4.96e-11	2.61e-09

Table 6.1: Diffuse Galactic emission foreground of the MW, calculated with GALPROP (v57) in different energy bands according to Eq. 5.1 in units of erg cm^{-2} s^{-1}. The integration angle corresponds to the respective resolution of the instrument for each band and is indicated next to the instrument in the header.

6.2 Dark Matter Halo of the Milky Way

When pointing in the directions of the selected dwarf galaxies, the observer also always looks through the DM halo of the MW. For a fully self-consistent description, the DM profile of the MW has to be line-of-sight-integrated according to the same scotogenic WIMP model introduced in Ch. 4. The secondary emission of transported DM annihilation products in the MW is not trivial due to the complex conditions. Cirelli et al. (2011) introduced a method to propagate electrons and positrons produced by DM and calculate the resulting IC and synchrotron emission in the Galactic halo. In this work, the distribution of the secondary DM photons of the MW halo itself is omitted because large parts of what could be expected from DM annihilation is already taken into account by the GALPROP simulations which are built in a way to explain the entire *measured* diffuse emission. Therefore, the considerations are limited to the prompt photons from DM annihilation in the MW assuming a standard NFW profile with $\rho_s = 0.41\,\mathrm{GeV\,cm^{-3}}$ at $r_s = 20\,\mathrm{kpc}$ (see Eq. 2.2).

The differential fluxes are evaluated according to Eq. 4.1 where the directional dependence is embedded in the J-factor. If the line-of-sight-integrated squared DM distribution is averaged over the full sky, a J-factor of $1.8 \times 10^{22}\,\mathrm{GeV^2\,cm^{-5}}$ is obtained for the chosen NFW profile, which is about four orders of magnitude larger than the J-factors of the dSphs in Tab. 5.1. The energy dependence of the NFW foreground comes from the annihilation spectrum dN/dE for photons. Thus, the spectral shape of the primary DM emission of the MW is equal to the prompt photon spectrum in Fig. 4.1 peaking around 50 GeV.

The NFW profile is characterized by a cusp towards the center of the Galaxy, so that the line-of-sight-integrated emission is naturally concentrated towards the GC (see Fig. 6.4).

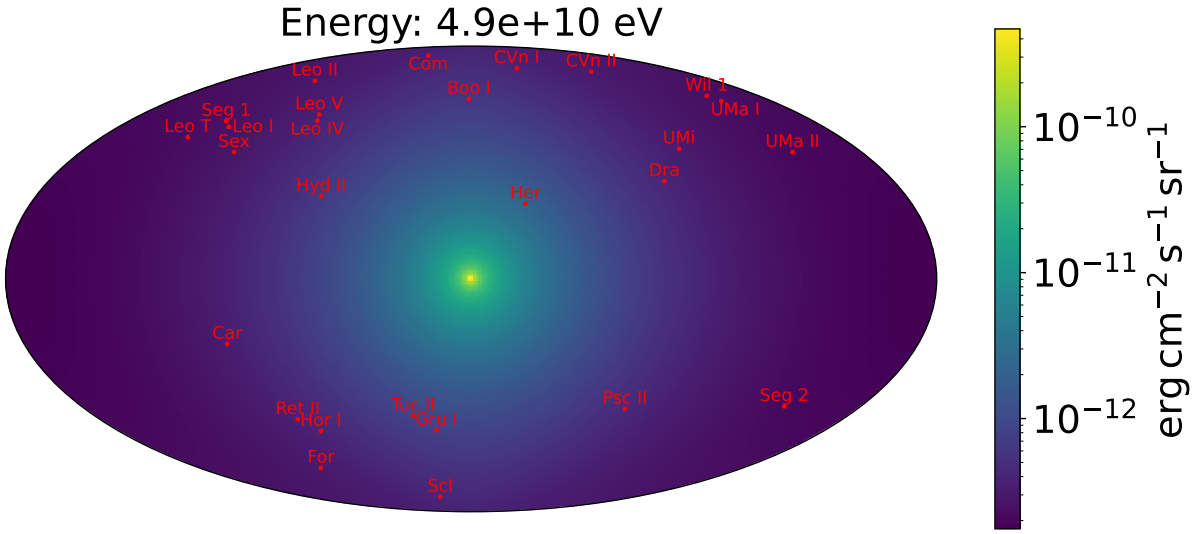

Figure 6.4: Expected sky map of the prompt scotogenic WIMP DM annihilation in the MW assuming an NFW profile. The positions of the dSphs are marked in red.

Galaxy	JEM-X|ISGRI 0.6° 1 keV-30 keV	Swift/BAT 1° 14 keV-195 keV	SPI 4° 100 keV-1 MeV	COMPTEL 3° 1 MeV-30 MeV	Fermi/LAT 3° 30 MeV-100 MeV	Fermi/LAT 1° 100 MeV-100 GeV	Total 100 keV -100 GeV
Carina	-	-	2.95e-22	6.25e-20	5.86e-19	8.92e-16	1.59e-14
Draco	-	-	3.66e-22	8.13e-20	7.63e-19	9.93e-16	1.97e-14
Fornax	-	-	2.87e-22	5.90e-20	5.54e-19	5.56e-16	1.54e-14
Leo I	-	-	2.38e-22	5.02e-20	4.71e-19	4.89e-16	1.28e-14
Leo II	-	-	2.69e-22	5.70e-20	5.35e-19	7.46e-16	1.44e-14
Sculptor	-	-	3.76e-22	7.88e-20	7.39e-19	1.07e-15	2.02e-14
Sextans	-	-	2.59e-22	5.44e-20	5.10e-19	6.11e-16	1.39e-14
Ursa Minor	-	-	2.97e-22	6.56e-20	6.16e-19	6.67e-16	1.59e-14
Boötes I	-	-	5.78e-22	1.23e-19	1.16e-18	1.27e-15	3.11e-14
Coma Berenices	-	-	3.34e-22	6.98e-20	6.55e-19	7.83e-16	1.79e-14
Canes Venatici I	-	-	3.82e-22	8.03e-20	7.53e-19	1.05e-15	2.05e-14
Canes Venatici II	-	-	2.82e-22	5.99e-20	5.62e-19	6.12e-16	1.52e-14
Hercules	-	-	2.05e-21	4.25e-19	3.99e-18	5.67e-15	1.10e-13
Leo IV	-	-	3.33e-22	6.85e-20	6.42e-19	5.97e-16	1.79e-14
Leo V	-	-	3.25e-22	6.66e-20	6.24e-19	6.85e-16	1.75e-14
Leo T	-	-	2.06e-22	4.43e-20	4.16e-19	6.06e-16	1.11e-14
Segue 1	-	-	2.38e-22	4.67e-20	4.38e-19	4.66e-16	1.28e-14
Segue 2	-	-	2.02e-22	4.19e-20	3.93e-19	6.23e-16	1.09e-14
Ursa Major I	-	-	2.10e-22	4.37e-20	4.10e-19	4.06e-16	1.13e-14
Ursa Major II	-	-	1.91e-22	3.70e-20	3.47e-19	4.95e-16	1.03e-14
Willman 1	-	-	2.22e-22	4.75e-20	4.46e-19	5.86e-16	1.19e-14
Reticulum II	-	-	3.36e-22	7.19e-20	6.74e-19	8.74e-16	1.81e-14
Tucana II	-	-	8.00e-22	1.76e-19	1.65e-18	2.35e-15	4.30e-14
Horologium I	-	-	3.65e-22	7.77e-20	7.29e-19	9.95e-16	1.96e-14
Hydra II	-	-	5.81e-22	1.24e-19	1.16e-18	1.65e-15	3.12e-14
Pisces II	-	-	4.28e-22	8.84e-20	8.30e-19	1.13e-15	2.30e-14
Grus I	-	-	7.56e-22	1.62e-19	1.52e-18	2.22e-15	4.06e-14
total	-	-	1.12e-20	2.36e-18	2.22e-17	2.91e-14	6.02e-13

Table 6.2: Contributions of the prompt scotogenic WIMP DM annihilation in the MW assuming a NFW profile as DM halo. The fluxes are given in units of $\mathrm{erg\,cm^{-2}\,s^{-1}}$. The integration angle corresponds to the respective resolution of the instrument for each band and is indicated next to the instrument in the header.

The resulting fluxes for the directions of the 27 selected galaxies are calculated according to Eq. 5.1 and listed in Tab. 6.2. The radius of the integrated circular region corresponds again to the respective resolution of the instrument in each band. Note that the fluxes from the NFW foreground can only be calculated in instrument bands above 100 keV because the prompt annihilation spectrum ranges from 100 keV to 1 TeV. The quoted fluxes directly reflect the locations of the dSphs which show larger foreground fluxes the closer they are to the GC. In general, the background from prompt DM emission is much smaller than from the diffuse GALPROP emission (see Tab. 6.1). At 50 GeV, where the DM fluxes are maximal, they are still four orders of magnitudes below the GALPROP fluxes. Likewise, it can be seen from the sky maps that for the direction of the GC the Galactic foreground is outshining the prompt scotogenic DM annihilation emission by two to three orders of magnitude. This means on the basis of prompt emission alone, there is hardly any reliable technique to detect a DM signal from the MW itself. Dwarf galaxies located at higher latitudes have the advantage of being exposed to lower astrophysical fore- and backgrounds. As a consequence of the expected DM fluxes and the Galactic fore- and backgrounds, individual signal-to-background ratios are estimated to find optimal candidates for a multiwavelength search.

6.3 Combined Multiwavelength SEDs

For visualization, the spectra for the MW foreground in the respective directions of the dwarf galaxies are added to the SEDs expected from the scotogenic DM model (see Sec. 5.2). The combined individual SEDs for all dSphs are displayed in Figs. 6.5-6.8. For each galaxy, the diffuse MW emission is shown as simulated by GALPROP summed over all components (see Sec. 6.1) as well as the prompt DM emission from the MW itself having the same spectral shape for all galaxies (see Sec. 6.2). A quantitative comparison of the signal-to-background ratios of the selected galaxies is provided in Sec. 6.5.

Fig. 6.9 shows the cumulative DM signal and MW foreground of all 27 selected dwarf galaxies in the radio regime and in X- to γ-rays. The "stacked" DM fluxes contain primary and all secondary contributions as shown in Fig. 5.2. It can be seen that the prompt DM emission from all galaxies of the sample together is about as strong as that from the MW summed over the respective directions. The dominant foreground component is the diffuse Galactic emission which cannot be outshined by the faint DM signals.

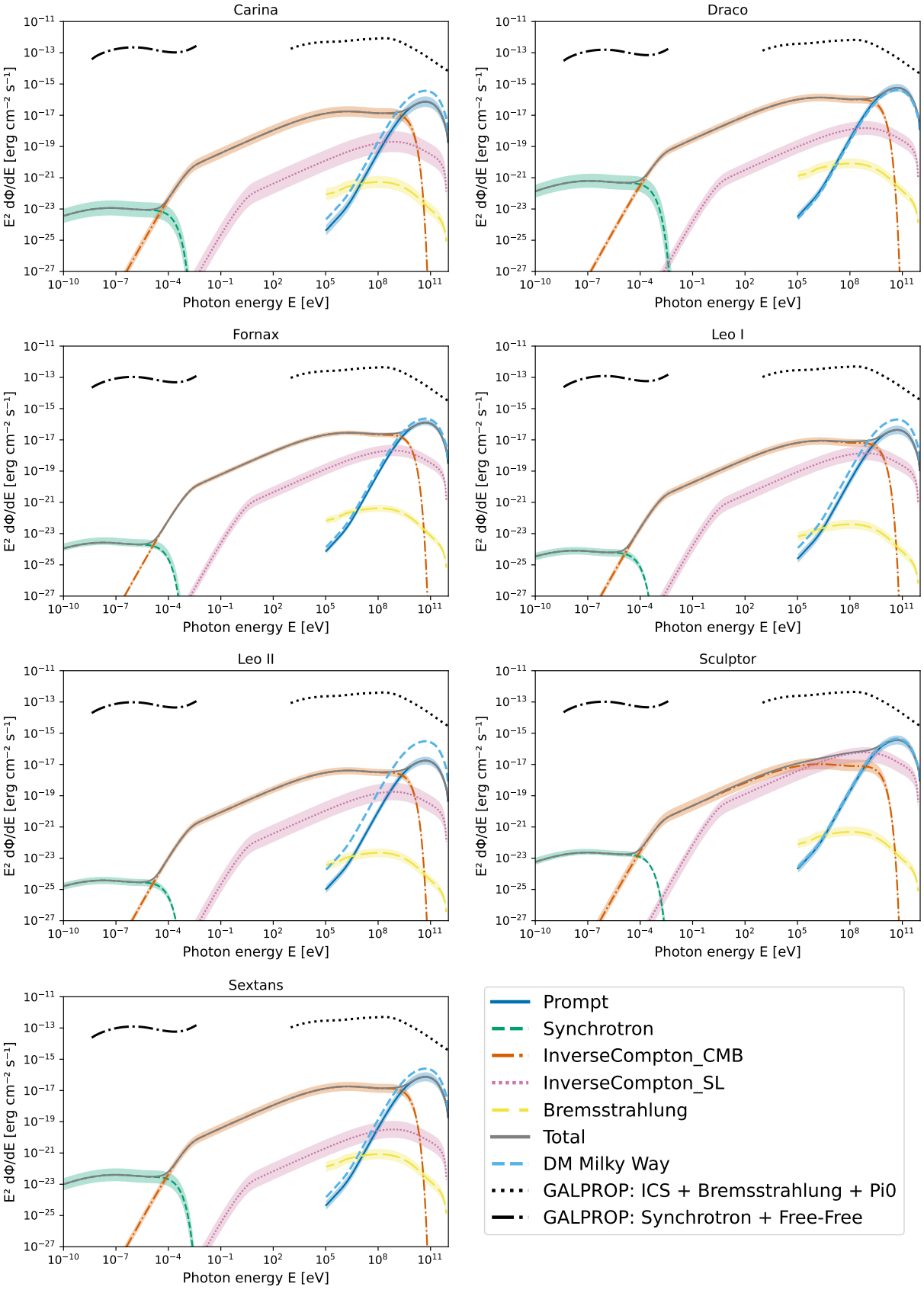

Figure 6.5: DM signal including its uncertainty band of individual dSphs compared to the diffuse emission of the MW and its own prompt DM flux in the direction of the respective galaxy.

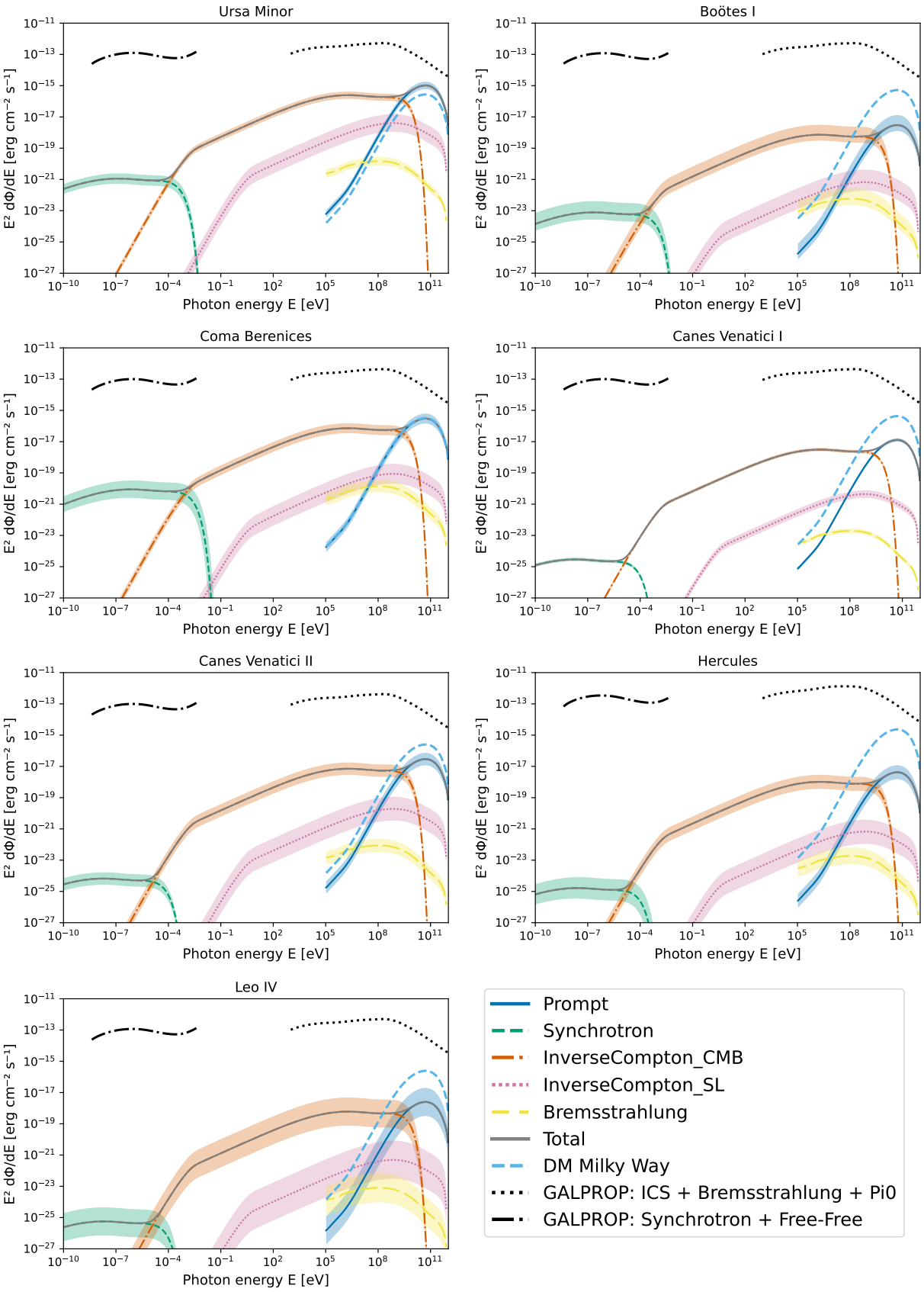

Figure 6.6: Same as Fig. 6.5 for a different set of galaxies.

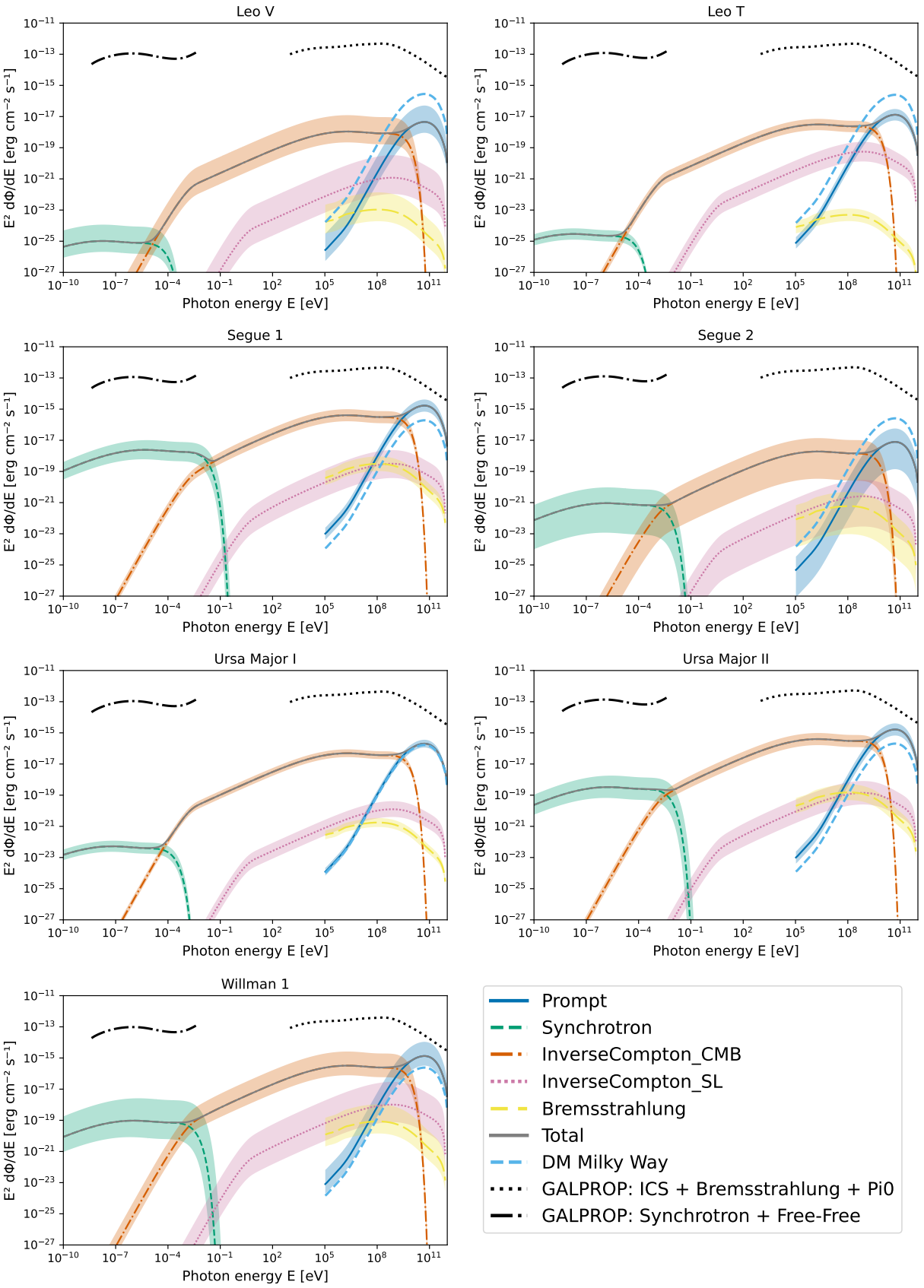

Figure 6.7: Same as Fig. 6.5 for a different set of galaxies.

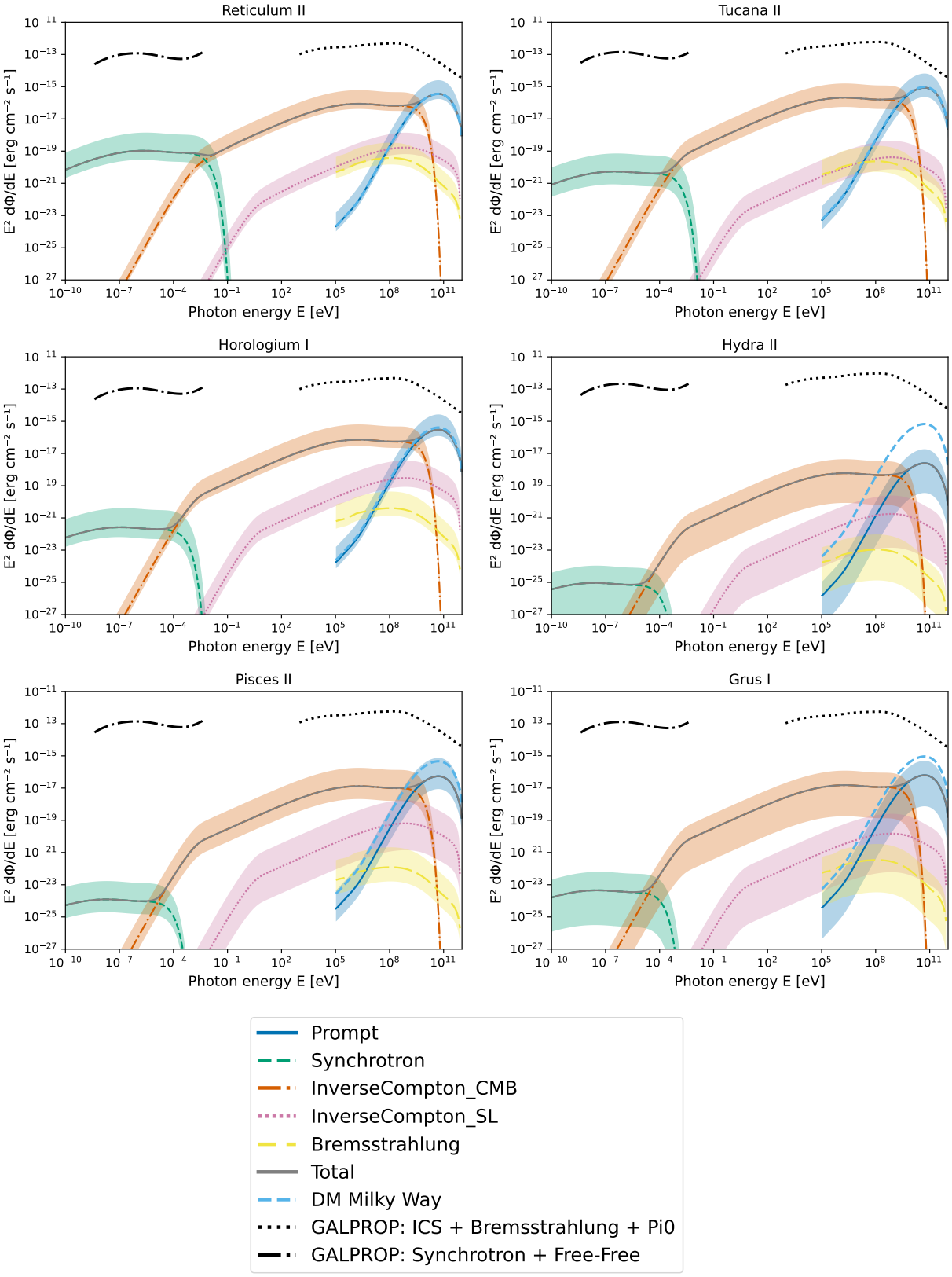

Figure 6.8: Same as Fig. 6.5 for a different set of galaxies.

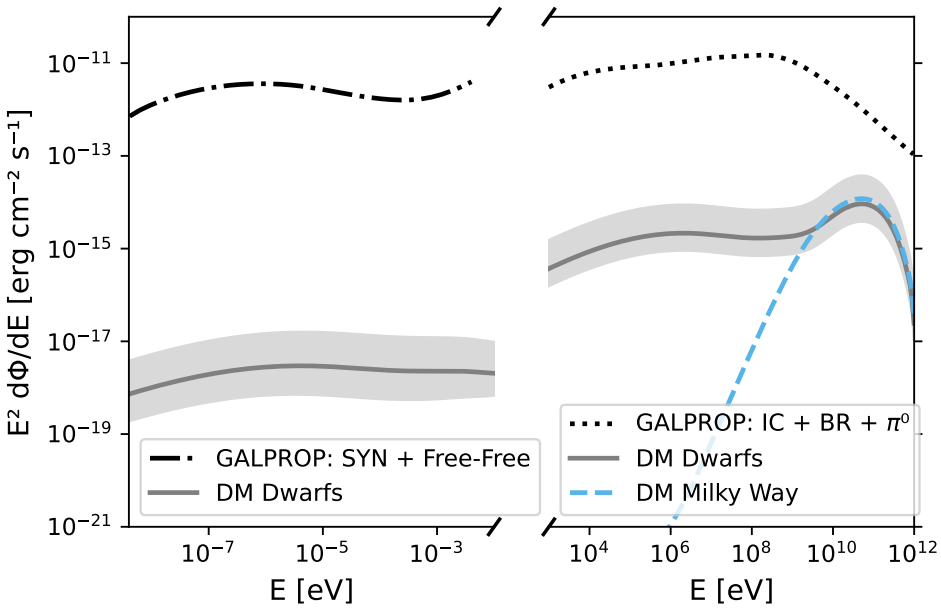

Figure 6.9: Cumulative DM signal of all 27 selected dSphs in the radio regime and in X- to γ-rays compared to the total diffuse emission of the MW and its own prompt DM flux. The shown parts of the DM SED of the dSphs, including its uncertainty band, correspond to the total fluxes in Fig. 5.2. The MW foregrounds are the respective sums of all spectra in the directions of the dSphs.

6.4 Source Confusion

The astrophysical background comes mostly from AGN in the vicinity of the selected galaxies, which may lead to source confusion, i.e. a small angular separation to the respective galaxies. Therefore, source catalogues of the respective high-energy instruments are considered to search for nearby sources whose signal could be confused with the DM signal from the dSphs. In order to identify such sources along the line-of-sight of the respective dwarf galaxies, the following catalogues are used, covering the whole energy spectrum from X-rays to high-energies: The INTEGRAL General Reference Source Catalogue (Bird et al. 2010) with sources detected by INTEGRAL/ISGRI (20–200 keV), the Swift/BAT 105-Month Hard X-ray Catalogue (Oh et al. 2018) covering 14–195 keV, the SPI Catalogue covering 20 keV–2 MeV (Bouchet et al. 2008), the First COMPTEL Source Catalogue (Schönfelder et al. 2000) covering 1–30 MeV, the First Fermi-LAT Low Energy Catalogue (Principe et al. 2018) covering 30–100 MeV, and the Fermi-LAT Fourth Source Catalogue (Abdollahi et al. 2020) covering 0.1–100 GeV. An interfering signal from a background source is assumed if the angular separation between the dwarf galaxy and any catalogue source is less than the angular resolution of the instrument in the respective energy band. Given that the halo sizes of the selected dSphs are mostly less than 1° (Evans et al. 2016), the angular resolutions of 0.6°, 1°, 4°, 3°, and 3°/1° for ISGRI, Swift/BAT, SPI, COMPTEL, and Fermi/LAT can be used as source separations, respectively.

	JEM-X|ISGRI 0.6° 1 keV-30 keV	Swift/BAT 1° 14 keV-195 keV	SPI 4° 100 keV-1 MeV	COMPTEL 3° 1 MeV-30 MeV	Fermi/LAT 3° 30 MeV-100 MeV	Fermi/LAT 1° 100 MeV-100 GeV
Carina	-	SWIFT J0639.9-5124 7.92e-12	-	-	-	-
Fornax	-	-	-	-	-	4FGL J0240.8-3401 1.95e-12
Sextans	-	-	-	-	-	4FGL J1010.8-0158 4.61e-12
Coma Berenices	-	-	-	GRO J1224+2155 2.71e-10	1FLE J1224+2118 5.64e-11	4FGL J1224.4+2436 1.61e-11
Canes Venatici II	-	-	NGC 4138 2.45e-08	-	-	-
Hercules	-	SWIFT J1650.5+0434 2.08e-11	-	-	-	4FGL J1650.9+0429 2.36e-12 4FGL J1649.6+0411 3.37e-12
Willman 1	-	-	-	-	-	4FGL J1049.7+5011 2.11e-12
Tucana II	-	-	-	-	-	4FGL J2247.7-5857 2.08e-12
Horologium I	-	-	-	-	-	4FGL J0253.2-5441 4.23e-12
Pisces II	-	SWIFT J2256.5+0526 9.11e-12	-	-	-	-
Grus I	J225400.0-500000 2.55e-21	-	-	-	-	-

Table 6.3: Background AGN in the vicinity of the selected dwarf galaxies. The fluxes are given in units of erg cm^{-2} s^{-1}. The assumed angular separation between the dwarf galaxies and the sources of the selected catalogues (see Sec. 6.4) is indicated in the header after the instrument in each energy band. In total, 15 AGN coincide with one of the dwarf galaxies in the selected angular ranges.

In total, 15 potential background sources are found for 11 out of the 27 dwarf galaxies in the selected angular ranges. They are displayed together with their fluxes in Tab. 6.3. Compared to the diffuse foreground fluxes in Tab. 6.1, the background fluxes are of the same or higher order of magnitude except for the ISGRI band. The same sources might also contribute to the radio bands which are not considered in this work for the calculation of signal-to-background-ratios. The reason for that is that there are dozens if not hundreds of sources within one square-degree leading to a large background while the DM signal in radio wavelengths is subdominant in dwarf galaxies (see Fig. 5.2). Therefore, focus is put on the X-ray to high-energy bands where the astrophysical background is lower and the expected signal larger.

6.5 Signal-to-Background Ratio

To calculate signal-to-background ratios for each dSph, the fluxes from the MW foreground and the AGN background as calculated in Tabs. 6.1, 6.2 and 6.3, respectively, are combined to a total background emission which is divided by the expected DM signal (see Tab. 5.2) in each instrument band. The results are shown in Tab. 6.4. The ratios range from 10^{-9} to 10^{-3} between 1 keV and 100 GeV. The largest signal-to-background ratios are obtained in the lowest (1–30 keV) and highest (0.1–100 GeV) energy band. However, the diffuse foreground emission below 100 keV is very uncertain and might be enhanced as discussed in Sec. 6.1. The high-energy band from 100 MeV to 100 GeV lies in the prompt emission regime where the DM signal has the highest amplitude resulting in increased signal-to-background ratios.

The largest signal-to-background ratio from an individual galaxy is expected for Segue 1 which is the closest dSph of the selected sample and has the strongest DM emission (see Fig. 5.1). Apart from that, Segue 1 is located far from the GC where the MW foreground is relatively low (see e.g. Fig. 6.2). Conversely, Canes Venatici II exhibits the smallest total signal-to-background ratio because of the nearby source NGC 4138 creating a large background flux of $2 \times 10^{-8}\,\mathrm{erg\,cm^{-2}\,s^{-1}}$ in the SPI band. The smallest ratios over all energy bands are attributed to Hydra II and Hercules which are the galaxies closest to the GC and consequently exposed to a high foreground. Hydra II is also the galaxy with the lowest total DM flux due to its relatively large distance and small size (see Fig. 5.1). It is evident that no galaxy would outshine the MW as the expected primary and secondary emission from scotogenic WIMP DM is at least three orders of magnitude below the fore- and background contributions. Trying to observe only the prompt emission of an individual galaxy would take several thousands of years to obtain a reasonable signal-to-noise ratio (see Fig. 6.10). However, the characteristic double- (X-rays to very-high-energy gamma-rays) or triple-hump (including radio) structure of the DM SEDs allows for a correlated multiwavelength analysis including as many instruments as possible. In

addition to long exposures, the cumulative effect of sources will increase the chances of detecting the faint DM signals.

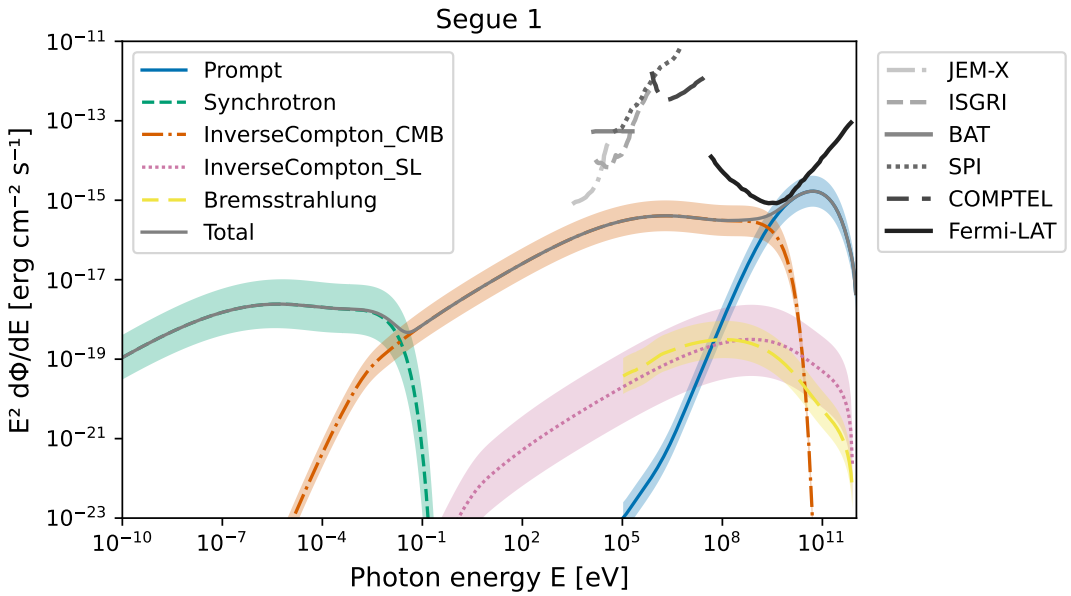

Figure 6.10: Same as upper left plot in Fig. 5.1 (dSph with the largest total flux) but in comparison to the sensitivities curves of the instruments considered in this work. The sensitivities are scaled to an observation time of about 8000 years, which would be needed to observe the prompt emission with Fermi-LAT.

Galaxy	JEM-X|ISGRI 1 keV-30 keV	Swift-BAT 14 keV-195 keV	SPI 100 keV-1 MeV	COMPTEL 1 MeV-30 MeV	Fermi 30 MeV-100 MeV	Fermi 100 MeV-100 GeV	Total 1 keV-100 GeV
Carina	4.10e-05	3.14e-06	1.76e-06	2.84e-06	1.86e-06	7.68e-05	2.39e-06
Draco	4.53e-04	2.49e-04	1.69e-05	2.58e-05	1.71e-05	7.83e-04	2.41e-05
Fornax	1.84e-04	7.66e-05	5.79e-06	9.11e-06	6.21e-06	1.14e-04	8.46e-06
Leo I	5.33e-05	2.06e-05	1.63e-06	2.64e-06	1.87e-06	7.94e-05	2.62e-06
Leo II	2.41e-05	1.20e-05	8.59e-07	1.36e-06	9.11e-07	3.98e-05	1.26e-06
Sculptor	8.38e-05	4.17e-05	3.65e-06	1.03e-05	1.30e-05	8.26e-04	1.94e-05
Sextans	6.52e-05	4.21e-05	2.97e-06	4.71e-06	3.09e-06	3.63e-05	4.00e-06
Ursa Minor	9.20e-04	5.60e-04	3.99e-05	6.34e-05	4.19e-05	1.79e-03	5.72e-05
Boötes I	3.89e-06	1.74e-06	1.27e-07	1.87e-07	1.24e-07	5.32e-06	1.78e-07
Coma Berenices	4.76e-04	2.04e-04	1.52e-05	8.21e-07	1.03e-06	5.24e-05	3.73e-06
Canes Venatici I	1.84e-05	8.69e-06	6.28e-07	9.52e-07	6.29e-07	2.69e-05	8.85e-07
Canes Venatici II	4.70e-05	2.02e-05	5.49e-10	2.31e-06	1.52e-06	6.36e-05	6.15e-09
Hercules	3.10e-06	7.44e-08	6.90e-08	9.05e-08	6.20e-08	1.32e-06	8.58e-08
Leo IV	3.26e-06	1.46e-06	1.07e-07	1.62e-07	1.07e-07	4.54e-06	1.51e-07
Leo V	6.43e-06	2.76e-06	2.01e-07	3.10e-07	2.04e-07	8.61e-06	2.83e-07
Leo T	1.66e-05	7.55e-06	5.58e-07	8.94e-07	5.89e-07	2.45e-05	8.03e-07
Segue 1	1.97e-03	1.01e-03	7.73e-05	1.22e-04	8.00e-05	3.22e-03	1.10e-04
Segue 2	1.06e-05	4.57e-06	3.25e-07	5.32e-07	3.47e-07	1.45e-05	4.63e-07
Ursa Major I	2.76e-04	1.29e-04	9.86e-06	1.57e-05	1.03e-05	4.08e-04	1.40e-05
Ursa Major II	2.20e-03	8.85e-04	6.80e-05	1.12e-04	7.29e-05	2.81e-03	9.68e-05
Willman 1	1.74e-03	9.62e-04	6.65e-05	1.05e-04	6.88e-05	1.19e-03	9.18e-05
Reticulum II	4.22e-04	2.11e-04	1.44e-05	2.23e-05	1.47e-05	6.58e-04	2.04e-05
Tucana II	8.45e-04	4.50e-04	2.90e-05	4.15e-05	2.77e-05	6.55e-04	3.97e-05
Horologium I	3.60e-04	1.85e-04	1.25e-05	1.93e-05	1.27e-05	1.58e-04	1.68e-05
Hydra II	1.83e-06	8.28e-07	5.56e-08	8.10e-08	5.37e-08	2.50e-06	7.79e-08
Pisces II	6.48e-05	2.16e-06	1.94e-06	2.96e-06	1.96e-06	8.58e-05	2.52e-06
Grus I	5.60e-05	3.54e-05	2.33e-06	3.37e-06	2.25e-06	1.07e-04	3.25e-06
total	4.19e-03	6.91e-04	1.88e-06	1.26e-04	1.09e-04	3.89e-03	2.01e-05

Table 6.4: Signal-to-background ratios as calculated by dividing Tab. 5.2 by the total fore- and background from diffuse emission (Tabs. 6.1 and 6.2) and nearby point sources (Tab. 6.3).

7 Conclusion and Outlook

In this work, a parametrized model for dwarf galaxies, which predicts the expected photon spectrum from DM annihilation within the galaxy's halo as observed from the Earth, is introduced. What is special about the approach used in this analysis is that the whole multiwavelength SED is considered including both the prompt photon signature and secondary emission from charged annihilation products, such as IC scattering of CMB and SL photons, bremsstrahlung and synchrotron radiation. The model is valid for a specific scotogenic WIMP with a mass of about 1 TeV and a cross section of $\langle \sigma v \rangle \approx 10^{-26}\,\mathrm{cm}^3\,\mathrm{s}^{-1}$ which mainly annihilates into W^+W^- and ZZ. From the J-factor, distance, visual magnitude and half-light radius characteristic for each galaxy, the DM photon spectrum was calculated in 27 dSphs of the MW reaching from synchrotron emission in the MHz range to the IC peak at MeV energies and to the prompt signature in the GeV up to TeV regime. This unique "triple hump" structure will be easily distinguishable from any other source if it can be disentangled from the large astrophysical fore-and backgrounds. In order to determine signal-to-background ratios in different energy bands for each galaxy, the diffuse MW foreground is estimated via GALPROP simulations and the prompt DM emission is calculated within the halo of the MW from the same scotogenic model. It is searched for possible background emission from AGN along the line-of-sight and 15 potential source confusions are found, which are considered as additional background flux. Signal-to-background ratios up to the order of 10^{-3} are obtained for individual galaxies with the largest being the values for Segue 1.

It is evident that DM signals restricted to a certain energy band and galaxy, usually the prompt emission peaking in the high-energy regime, are too faint to be detectable against the large MW foreground. However, DM annihilation leads to a very characteristic signature if viewed over a wide range of energies unveiling the spectrum of secondary emissions. The amplitudes of the emission components scale with astrophysical parameters characteristic for each galaxy. The underlying DM model which determines the shape of the unique DM spectrum is shared by all galaxies allowing for a coherent analysis. This means that the predictions of this work could be probed if multiple sources are observed with long exposure times by many instruments covering the X- to very-high-energy gamma-rays as gapless as possible. The more galaxies are taken into account, the more rigid becomes the DM annihilation model. For this reason, the parametrized model should be extended for more (nearby) galaxies beyond dSphs, which would lead to an unambiguous signal across

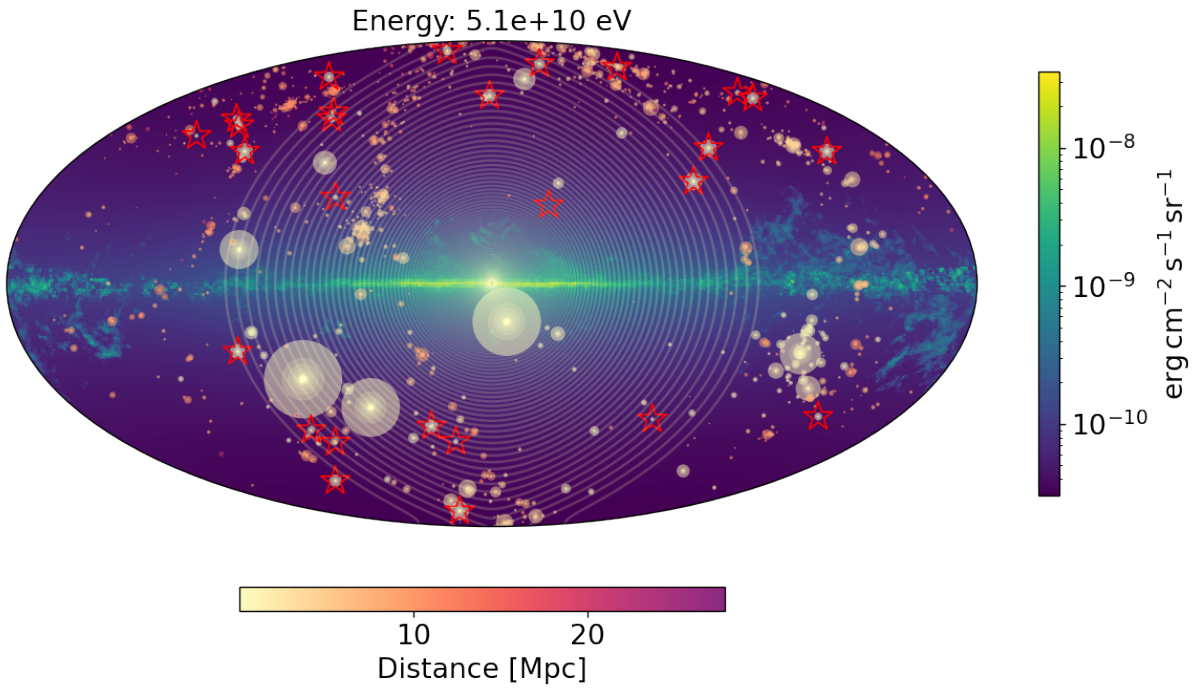

Figure 7.1: GALPROP (v57) simulations at around 50 GeV including bremsstrahlung, IC scattering and pion decay. All 1440 Local Volume galaxies (Karachentsev & Kashibadze 2006) are displayed with their distances colorcoded. The circle size scales with the angular diameter of the respective galaxy. The positions of the 27 dSphs are marked as red stars. Part of the MW halo is illustrated in the form of contours. The supergalactic plane is visible and would show a distinct feature compared to the diffuse MW emission.

the supergalactic plane. Fig. 7.1 shows all 1440 Local Volume galaxies (Karachentsev & Kashibadze 2006) including the Galactic halo according to their size and distance in front of the diffuse MW foreground at 50 GeV where the DM spectrum is peaking. Assuming that, on average, all galaxies exhibit a DM flux about 10^{-15} erg cm^{-2} s^{-1} at 50 GeV, which corresponds to the peak emission of the brightest dwarf, Segue 1, scaled to distance with a factor 23 kpc/d, the total signal from all Local Volume galaxies would be of the order of 10^{-14} erg cm^{-2} s^{-1}. This value should be seen as a lower limit since most galaxies are much bigger and brighter than dSphs, which means that they contain more DM and more SL photons to be upscattered. This would enhance the IC component in the high-energy regime. In addition, there would be a third IC component for galaxies containing a significant amount of dust and therefore an IR photon field. At the same time, bigger galaxies also contain more gas which increases their own intrinsic background.

The expected DM signals may be further enhanced by subhalo clumping within the halo of a galaxy increasing the DM density along the line-of-sight. The subhalo boost factor cannot be determined with high accuracy but is estimated to be of the order of 1 to 100 for galaxies of the size of the MW and potentially below 10 for the case of dSphs (Ando et al. 2019).

Another improvement of the parametrized DM model will be to implement also the tertiary emission which refers to the annihilation of propagated and cooled positrons. This would lead to a distinct feature in the spectrum consisting of a line emission at 511 keV and a continuum stemming from Positronium formation (Siegert et al. 2022b, 2016). However, the propagation of charged particles is hardly understood in diverse interstellar environments and conditions (Siegert 2023). In fact, the positrons could also escape from the galaxy into the intergalactic medium before annihilating.

A promising strategy for disentangling DM signatures from foreground emission are studies of the Cosmic Gamma-ray Background (CGB) which would show distinct redshift dependent features of primary, secondary and tertiary DM annihilation components.

Considering future measurements, larger accuracy in the GeV to TeV range will be reached by the Cerenkov Telescope Array (CTA) (Maier 2019) in combination with ongoing wide field-of-view surveys with Fermi/LAT. In the MeV range, the Compton Spectrometer and Imager (COSI) will launch in 2027 and enhance the sensitivity from 0.2 to 5 MeV immensely compared to previous instruments while providing deep exposures of the full sky (Tomsick et al. 2019, 2023). In the light of upcoming observatories like COSI-SMEX and CTA, the detection of faint DM signals is within reach if a coherent analysis across the MeV to GeV range is applied on all nearby galaxies in addition to an improved measurement and theoretical description of the CGB.

Bibliography

Abazajian, K., Fuller, G. M., & Patel, M. 2001, Physical Review D, 64

Abdalla, H., Aharonian, F., Benkhali, F. A., et al. 2022, Phys. Rev. Lett., 129, 111101

Abdallah, H., Abramowski, A., Aharonian, F., et al. 2016, Phys. Rev. Lett., 117, 111301

Abdollahi, S., Acero, F., Ackermann, M., et al. 2020, The Astrophysical Journal Supplement Series, 247, 33

Abi, B., Albahri, T., Al-Kilani, S., et al. 2021, Phys. Rev. Lett., 126, 141801

Acciari, V., Ansoldi, S., Antonelli, L., et al. 2022, Physics of the Dark Universe, 35, 100912

Ackermann, M., Ajello, M., Albert, A., et al. 2015a, Phys. Rev. D, 91, 122002

Ackermann, M., Ajello, M., Albert, A., et al. 2017, The Astrophysical Journal, 840, 43

Ackermann, M., Ajello, M., Atwood, W. B., et al. 2012, The Astrophysical Journal, 750, 3

Ackermann, M., Albert, A., Anderson, B., et al. 2015b, Phys. Rev. Lett., 115, 231301

Ackermann, M., Albert, A., Anderson, B., et al. 2014, Phys. Rev. D, 89, 042001

Ade, P. A. R., Aghanim, N., Arnaud, M., et al. 2016, A&A, 594, A14

Adriani, O., Barbarino, G. C., Bazilevskaya, G. A., et al. 2009, Nature, 458, 607

Aghanim, N., Akrami, Y., Ashdown, M., et al. 2020, A&A, 641, A6

Aghanim, N., Akrami, Y., Arroja, F., et al. 2020, A&A, 641, A1

Agnese, R., Anderson, A. J., Aralis, T., et al. 2018, Phys. Rev. D, 97, 022002

Aharonian, F. A., Kelner, S. R., & Prosekin, A. Y. 2010, Phys. Rev. D, 82, 043002

Ajello, M., Gasparrini, D., Sánchez-Conde, M., et al. 2015, The Astrophysical Journal Letters, 800, L27

Albert, A., André, M., Anghinolfi, M., et al. 2020, Phys. Rev. D, 102, 082002

Alcock, C., Allsman, R. A., Alves, D. R., et al. 2000, The Astrophysical Journal, 542, 281

Alp, D. & Modée, S. 2014

Alvarez, A., Banik, A., Cepedello, R., et al. 2023, Journal of High Energy Physics, 2023

Amole, C., Ardid, M., Arnquist, I., et al. 2019, Physical Review D, 100

Ando, S., Ishiyama, T., & Hiroshima, N. 2019, Galaxies, 7, 68

Aprile, E., Aalbers, J., Agostini, F., et al. 2018, Physical Review Letters, 121

Aprile, E., Aalbers, J., Agostini, F., et al. 2017, The European Physical Journal C, 77

Ardu, M. & Pezzullo, G. 2022, Universe, 8, 299

Arnaud, Q., Armengaud, E., Augier, C., et al. 2020, Physical Review Letters, 125

Atwood, W. B., Abdo, A. A., Ackermann, M., et al. 2009, The Astrophysical Journal, 697, 1071

Ávila, I. M., Romeri, V. D., Duarte, L., & Valle, J. W. F. 2020, The European Physical Journal C, 80

Baldini, A. M. et al. 2016, Eur. Phys. J. C, 76, 434

Baratella, P., Cirelli, M., Hektor, A., et al. 2014, Journal of Cosmology and Astroparticle Physics, 2014, 053

Baring, M. G., Ellison, D. C., Reynolds, S. P., Grenier, I. A., & Goret, P. 1999, The Astrophysical Journal, 513, 311

Bartels, R. & Ando, S. 2015, Physical Review D, 92

Barthelmy, S. D., Barbier, L. M., Cummings, J. R., et al. 2005, Space Science Reviews, 120, 143

Bauer, M. & Plehn, T. 2018, Yet Another Introduction to Dark Matter

Beck, R. 2011, in Space Sciences Series of ISSI (Springer New York), 215–230

Begeman, K. G., Broeils, A. H., & Sanders, R. H. 1991, Monthly Notices of the Royal Astronomical Society, 249, 523

Begeman, K. G., Broeils, A. H., & Sanders, R. H. 1991, Monthly Notices of the Royal Astronomical Society, 249, 523

Belanger, G., Boudjema, F., & Pukhov, A. 2014, micrOMEGAs : a code for the calculation of Dark Matter properties in generic models of particle interaction

Bell, N. F., Cai, Y., Dent, J. B., Leane, R. K., & Weiler, T. J. 2015, Phys. Rev. D, 92, 053008

Bernabei, R., Belli, P., Caracciolo, V., et al. 2021, The dark matter: DAMA/LIBRA and its perspectives

Berteaud, J., Calore, F., Iguaz, J., Serpico, P. D., & Siegert, T. 2022, Phys. Rev. D, 106, 023030

Bertone, G. & Tait, T. M. P. 2018, Nature, 562, 51

Binney, J., Gerhard, O., & Silk, J. 2001, Monthly Notices of the Royal Astronomical Society, 321, 471–474

Binney, J. J. & Evans, N. W. 2001, Monthly Notices of the Royal Astronomical Society, 327, L27–L31

Bird, A. J., Bazzano, A., Bassani, L., et al. 2010, arXiv.org, 186, 1

Bisschoff, D., Potgieter, M. S., & Aslam, O. P. M. 2019, The Astrophysical Journal, 878, 59

Blumenthal, G. R. & Gould, R. J. 1970, Rev. Mod. Phys., 42, 237

Bond, J. R., Cole, S., Efstathiou, G., & Kaiser, N. 1991, The Astrophysical Journal, 379, 440

Borsanyi, S., Fodor, Z., Guenther, J. N., et al. 2021, Nature, 593, 51

Bouchet, L., Jourdain, E., Roques, J. P., et al. 2008, The Astrophysical Journal, 679, 1315

Boudaud, M., Lacroix, T., Stref, M., & Lavalle, J. 2019, Phys. Rev. D, 99, 061302

Bovy, J. & Tremaine, S. 2012, The Astrophysical Journal, 756, 89

Burkert, A. 1995, The Astrophysical Journal, 447, L25

Bélanger, G., Boudjema, F., Kraml, S., Pukhov, A., & Semenov, A. 2006, Physical Review D, 73

Calore, F., Dekker, A., Serpico, P. D., & Siegert, T. 2023, Monthly Notices of the Royal Astronomical Society, 520, 4167

Carr, B. & Kühnel, F. 2022, SciPost Physics Lecture Notes

Cebrián, S. 2023, Journal of Physics: Conference Series, 2502, 012004

Cen, R. & Ostriker, J. P. 1999, The Astrophysical Journal, 514, 1

Chan, M. H., Cui, L., Liu, J., & Leung, C. S. 2019, The Astrophysical Journal, 872, 177

Chang, L. J., Lisanti, M., & Mishra-Sharma, S. 2018, Phys. Rev. D, 98, 123004

Cirelli, M., Corcella, G., Hektor, A., et al. 2011, Journal of Cosmology and Astroparticle Physics, 2011, 051

Cirelli, M., Fornengo, N., Kavanagh, B. J., & Pinetti, E. 2021, Phys. Rev. D, 103, 063022

Cirelli, M., Fornengo, N., Koechler, J., Pinetti, E., & Roach, B. M. 2023, Journal of Cosmology and Astroparticle Physics, 2023, 026

Cirelli, M. & Panci, P. 2009, Nuclear Physics B, 821, 399

Clowe, D., Bradač, M., Gonzalez, A. H., et al. 2006, The Astrophysical Journal, 648, L109

Csáki, C. 1996, Modern Physics Letters A, 11, 599–613

Cui, M.-Y., Yuan, Q., Tsai, Y.-L. S., & Fan, Y.-Z. 2017, Phys. Rev. Lett., 118, 191101

Debattista, V. P. & Sellwood, J. A. 1998, The Astrophysical Journal, 493, L5–L8

Djuvsland, J. I., Hinton, J., & Reville, B. 2023, Physics of the Dark Universe, 39, 101157

Dobrynina, A., Kartavtsev, A., & Raffelt, G. 2015, Phys. Rev. D, 91, 083003

Dolag, K., Bartelmann, M., & Lesch, H. 1999, A&A, 348, 351

Eisenberger, L., Siegert, T., Mannheim, K., & Porod, W. 2024, Monthly Notices of the Royal Astronomical Society, stae214

Evans, N., Sanders, J., & Geringer-Sameth, A. 2016, Physical Review D, 93

Evans, N. W., Ferrer, F., & Sarkar, S. 2004, Phys. Rev. D, 69, 123501

Ferreira, E. 2021, The Astronomy and Astrophysics Review, 29

Ferreras, I. 2019, Fundamentals of Galaxy Dynamics, Formation and Evolution (UCL Press)

Foster, J. W., Park, Y., Safdi, B. R., Soreq, Y., & Xu, W. L. 2023, Phys. Rev. D, 107, 103047

Franarin, T. H., Vasconcellos, C. A. Z., & Hadjimichef, D. 2014, Astronomische Nachrichten, 335, 647

Friedmann, A. 1922, Zeitschrift fur Physik, 10, 377

Fukuda, Y., Hayakawa, T., Ichihara, E., et al. 1998, Phys. Rev. Lett., 81, 1562

Gaskins, J. M. 2016, Contemporary Physics, 57, 496–525

Geringer-Sameth, A. & Koushiappas, S. M. 2011, Physical Review Letters, 107

Giagu, S. 2019, Frontiers in Physics, 7, 75

Goldwurm, A. 2011, in Astronomical Society of the Pacific Conference Series, Vol. 439, The Galactic Center: a Window to the Nuclear Environment of Disk Galaxies, ed. M. R. Morris, Q. D. Wang, & F. Yuan, 391

Henry, J. & Briel, U. 1993, Advances in Space Research, 13, 191

Hiroshima, N., Ando, S., & Ishiyama, T. 2018, Physical Review D, 97

Hisano, J., Matsumoto, S., Nojiri, M. M., & Saito, O. 2005, Phys. Rev. D, 71, 063528

Hu, W. 2001, Intermediate Guide to the Acoustic Peaks and Polarization

Iguaz, J., Serpico, P. D., & Siegert, T. 2021, Phys. Rev. D, 103, 103025

Jean, P., Gillard, W., Marcowith, A., & Ferrière, K. 2009, A&A, 508, 1099

Jee, M. J., Ford, H. C., Illingworth, G. D., et al. 2007, The Astrophysical Journal, 661, 728

Johnson, H. L. & Morgan, W. W. 1953, The Astrophysical Journal, 117, 313

Jungman, G., Kamionkowski, M., & Griest, K. 1996, Physics Reports, 267, 195

Kapteyn, J. C. 1922, The Astrophysical Journal, 55, 302

Karachentsev, I. D. & Kashibadze, O. G. 2006, Astrophysics, 49, 3

Khangulyan, D., Aharonian, F. A., & Kelner, S. R. 2014, The Astrophysical Journal, 783, 100

Koposov, S. E., Belokurov, V., Torrealba, G., & Evans, N. W. 2015, The Astrophysical Journal, 805, 130

Kraljic, D. & Sarkar, S. 2015, Journal of Cosmology and Astroparticle Physics, 2015, 050–050

Krivonos, R., Revnivtsev, M., Churazov, E., et al. 2007, A&A, 463, 957

Lai, M. 2023, Journal of Instrumentation, 18, C02046

Leane, R. K. & Linden, T. 2023, Phys. Rev. Lett., 131, 071001

Lisanti, M., Mishra-Sharma, S., Rodd, N. L., & Safdi, B. R. 2018, Phys. Rev. Lett., 120, 101101

Ma, E. 2006, Phys. Rev. D, 73, 077301

MAGIC_Collaboration. 2016, Journal of Cosmology and Astroparticle Physics, 2016, 039

Maier, G. 2019, in International Cosmic Ray Conference, Vol. 36, 36th International Cosmic Ray Conference (ICRC2019), 733

Martin, N. F., Nidever, D. L., Besla, G., et al. 2015, The Astrophysical Journal, 804, L5

Mauro, M. D., Donato, F., Fornengo, N., Lineros, R., & Vittino, A. 2014, Journal of Cosmology and Astroparticle Physics, 2014, 006

McConnachie, A. W. 2012, The Astronomical Journal, 144, 4

Milgrom, M. 1994, Annals of Physics, 229, 384

Miller, M. J. & Bregman, J. N. 2013, The Astrophysical Journal, 770, 118

Mohapatra, R. N., Nasri, S., & Yu, H.-B. 2005, Phys. Rev. D, 72, 033007

Moore, B., Governato, F., Quinn, T., Stadel, J., & Lake, G. 1998, The Astrophysical Journal, 499, L5–L8

Navarro, J. F., Frenk, C. S., & White, S. D. M. 1997, The Astrophysical Journal, 490, 493–508

Norberg, P., Baugh, C. M., Hawkins, E., et al. 2001, Monthly Notices of the Royal Astronomical Society, 328, 64

Oh, K., Koss, M., Markwardt, C. B., et al. 2018, Astrophysical Journal, Supplement, 235, 4

O'Hare, C. A. J. 2021, Phys. Rev. Lett., 127, 251802

Oort, J. H. 1932, Bulletin of the Astronomical Institutes of the Netherlands, 6, 249

Porter, T. A., Jóhannesson, G., & Moskalenko, I. V. 2022, The Astrophysical Journal Supplement Series, 262, 30

Posti, Lorenzo & Helmi, Amina. 2019, A&A, 621, A56

Press, W. H. & Schechter, P. 1974, The Astrophysical Journal, 187, 425

Principe, G., Malyshev, D., Ballet, J., & Funk, S. 2018, A&A, 618, A22

Pérez de los Heros, C. 2020, Symmetry, 12

Regis, M., Reynoso-Cordova, J., Filipović, M. D., et al. 2021, Journal of Cosmology and Astroparticle Physics, 2021, 046

Restrepo, D., Zapata, O., & Yaguna, C. E. 2013, Journal of High Energy Physics, 2013

Riess, A. G., Casertano, S., Yuan, W., Macri, L. M., & Scolnic, D. 2019, The Astrophysical Journal, 876, 85

Rubin, V. C., Thonnard, N., & Ford, JR., W. K. 1978, The Astrophysical Journal, 225, L107

Saxena, S., Summa, A., Elsässer, D., Rüger, M., & Mannheim, K. 2011, The European Physical Journal C, 71

Schneider, M. D., Frenk, C. S., & Cole, S. 2012, Journal of Cosmology and Astroparticle Physics, 2012, 030–030

Schönfelder, V., Bennett, K., Collmar, W., et al. 1992, in Data Analysis in Astronomy, 185–200

Schönfelder, V., Bennett, K., Blom, J. J., et al. 2000, Astronomy and Astrophysics Supplement Series, 143, 145

Siegert, T. 2023, Astrophysics and Space Science, 368

Siegert, T., Berteaud, J., Calore, F., Serpico, P. D., & Weinberger, C. 2022a, A&A, 660, A130

Siegert, T., Boehm, C., Calore, F., et al. 2022b, Monthly Notices of the Royal Astronomical Society, 511, 914

Siegert, T., Calore, F., & Serpico, P. D. 2024, arXiv e-prints, arXiv:2401.03795

Siegert, T., Diehl, R., Khachatryan, G., et al. 2016, Astronomy & Astrophysics, 586, A84

Siegert, T., Horan, D., & Kanbach, G. 2022, in Handbook of X-ray and Gamma-ray Astrophysics, 80

Sjöstrand, T., Ask, S., Christiansen, J. R., et al. 2015, Computer Physics Communications, 191, 159

Slatyer, T. 2022, SciPost Physics Lecture Notes

Smith, M. S., Kawano, L. H., & Malaney, R. A. 1993, Astrophysical Journal, Supplement, 85, 219

Springel, V. 2006, Sterne und Weltraum, 45, 30

Springel, V., White, S. D. M., Jenkins, A., et al. 2005, Nature, 435, 629

Steigman, G., Dasgupta, B., & Beacom, J. F. 2012, Phys. Rev. D, 86, 023506

Strigari, L., Koushiappas, S., Bullock, J., et al. 2008, The Astrophysical Journal, 678, 614–620

Strong, A. W., Moskalenko, I. V., & Ptuskin, V. S. 2007, Annual Review of Nuclear and Particle Science, 57, 285

Tomsick, J., Zoglauer, A., Sleator, C., et al. 2019, in Bulletin of the American Astronomical Society, Vol. 51, 98

Tomsick, J. A., Boggs, S. E., Zoglauer, A., et al. 2023, arXiv e-prints, arXiv:2308.12362

Tremaine, S. & Gunn, J. E. 1979, Phys. Rev. Lett., 42, 407

Turner, M. S. 1990, Physics Reports, 197, 67

Vedrenne, G., Roques, J. P., Schönfelder, V., et al. 2003, A&A, 411, L63

Villanueva-Domingo, P., Mena, O., & Palomares-Ruiz, S. 2021, Frontiers in Astronomy and Space Sciences, 8

Vitagliano, E., Tamborra, I., & Raffelt, G. 2020, Rev. Mod. Phys., 92, 045006

Walker, T. P., Steigman, G., Schramm, D. N., Olive, K. A., & Kang, H.-S. 1991, The Astrophysical Journal, 376, 51

Wechsler, R. H. & Tinker, J. L. 2018, Annual Review of Astronomy and Astrophysics, 56, 435

White, S. D. M., Frenk, C. S., & Davis, M. 1983, Astrophysical Journal, Letters, 274, L1

Winkler, C., Courvoisier, T. J. L., Di Cocco, G., et al. 2003, A&A, 411, L1

Workman, R. L., Burkert, V. D., Crede, V., et al. 2022, Progress of Theoretical and Experimental Physics, 2022, 083C01

Xiao, M., Perez, K. M., Giannotti, M., et al. 2021, Phys. Rev. Lett., 126, 031101

York, D. G., Adelman, J., Anderson, John E., J., et al. 2000, Astronomical Journal, 120, 1579

Zabalza, V. 2015, in International Cosmic Ray Conference, Vol. 34, 34th International Cosmic Ray Conference (ICRC2015), 922

Zwicky, F. 1933, Helvetica Physica Acta, 6, 110

Acknowledgements

I would like to thank Thomas whose ideas and expertise have made this thesis possible. Through his supervision, I have learnt a lot of new things in the process of this work.

I am very grateful for the insightful discussions with Profs. Karl Mannheim and Werner Porod covering both the field of astrophysics and particle physics.

I also thank Thomas and Karl for their support beyond this thesis concerning travels, conferences and my future career.

I am thankful for being part of AG Siegert where we exchange ideas and motivate each other. I hope that I will get the opportunity to keep on working at the Astro department in Würzburg whose members have become close friends over the past year.

Especially, I am lucky to have Sarah and Patrick as my office mates who can not only give me instant programming advice but also inspire me in many ways.

Finally, I want to thank my family and friends for all kinds of support. Special thanks go to Nicki, Nora and Carsten who are always taking care of me.

Declaration

Erklärung

Hiermit erkläre ich, dass ich die vorliegende Arbeit selbständig verfasst und keine anderen als die angegebenen Quellen und Hilfsmittel verwendet habe. Die Arbeit wurde keiner anderen Prüfungsbehörde unter Erlangung eines akademischen Grades vorgelegt.

Würzburg, den 26.01.2024 ..... (Unterschrift)

Laura Eisenberger